UNIVERSITÀ DEGLI STUDI DI PADOVA

Head Office: Università degli Studi di Padova

Department of Geosciences

Ph.D. COURSE IN: Earth Sciences

SERIES XXXV

INVESTIGATION OF SEISMIC SLIP IN EXPERIMENTAL FAULTS UNDER HYDROTHERMAL CONDITIONS

Thesis written with the financial contribution of China Scholarship Council

Coordinator: Prof. Claudia Agnini

Supervisor: Prof. Giulio Di Toro

Co-Supervisor: Dr. Lu Yao

Ph.D. student: Wei Feng

Abstract

Rock stiffness and the evolution of rock friction with slip velocity and slip displacement control earthquake mechanics and the seismic cycle. This physical interpretation is also based on rock friction experiments where low (~1 μm/s, sub-seismic) to high (~1 m/s, seismic) slip velocities were imposed on experimental faults. However, the investigation of rock friction under hydrothermal conditions at slip velocities (0.01-1 m/s) and displacements (> 0.1 m) typical of earthquakes has been partly hampered by technical challenges. In this thesis, I aim at better understanding the frictional behavior of experimental faults in the presence of hot and pressurized fluids during the seismic cycle by means of rotary shear experiments and micro-analytical investigations.

First, I investigated the effect of the physical state of water on frictional strength. Experimental results show that in the presence of pressurized water in liquid and supercritical states, compared to in vapor state (and dry conditions), weakens the fault strength of gabbro of 50-60% at sub-seismic slip velocities (e.g., 10 μm/s).

Then, I performed slide-hold-slide experiments under hydrothermal conditions to investigate frictional healing during the seismic cycle. The results show that the log-linear relation between frictional healing and hold time is relaxed at high temperatures and, especially, in the presence of fluids. This behavior is attributed to the contrasting effects of contact area increase vs. contact strength decrease of the asperities during the holds.

Finally, I studied the slip dependence of frictional stability in large displacement experiments performed on gouges at conditions close to brittle-ductile transition. The results show that the transition from velocity-weakening (potentially unstable) to velocity-strengthening (stable) behavior is promoted by slip displacement and is associated with the transition from localized to distributed deformation in the gouge layer.

The results presented in this thesis challenge in some cases our current knowledge of rock friction under hydrothermal conditions and may provide new insights into the mechanical behavior of faults during the seismic cycle.

Keywords: Hydrothermal conditions, Fluid-rock interaction, Fault strength, Frictional healing, Frictional stability, Seismic cycle, Long slip displacement

Riassunto

La rigidità della roccia e l'evoluzione dell'attrito con la velocità e la distanza di scivolamento controllano la meccanica dei terremoti e il ciclo sismico. Questa interpretazione fisica si basa anche su esperimenti di attrito nelle rocce effettuati a basse (~1 mm/s, sub-sismiche) e alte (~1 m/s, cosismiche) velocità di scivolamento. Tuttavia, lo studio dell'attrito delle rocce in condizioni idrotermali e a velocità di scivolamento (0,01-1 m/s) e per rigetti (> 0,1 m) tipici dei terremoti è stata in parte ostacolata da problemi tecnici. In questa tesi, mi propongo di comprendere meglio il comportamento dell'attrito di faglie sperimentali in presenza di fluidi caldi e pressurizzati durante il ciclo sismico, mediante esperimenti condotti con macchine tipo *rotary* e indagini microanalitiche.

Nella prima parte della tesi, ho studiato l'effetto dello stato fisico dell'acqua sul coefficiente di attrito. I risultati sperimentali mostrano che la presenza di acqua pressurizzata allo stato liquido e supercritico, rispetto a quella allo stato di vapore (e in condizioni asciutte), abbassa il coefficiente d'attrito di una faglia di gabbro del 50-60% a velocità di scorrimento sub-sismiche (e.g., 10 mm/s).

Ho quindi effettuato esperimenti in condizioni idrotermali per studiare l'attrito delle faglie nella fase intersismica del ciclo sismico. I risultati mostrano che la relazione log-lineare tra l'incremento di attrito e tempo di contatto si riduce ad alte temperature e, soprattutto, in presenza di fluidi. Questo comportamento è attribuito agli effetti contrastanti dell'aumento dell'area di contatto rispetto alla diminuzione della forza di contatto delle asperità durante il tempo di contatto (o intersismico).

Ho infine studiato la dipendenza della stabilità dell'attrito con il rigetto effettuando esperimenti su polveri di roccia deformate a temperature e pressionei prossime a quelle della transizione fragile-duttile. I risultati sperimentali mostrano che la transizione da comportamento *velocity-weakening* e potenzialmente instabile a *velocity-strengthening* e stabile avviene all'aumentare del rigetto ed è associata alla transizione da una deformazione localizzata a distribuita nello strato di polvere.

I risultati presentati in questa tesi sfidano in alcuni casi le nostre attuali conoscenze sull'attrito delle rocce in condizioni idrotermali e forniscono nuove possibili interpretazioni sul comportamento meccanico delle faglie durante il ciclo sismico.

Parole chiave: Condizioni idrotermali, Interazione fluido-roccia, Resistenza della faglia, Attrito statico, Stabilità dell'attrito, Ciclo sismico, Esperimenti con grandi rigetti

Contents

Abstract ..... **ii**

List of symbols ..... **vii**

Chapter 1 Introduction **1**

1.1 Motivations 1

1.2 Fault zone structure 3

1.3 The seismic cycle 4

1.4 Fault friction 7

1.4.1 Rate-State friction law and friction at nucleation velocities 10

1.4.2 Friction at seismic slip velocities 13

1.5 Brittle-ductile transition 14

1.6 Rock-fluid interaction 16

1.7 Objectives and structure of this thesis 17

Chapter 2 Methods **20**

2.1 Rotary shear machines 20

2.2 Hydrothermal vessel 22

2.3 Sample assembly 26

2.4 Experimental materials 29

2.5 Data processing 31

2.6 Microanalysis of experimental products 32

Chapter 3 Physical state of water controls friction of gabbro-built faults **34**

3.1 Abstract 35

3.2 Introduction 35

3.3 Methods 37

3.4 Results 43

3.4.1 Mechanical data 43

3.4.2 Microanalysis of deformed samples 47

3.5 Discussion 52
3.6 Conclusions 59
3.7 Appendices 59
3.7.1 Modeling of the temperature evolution in the slipping zone 59
3.7.2 Micro-Raman spectroscopy data 61
3.7.3 Data from the experiments performed at effective normal stress of 20 MPa 61
3.7.4 Microstructures of deformed samples 63
Chapter 4 Frictional healing of gabbro-built fault gouges under hydrothermal conditions 67
4.1 Abstract 68
4.2 Introduction 68
4.3 Methods 70
4.4 Results 74
4.4.1 Mechanical data 74
4.4.2 Microanalysis of starting and deformed gouges 78
4.5 Discussion 81
4.5.1 Interpretation of experimental observations 81
4.5.2 Geophysical implications 84
4.6 Conclusions 85
4.7 Appendices 86
Chapter 5 Slip-dependence of frictional stability of simulated faults under hydrothermal conditions 90
5.1 Abstract 91
5.2 Introduction 91
5.3 Methods 93
5.3.1 Starting materials 93
5.3.2 Friction experiments 93

5.3.3 Microstructural analysis 97
5.4 Results 98
5.4.1 Mechanical Data 98
5.4.2 Microanalysis of deformed samples 101
5.5 Discussion 107
5.5.1 Slip-dependence of the frictional behavior 107
5.5.2 Geological implications 110
5.6 Conclusions 112
5.7 Appendices 112
6 Conclusions and Perspectives 116
6.1 Main results of the thesis 116
6.1.1 Frictional strength 116
6.1.2 Frictional healing 117
6.1.3 Frictional stability 118
6.2 Implications for the seismic cycle 119
6.3 Future work 120
6.3.1 High velocity ($V \geq 1$ m/s) experiments 120
6.3.2 Mechanisms responsible for decreased frictional healing 122
Bibliography 123
Appendices 150
Appendix A Preliminary data on frictional healing in basalt-built gouges 150
Appendix B High-velocity frictional properties of gabbro- and marble-built faults under hydrothermal conditions 152
Acknowledgements 158

List of symbols

$\Delta\mu_r$	Frictional relaxation
$\Delta\mu$	Frictional healing
β	Healing rate
η	Fluid viscosity, Pa·s
κ	Thermal conductivity, W/(mk)
μ_p	Peak friction
μ_{ss}	Steady state friction
μ_s	Static friction
μ	Coefficient of friction
θ	State variable, s
σ_{eff}	Effective normal stress, Pa
σ_n	Normal stress, Pa
σ_{n_1}	Maximum principal stress, Pa
σ_{n_3}	Maximum principal stress, Pa
τ	Shear stress, Pa
A	Nominal area, m^2
a	Direct effect of rate and state law
A_r	Real contact area, m^2
b	Evolution effect of rate and state law
d	Slip displacement, m
d_c	Critical slip distance, m
H	Thickness, m
K	Stiffness, Pa/m
K_c	Critical stiffness, Pa/m
L	Characteristic length for elasohydrodynamic, m
P_p	Pore fluid pressure, Pa

S	Sommerfield number
T	Temperature, ℃
t	Time, s
t_h	Hold time, s
V	Slip velocity, m/s
V_c	Critical slip velocity, m/s
V_{eq}	Equivalent slip velocity, m/s
w	Axial displacement, m
z	Dilatation or shortening, m

Chapter 1 Introduction

1.1 Motivations

With about 700,000 deaths in the 21st century, earthquakes are currently the leading cause of casualties by natural disasters worldwide (https://ourworldindata.org/natural-disasters). Geophysical, seismological and geological evidence, borehole data and other field studies in both tectonic and volcanic environments suggest that earthquakes are often genetically and spatially related to fluid circulation at conditions of elevated temperature and fluid pressure (i.e., hydrothermal fluids: Raleigh et al., 1972, 1976; Yukutake et al., 2011; Gomila et al., 2021; Scholz, 2019; Sibson, 2020, Ross et al., 2020). The presence of hydrothermal fluids interacting with the rock strongly governs the fault mechanics and seismic cycle. On the one hand, the increase in pore fluid pressure may result in fault weakening and failure, while the decrease may stabilize faults (Sibson, 2020). On the other hand, fluid-rock interaction can trigger chemical reactions and processes, e.g., mineral dissolution and precipitation, kinetic reduction of fracture energy, and sub-critical crack growth, which affect the frictional stability and strength of faults (Orowan, 1944; Rutter, 1972; Atkinson, 1984; Schott et al., 2009; Wintsch et al., 1995; Verberne et al., 2015; Moore and Lockner, 2013).

These considerations are also valid for human-induced seismicity, particularly associated with the exploitation of geothermal reservoirs. Currently, in medium- to high-enthalpy geothermal fields (temperature of fluids $100 < T < 450$°C) the most common way of capturing geothermal energy is to inject water in relatively deep reservoirs (e.g., 0.5-5 km depth) and then recover the heated water at the Earth's surface (Barbier, 2002; Islam et al., 2022 and references therein). However, injecting fluids into underground reservoirs affects the mechanical behavior of the rock mass. In fact, an increase in seismicity associated with deep water injection has been often recorded (Baisch et al., 2010; Cornet et al., 2007; Mukuhira et al., 2010; Diechmann and Giardini,

2009; Asunuma et al., 2005). Consequently, comprehensive knowledge of fluid-rock interactions, fluid-induced seismicity and a better understanding of the associated fault behavior are necessary for the safe and efficient exploitation of deep geothermal energy.

Despite the importance of fluids in earthquake mechanics, it is still poorly known how fault mechanics and the seismic cycle are affected by the presence of hot and pressurized fluids. Fault friction, together with elastic properties of the fault zone and host rocks, plays a significant role in the creeping vs. stick-slip behavior of faults, nucleation of earthquakes, as well as in controlling coseismic fault slip, rupture speed, ground motions, etc. (Brace and Byerlee, 1966; Dieterich, 1972; Heaton, 1990; Rice, 2006; Di Toro et al., 2011; Marone, 1998; Scholz, 2019). Great success has been achieved in understanding the stability of fault slip, nucleation of earthquakes and dynamic weakening mechanism in the past decades by performing low (~1 μm/s, sub-seismic conditions) to high (~1 m/s, seismic conditions) velocity friction experiments (Brace and Byerlee, 1966; Dieterich, 1978; Blanpied et al., 1991; Marone, 1998; Yao et al., 2016; Violay et al., 2014; Tullis, 2015; Di Toro et al., 2011; Niemeijier et al., 2012; Verberne et al., 2014; Goldsby and Tullis, 2011; Ikari et al., 2011). However, the physical-chemical processes that govern the fault behavior under realistic conditions typical of earthquake hypocentral depths are still poorly understood. Extrapolating the experimental results to natural conditions is still an extremely challenging task. In fact, for “low velocity” experiments, usually performed with bri-axial or tri-axial machines, though in some cases hydrothermal conditions can be imposed, the shear displacement is limited to several millimeters neglecting the effect of cumulative displacement (He et al., 2007; Moore et al., 2021; Stesky et al., 1974; Blanpied et al., 1991; Chen et al., 2015). For “high velocity” experiments, aiming at reproducing coseismic fault slip, the implementation of hydrothermal conditions in rotary shear machines has been hindered by technical difficulties leaving high-velocity (or coseismic) friction properties of faults under realistic crustal conditions still ambiguous (Di Toro et al., 2011). Therefore, experiments that can overcome these limitations are motivated to provide insights into

the mechanical behavior of natural faults in the seismic cycle (Harbord et al., 2022; Violay et al., 2021; Niemeijer et al., 2008).

1.2 Fault zone structure

It is well known that earthquakes are a result of ruptures, which nucleate, propagate and terminate mostly along pre-existing faults (Gilbert, 1909; Scholz, 2019 for a review). Field geology, seismological and geophysical studies and drilling projects of active faults have demonstrated that the crustal fault zone mainly comprises four domains: slip zones, fault core, damage zone and country rock (Caine et al., 1996; Sibson and Rowland, 2003; Faulkner et al., 2003; Mitchell and Faulkner, 2009; Chester and Logan, 1986) (Figure 1.1).

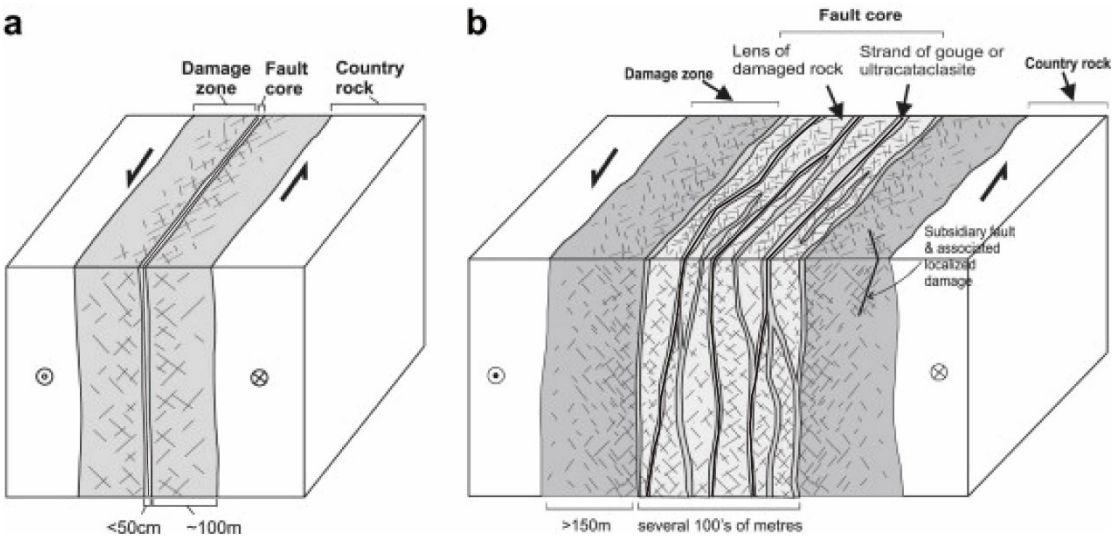

Figure 1.1: Typical fault zone structures in quartzo-feldspathic rock, 0.1 mm- to cm-thick slip zones are marked within the fault core (after Mitchell and Faulkner, 2009).

In the upper crust, shear strain is largely accumulated in individual 0.1 mm to cm-thick slip zone within the mm- to m- thick fault core, which often consists of in-cohesive gouge powder and (ultra)cataclasites as a result of abrasive wear and comminution (Caine et al., 1996; Sibson, 2003). The damage zone surrounding the fault core, typically 10 to 100 meters wide, is composed of a network of fractures, veins, secondary

faults and joints. The intensity of deformation decays away from the fault core into the undeformed host rocks (Faulkner et al., 2003; Mitchell and Faulkner, 2009).

Fault zone and its related properties (e.g., anisotropic permeability) play a significant role in controlling fluid flow, earthquake nucleation and the faulting process (Caine et al., 1996; Faulkner et al., 2010; Ben-Zion and Sammis, 2003; Mitchell and Faulkner, 2012). The evolution of fault structure depends highly on depth, lithology, accumulative slip history and tectonic environment (Savage and Brodsky, 2011; Shipton et al., 2001; Bistacchi et al., 2010; Masoch et al., 2021).

1.3 The seismic cycle

Earthquakes are a dynamic process, mostly occurring on pre-existing faults (Scholz, 2019). To explain this phenomenon, Reid (1910) proposed the elastic rebound model according to which earthquakes are the result of the unbalance between elastic strain accumulation in the country rocks and its sudden release, and between frictional strength and forces in the fault slip zone. Relative motion between two plates of an active but locked fault can lead to increasing the shear stress and accumulate the elastic strain energy in the rock mass. When shear stress is raised sufficiently to overcome the fault strength, the sides of a fault move suddenly past each other, releasing the stored elastic energy. Over the recurrence interval of hundreds of years to millennia, individual faults may experience several deformation processes and different events under tectonic loading, referring to as the so called seismic cycle (Figure 1.2). The seismic cycle can be divided into four main stages (Scholz, 2019):

Interseismic stage: the fault is in a quasi-stationary state. The frictional strength of the fault increases over time, known as frictional healing (Marone, 1998). This restrengthening is a fundamental process in the seismic cycle as it controls the elastic strain energy storage in the country rocks, the earthquake occurrence interval and stress drop. This behavior has been widely investigated in the laboratory by performing slide-

hold-slide friction experiments, consisting of sliding at a constant slip velocity, stopping the driving velocity for a determined hold time, followed by resumption of slip at pre-hold slip velocity (Figure 1.3a). Frictional healing is defined as the difference between the peak friction upon re-shearing after hold and the pre-hold steady-state friction (Figure 1.3b). Previous experiments revealed that the frictional healing increases with the logarithm of the hold time (Figure 1.3c), which is interpreted to be the result of an increase in real contact area due to asperity creep (Dieterich, 1972; Dieterich and Kilgore, 1994) and in contact bonding (Li et al., 2011).

Preseismic stage: the accumulated stress sustained by the fault is approaching a critical threshold at which earthquakes can occur (that is, rupture propagation velocity of the order of km/s) (Heaton, 1990). The seismic rupture nucleates locally along the fault where the elastic strain energy is sufficient to be released. At this preseismic stage, faults may slip at very low velocities (i.e., nm/s). How slip evolves during the earthquake nucleation stage are enigmatic, Ellsworth and Bulut (2018) suggest that earthquakes are triggered by a series of foreshocks, and Tape et al. (2013) conclude that earthquakes transition from slow slipping to fast slipping rupture.

Coseismic stage: seismic ruptures propagate at high velocity (km/s) along the fault core and the fault wall rock suddenly accelerate to a slip velocity of ~m/s on average (Heaton, 1990). Rupture propagation and fault slip are accompanied by dynamic stress drop and the release of stored strain energy, which may allow the coseismic slip to be transferred also to the region beneath the seismogenic volume (i.e., where earthquake ruptures can nucleate). A significant reduction in fault strength may occur due to the activation of multiple dynamic weakening processes (Di Toro et al., 2011; Tullis, 2015; Wibberley and Shimamoto, 2005; Pozzi et al., 2021).

Postseismic stage: In the case of typical crustal faults, where moderate and large in magnitude earthquakes nucleate at 7 to 20 km depths, following the coseismic slip, afterslips may occur on the fault at both shallow (< 2-4 km depths) and deep (> 10-20

km) crustal levels as the result of stress redistribution and change in strain rate (Pollitz, 2015). For instance, transient deepening of aftershocks after the mainshocks has been recorded in Southern and Baja California and other areas (Schaff et al., 2002; Rolandone et al., 2004; Cheng and Ben-Zion, 2019), which may reflect the downward migration of the brittle-ductile transition at depth.

Because the faults are under continuous tectonic loading, the stages above can be repeated resulting in the seismic cycle. In addition to the fast fault slip velocity earthquake events, fault behavior in the crust can involve slow-slip velocity events, non-volcanic tremors, swarms, low-frequency earthquakes and stable creep, all of which are dependent on ambient pressure and temperature, pressure and composition of fluids, rock type, etc. and visco-plastic-elastic properties of the country rocks (Barbot, 2019; 2022; Ross et al., 2020; Leeman et al., 2016).

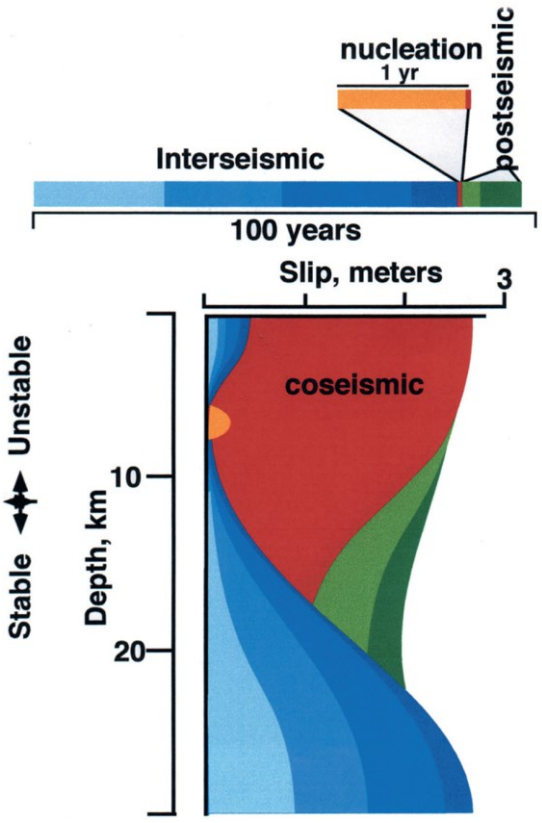

Figure 1.2: Fault slip as a function of depth in the seismic cycle, using a continental fault model loaded at 3 cm per year and with the unstable to stable transition at 11 km depth (Scholz, 2019)

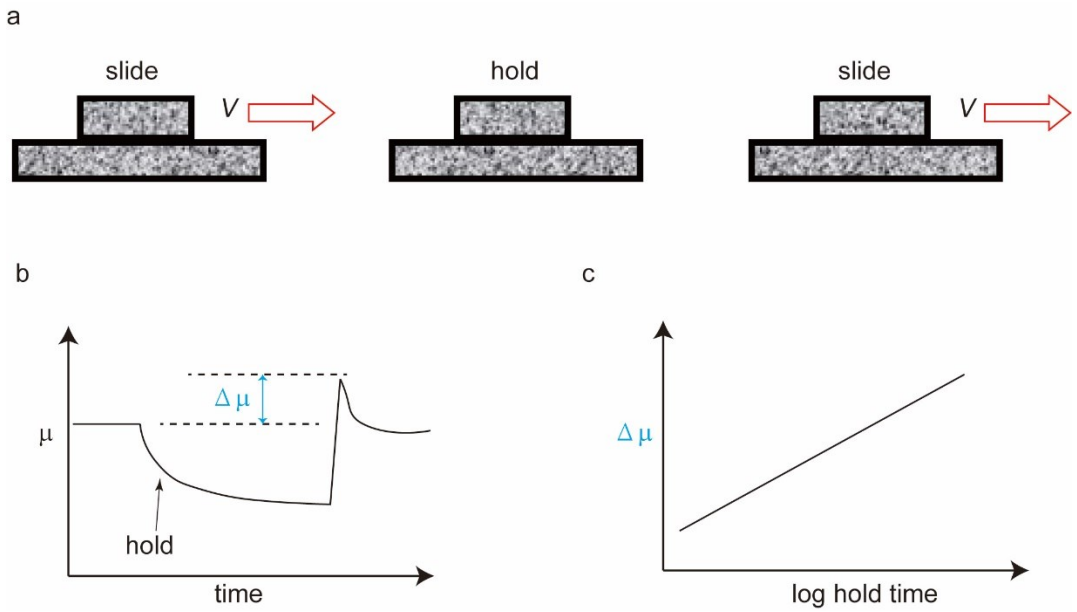

Figure 1.3: Schematic diagram of slide-hold-slide experiments. **a.** Experimental procedure consists in alternating sliding at a constant slip velocity with a stop for a determined period hold. **b.** Frictional healing is defined as the peak friction upon re-shearing minus steady-state friction before hold. Measured friction normally relaxes during the hold. **c.** Frictional healing typically increases linearly with the log hold time.

1.4 Fault friction

Friction is the force that resists the sliding of one object over another one along the contact surface. In 1699, Amontons developed two main laws of friction based on the understanding proposed by Leonardo da Vinci: 1) The frictional force is independent of the size of the contact surface, and 2) is proportional to the normal stress, which is well-known as "Amontons's law". He also found that the frictional force is about one-third of the normal force, while static friction force is about two-thirds of that. After then, Coulomb recognized that the contact surfaces were covered with asperities and observed an increase in static friction with the stationary time of contact surfaces. Later, Bowden and Tabor contributed to the concept of friction by proposing the adhesion theory which states that the real area of the contacting surface (A_r) is a fraction of the total contact area (A). Only the asperities in contact support the normal load and are

responsible for friction. This is a foundational concept for following studies on friction.

Fault friction is of importance in earthquake mechanics since once the fault zone is formed the relative motion of the wall rocks will be controlled by friction. The coefficient of friction (μ) is defined as the ratio of shear stress (τ) to the normal stress (σ_n) acting on the fault (i.e., $\mu = \tau / \sigma_n$). Based on experimental observations (Figure 1.4), Byerlee (1978) summarized that the frictional strength of rocks can be depicted by two relations for low and higher normal stress (*Byerlee's rule*, Figure 1.4):

$$\tau = 0.85\ \sigma_n, \text{ for } \sigma_n < 200 \text{ MPa} \qquad (1\text{-}1)$$

$$\tau = 50 + 0.6\ \sigma_n, \text{ for } \sigma_n > 200 \text{ MPa} \qquad (1\text{-}2)$$

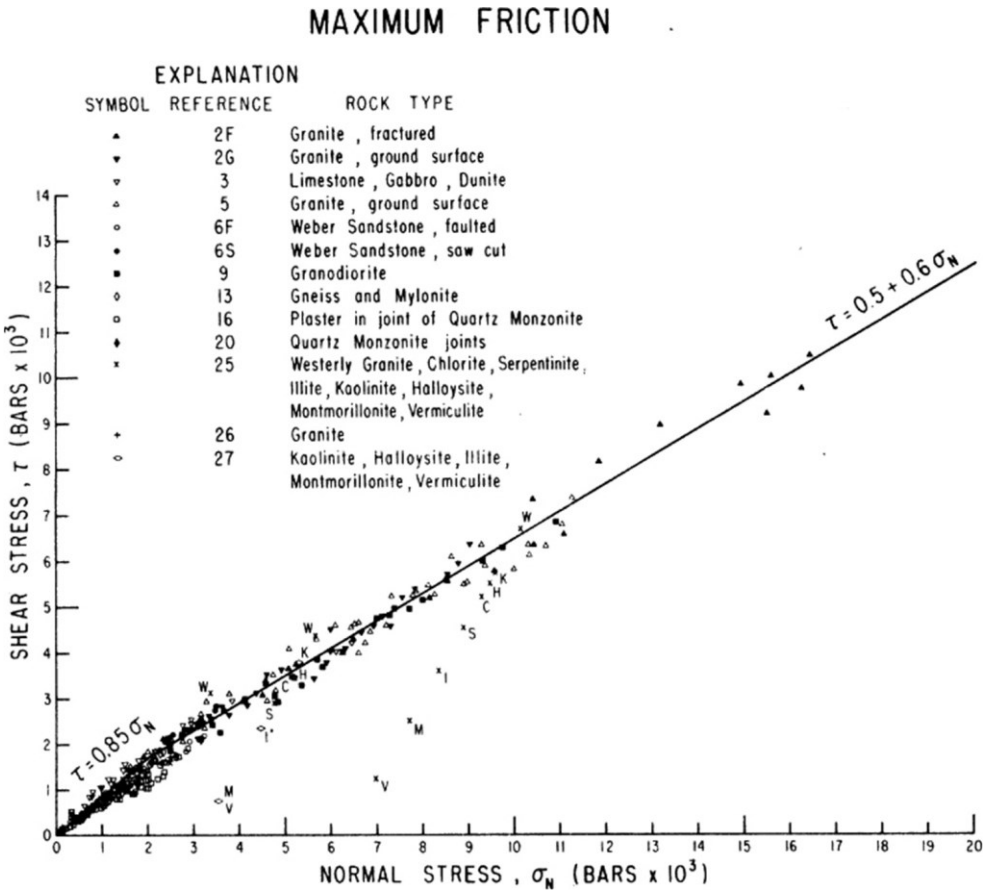

Figure 1.4: Shear stress versus normal stress for a variety of lithologies: the slope is about 0.6 (from Byerlee, 1978). However, there are exceptions to the so-called Byerlee law, and these are related to clay minerals and phyllosilicates (e.g., V = vermiculite, I = illite, M = Montmorillonite).

Considering the presence of pore fluid at a pressure of P_p in the slip zone, which acts against the stresses normal to the fault, the effective normal stress reduces to $\sigma_{eff} = \sigma_n - \alpha P_p$ assuming α=1. Hence, the friction strength is redefined as $\tau = \mu(\sigma_n - P_p)$ assuming cohesion is zero. In the Mohr space (i.e., description of the stress tensor), the reduced effective normal stress facilitates the reactivation of the fault by shifting the Mohr circle close to the failure criterion (Figure 1.5).

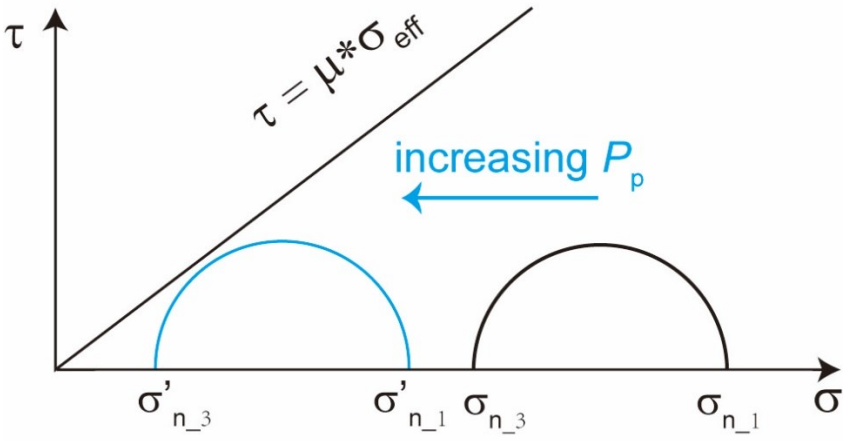

Figure 1.5: Mohr space diagram showing the increase in pore pressure shifts the Mohr circle to the left, approaching the failure envelope of the fault.

To investigate the frictional behavior of faults, friction experiments have been performed in the laboratory on a wide range of lithologies under varied experimental conditions (temperature, pressure, presence of fluids) and in different experimental configurations (bi-axial, tri-axial, rotary shear machines) (Stesky, 1978; Chester, 1994; Beeler et al., 1996; Frye and Marone, 2002; He et al., 2007; Moore and Lockner, 2008; King and Marone, 2012; Tesei et al., 2012; Mitchell et al., 2015; Verberne et al., 2015; Okamoto et al., 2019; Philips et al., 2020; Giacomel et al., 2021 and others). Most of the experiments show that frictional strength follows *Byerlee's rule*, i.e., the friction coefficient is between 0.6-0.85 regardless of lithology, normal stress, fluids, temperature and pressure (Figure 1.4). However, clay minerals and phyllosilicates

minerals with a plate-like structure have steady-state friction coefficients as low as 0.1, for instance, graphite (Collettini et al., 2019; Moore and Lockner, 2004). These minerals are often the products of fluid-rock interaction, in some cases under hydrothermal conditions and can determine the strength of the fault zone (Wintsch et al., 1995). Moreover, in the last 30 years, a large body of friction experiments performed, also under hydrothermal conditions, suggests that fault strength is strongly dependent on temperature, fluids, normal stress, slip velocities and slip history (Di Toro et al., 2011; Goldsby and Tullis, 2002; Morrow et al., 2000; Beeler et al., 1996; King and Marone et al., 2012).

1.4.1 Rate-State friction law and friction at nucleation velocities

Earthquakes are usually accompanied by sudden fault slip releasing stored elastic energy in the wall rocks. The stick-slip motion, a sudden movement often observed in frictional sliding, has been proposed as an analogue for an earthquake (Brace and Byerlee, 1966).

It is well known that earthquakes are only part of a wide spectrum of fault behavior, elastic strain energy can also be released slowly through slow-slip events, slow earthquakes, swarms and creeps (Scholz, 2019; Barbot, 2019; 2022; Ross et al., 2020; Leeman et al., 2016). These fault behaviors, divided into unstable and stable sliding, depend on effective normal stress, the frictional properties (velocity-dependence) of the fault and the stiffness of the surrounding rocks, which can be described by a spring-slider model (Burridge and Knopoff, 1967).

In order to discriminate the fault behavior whether unstable (seismic) or stable (aseismic), the Rate- and State Friction (RSF) law developed by Dieterich (1979) and Ruina (1983) describes the evolution of friction coefficient leading to the frictional instability and earthquake nucleation. In the RSF law, the friction coefficient μ is expressed as a function of slip velocity V and a state variable θ.

$$\mu = \mu_0 + aln\left(\frac{V}{V_0}\right) + bln(\frac{V_o\theta}{d_c}) \qquad (1–3)$$

Where μ_0 represents the steady-state friction coefficient at a reference velocity V_0, μ is the friction coefficient at slip velocity V. Parameters a and b are experimentally derived dimensionless constants, controlling the direct effect and the evolution effect in response to an instantaneous change in velocity, respectively. d_c is the critical slip displacement or the slip required to achieve the new steady-state frictional contacts upon the velocity perturbation. θ is a state variable with the units of time, which is assumed to represent the evolution of the microstructural state (Marone, 1998). The most widely used forms for the evolution of θ are "ageing law" (Dieterich, 1979) or the "slip law" (Ruina, 1983):

$$\frac{d\theta}{dt} = 1 - \frac{V\theta}{d_c} \qquad (1\text{-}4)$$

$$\frac{d\theta}{dt} = -\frac{V\theta}{d_c} ln \frac{V\theta}{d_c} \qquad (1\text{-}5)$$

In the ageing law, θ evolves with time when the fault is in quasi stationary state, while the evolution of θ requires slip in the slip law. Combining with either one of the two evolution laws, the RSF law has successfully reproduced the seismic or aseismic fault behavior and time-dependent frictional healing behaviors as observed in the laboratory as well as in nature.

In this model, the difference between the parameters a and b (i.e., a-b) is significantly important and can be used to determine the frictional stability of the fault. If a-b >0, the frictional strength increases with increasing slip velocity, i.e., the fault exhibits velocity-strengthening behavior and is intrinsically stable (Figure 1.6a). However, if a-b < 0, the fault exhibits velocity-weakening behavior (Figure 1.6b), the fault is conditionally unstable and earthquakes can nucleate if the elastic stiffness (K) of the surrounding rocks is less than the critical stiffness (K_c):

$$K < K_c = \frac{-(a-b)\sigma_{eff}}{d_c} \qquad (1\text{-}6)$$

The velocity dependence of friction is usually obtained from velocity-stepping friction experiments in which the slip velocity is generally changed by a factor of 10 or 1/10, typically at earthquake nucleation velocities ranging from 0.01 μm/s to 10 μm/s. Experimental results indicate the velocity dependence of friction depends on lithology (Ikari et al., 2011; An et al., 2021; Moore and Lockner, 2008), temperature (He et al., 2007; Verberne et al., 2015; Blanpied et al., 1995;), normal stress (Giacomel et al., 2021; Bedford et al., 2021), pore fluids (Bedford et al., 2021; He et al., 2006; 2007; Morrow et al., 2017), gouge size (Bedford et al., 2021), shear strain (Ikari et al., 2011) and so on (see also Spagnuolo et al., 2016). Moreover, and this is quite systematic, clay- or phyllosilicate-rich fault gouges with $\mu < 0.5$ at sub-seismic slip rates exhibit velocity-strengthening behavior, whereas fault gouges with higher μ exhibit velocity-weakening behavior (Ikari et al., 2011). In general, clays and phyllosilicates (talc, montmorillonite, etc.) tend to be velocity-strengthening while silicate minerals (quartz, feldspar, etc.) tend to be velocity-weakening, at least at room temperature conditions (Ikari et al., 2011 and references therein). In nature, frictional velocity-dependence is also related to fault maturity, for instance, velocity-strengthening transitions to velocity-weakening due to cementation or consolidation (Moore and Saffer, 2001; Marone and Saffer, 2007). In addition, the RSF law provides a good framework for simulating the frictional healing, earthquake nucleation processes, the seismic cycle and aftershock behavior in nature (Marone, 1998; Noda and Lapusta, 2013; Rice, 1993; Lapusta and Rice, 2003).

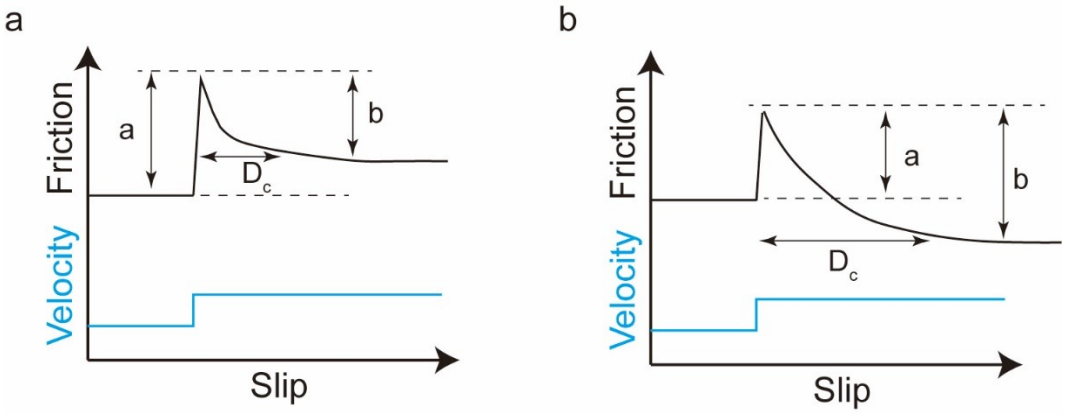

Figure 1.6: Schematic diagram of frictional response to velocity stepping according to the rate- and

state-friction law. **a.** velocity-strengthening behavior; **b.** velocity-weakening behavior.

1.4.2 Friction at seismic slip velocities

Once the earthquake has nucleated, fault ruptures will propagate at ~km/s and rocks bounding the fault will accelerate one relative to the other up to velocities of ~m/s (Heaton, 1990). To reproduce the co-seismic slip typical of moderate to large magnitude earthquakes, high-velocity (V> 0.1 m/s) rotary shear experiments have been extensively performed on a wide range of rock types. In these experiments, the faults show a dramatic reduction in frictional strength to as low as 0.1 at seismic slip velocities (Di Toro et al., 2011. Figure 1.7).

Under such sliding conditions, a variety of thermally-activated processes may be involved due to frictional heating, resulting in reduced friction strength. Numerous dynamic weakening mechanisms have been proposed based on experimental observations and modelling, including flash heating (Rice, 2006; Goldsby and Tullis, 2011), thermal pressurization (Sibson, 1973; Wibberley and Shimamoto, 2005; Noda and Shimamoto, 2005), powder lubrication (Reches and Lockner, 2010; Han et al., 2010), silica gel lubrication (Goldsby and Tullis, 2002; Di Toro et al., 2004), decomposition (De Paola et al., 2011), frictional melting (Di Toro et al., 2006; Nielsen, 2008; Niemeijer et al., 2011), elastochydrodynamic lubrication (Brodsky and Kanamori, 2001; Cornelio et al., 2019) and grain-size and temperature dependent plastic deformation (De Paola et al., 2015; Pozzi et al., 2021).

To date, the majority of high velocity experiments have been performed at ambient temperature under room humidity conditions and only few in the presence of pressurized pore fluids (Aretusini et al., 2021; Cornelio et al., 2019; Violay et al., 2014; Rempe et al., 2020). However, mostly because of technical limitations, performing high velocity experiments in the presence of hot and pressurized water (i.e., hydrothermal conditions) has still been hindered. Therefore, it remains unknown whether

hydrothermal conditions affect the weakening processes observed at room humidity and whether other weakening mechanisms may be activated.

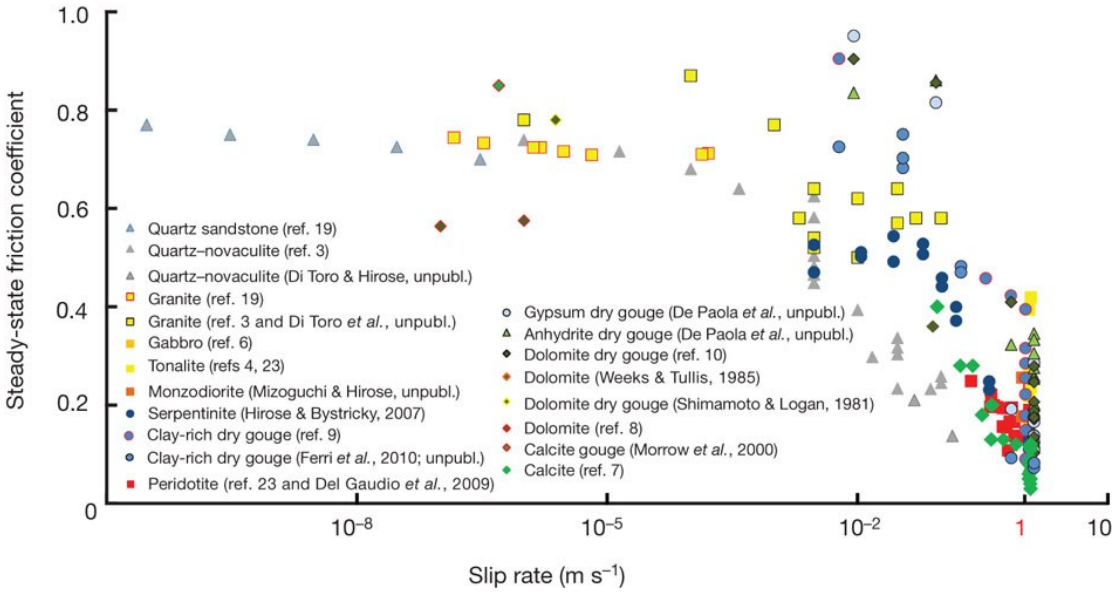

Figure 1.7: Steady-state friction coefficient versus slip rate for a wide range of lithologies. Friction coefficient dramatically decreases as slip rate approaches seismic slip rates (0.1~1 m/s). (Di Toro et al., 2011)

1.5 Brittle-ductile transition

Plate tectonics loading leads to two types of mechanical behavior of rocks: the so called brittle and ductile regimes (other rheological-dependent definitions are also used: elasto-frictional vs. viscous-plastic regime: Sibson, 1977). In the upper Earth's crust, strain is commonly accommodated in rocks in a localized fashion. Deformation is brittle microcracking where grains become cracked at the microscopic scale. The microcracks coalesce and form macroscopic fractures (Lockner et al., 1991; Paterson and Wong, 2005). At the crustal scale, tectonic loading builds up the strain on faults and the crustal strength is controlled by the friction of the faults. In the deep crust under high temperature and pressure, strain is accommodated by the viscous-plastic flow of rocks. Grains deform by dislocation or diffusion creep (crystal plasticity in general) at the microscopic scale. The crustal strength can be described by steady-state flow laws,

depending on the pressure, temperature and strain rate (Poirier, 1985). As a consequence, the constitutive laws for frictional and viscous-plastic behavior of rocks allows us to describe the strength distribution in the Earth's crust (Figure 1.8).

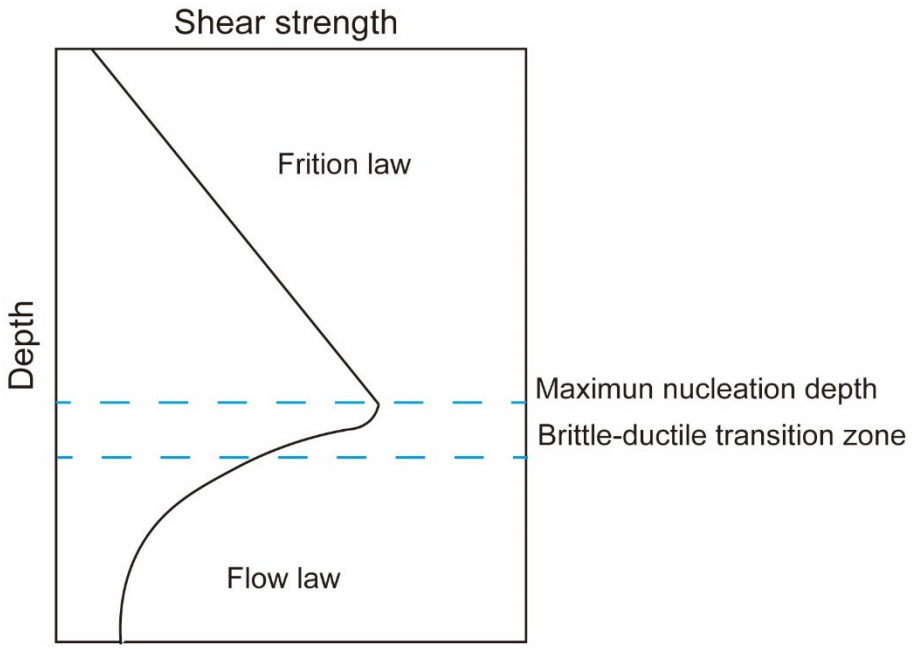

Figure 1.8: Schematic diagram of the shear strength-depth profile over the crustal depth. Shear strength is controlled by friction law in the upper crust, and transitions to viscous-plastic flow law with depth. The transition zone is also called known as the brittle-ductile (or, more rigorously, elasto-frictional vs. viscous-plastic, Sibson, 1977) transition zone.

The transition from brittle to ductile occurs over a certain depth where brittle and ductile deformation coexist, the so-called brittle-ductile transition zone. This transition is of major importance since it generally coincides with the maximum depth at which an earthquake can nucleate (Sibson, 1977; 1982) and it is the depth range where strength and elastic strain energy are at a maximum.

Experimental studies show that the transition from brittle to ductile depends mainly on confining pressure, temperature, fluids and strain rate. Specifically, an increase in confining pressure can result in brittle-ductile transition, for instance, in calcite-built rocks (Paterson 1958; Fredrich et al., 1989). With increasing confining pressure. the macroscale deformation transitions from axial splitting to single shear failure, to

conjugate fractures, and finally to considerable barrelling ductile deformation. In addition, an increase in temperature generally promotes the plasticity of silicate rocks by reducing the strength of crystalline slip systems (Paterson and Weaver, 1970). The addition of water can also weaken the rock samples and promotes plastic deformation in quartz (Griggs, 1967) and Westerly granite (Tullis and Yund, 1980). The rate of the deformation also strongly controls the brittle-ductile transition. For instance, decreasing the strain rate lowers the pressure necessary to achieve ductility in diabase (Caristan, 1982) and albite (Tullis and Yund, 1980).

1.6 Rock-fluid interaction

Interstitial fluid is almost ubiquitous within rock pores. Geophysical observations allow quantitative analysis of pore fluid volumes and pressures in various tectonic settings (Heise et al., 2013; Peacock et al., 2011). Borehole data and seismic studies reveal anomalous pore fluid pressure at shallow boreholes and within or adjacent to the faults (Davis and Villinger, 2006; Sibson and Rowland, 2003; Kato et al., 2010; Park et al., 2010).

The presence of pore fluid can alter the local pressures and reduce the effective normal stresses (Terzaghi effect: Rutter, 1972), as discussed above. The elevated pore pressure has been used to explain apparent weakness within fault zones (Moore et al., 1996; Tobin and Saffer, 2009) and also interpret the occurrence of slow-slip events, episodic tremors and low-frequency earthquakes (Audet et al., 2009; Shelly and Hardebeck, 2010; Shelly et al., 2006; Ito and Obara, 2006).

In addition to the mechanical effect, numerous studies suggest that fluid-rock interaction can also trigger chemical processes (Paterson and Wong, 2005; Lisabeth and Zhu, 2005; others), including mineral dissolution and precipitation (Rutter, 1972; Zhang and Spiers, 2005), formation of new minerals (Dunkel et al., 2017; Kanakiya et al., 2017) and sub-critical crack growth (Askinson, 1982; Brantut et al., 2013), which

may contribute to the deformation and lead to the strengthening or weakening of the faults (Wintsch et al., 1995).

Physical and chemical interactions between fluid and rocks can produce a spectrum of deformation behaviors, which should be taken into account in unraveling the deformation mechanisms of fault rocks during the seismic cycle.

1.7 Objectives and structure of this thesis

Numerous experimental and numerical modeling studies have indicated that (hydrothermal) fluids govern fault strength, earthquake rupture propagation and the seismic cycle (Blanpied et al., 1992; Wibberley et al., 2005). Presence of fluids contributes to the activation of a plethora of physical and chemical processes including, for instance, pore pressure-dependent processes (Terzaghi effect), diffusive mass transfer, pressure solution, etc. Conducting rock deformation experiments in the presence of fluids is a promising way to better understand the fault behavior and reveal the earthquake mechanics. However, it is still technically challenging to perform rock friction experiments covering the entire slip velocity range during the seismic cycle and in the presence of hot and pressurized fluids. New experimental machines, devices and dedicated experiments are required (Harbord et al., 2022; Violay et al., 2021; Niemeijer et al., 2008).

In light of this, the objectives of this thesis are:

1. To describe a new experimental device/configuration that allowed me to perform rock friction experiments under hydrothermal conditions (i.e., presence of hot and pressurized water in liquid, vapor and supercritical state) and over a wide range of imposed slip velocities (from sub- to seismic or cm/y to m/s) and realistic fault slip displacements (up to several meters). In **Chapter 2: Experimental methods**, I introduce a new-developed hydrothermal vessel installed on a low to high velocity

rotary shear machine. The sample assembly and experimental materials are also presented.

2. To characterize the frictional strength of experimental faults under hydrothermal conditions and the role of the physical state of pore water on the frictional strength. In **Chapter 3: Physical state of water controls friction of gabbro-built faults**, I describe a series of friction experiments performed on cylindrical gabbro at a constant velocity ranging from 1 μm/s to 0.1 m/s in the presence of water at liquid, vapor and supercritical state. In the experiments, the friction coefficient decreases with increasing slip velocity under vapor conditions (like under room humidity conditions, e.g., Hirose and Shimamoto, 2005; Niemeijer et al., 2011; Di Toro et al., 2011) but, quite surprisingly, it decreases with slip displacement regardless of the slip velocity under the liquid and supercritical water conditions. The content of this chapter is under review in *Nature communications*.

3. To investigate frictional healing (strength recovery) of experimental faults under hydrothermal conditions. In **Chapter 4: Frictional healing of gabbro-built fault gouges under hydrothermal conditions**, I describe Slide-Hold-Slide experiments on gabbro-built gouges at an effective normal stress of 50 MPa, temperatures from 25 to 400°C, under dry or pore pressure (30 MPa) conditions. The experiments show that the well-known linear relation between frictional healing and the hold time is strongly relaxed under these extreme conditions, especially for long-lasting holds, and in some cases and the frictional healing rate switches from positive to negative with increasing hold time. The content of this chapter is in preparation for submission to *Geophysical Research letters*.

4. To determine the frictional stability of experimental faults under hydrothermal conditions. In **Chapter 5: Slip-dependence of frictional stability of simulated faults under hydrothermal conditions**, I describe a series of velocity-stepping (from 16 nm/s to 10 μm/s, five orders of magnitude) experiments on gabbro and basalt at T=300 and

400°C, normal stresses of 50 or 100 MPa conditions. The experimental results show that instability (velocity-weakening) transitions to stability (velocity-strengthening) with cumulative displacement. This chapter is intended for submission to *Geophysical research letters*.

Chapters 3 to 5 have been structured as scientific papers and include the abstract, introduction, methods, results, discussion and conclusion sections. In Chapter 6, I summarize the main results of my thesis and propose future studies on the topic. In Appendices, Appendix A is preliminary data of frictional healing on basalt-built gouges. Appendix B is ongoing work on high velocity experiments of gabbro- and marble-built faults (I am a co-author, my contribution was to run the friction experiments and assist with microstructural work).

Chapter 2 Methods

The experimental work presented in this thesis was conducted at the Department of Geosciences, University of Padova (UNIPD) and at the Laboratory of Tectonophysics, Institute of Geology, China Earthquake Administration (IGCEA). This chapter gives an outline of the rotary shear machines, the new hydrothermal vessel, the experimental materials and the microanalytical techniques exploited. Specific and detailed procedures for the friction experiments are presented in each chapter.

2.1 Rotary shear machines

The friction experiments were conducted using a rotary-shear Low to High-velocity apparatus (LHVR-Beijing) installed at the Institute of Geology, China Earthquake Administration in Beijing, China (Ma et al., 2014) and Rotary Shear Apparatus (RoSA) at the Department of Geosciences at the University of Padua, Italy (Rempe et al., 2014). Both designed by Prof. Toshihiko Shimamoto, these are very similar machines, though the LHVR has a power supply of 22 kW and RoSA of 11 kW. Since most of the experiments were performed in LHVR-Beijing, in this section I will focus on this machine (Figure 2.1). In fact, because of the impact of COVID-19, the installation of the hydrothermal vessel at the Department of Geosciences planned for June 2020 was delayed by nine months and the vessel was installed and tested in late March 2021. Moreover, the several COVID-19 pandemic waves and related closures of the Department resulted in further delays. The calibration and improvements to the machine and to the vessel required other nine months of work and the systematic production of reproducible experimental data started only in February 2022.

The LHVR-Beijing rotary machine is 3.2 m in height (Figure 2.1) and consists of a servomotor (1) with a power output of 22 kW supplying a maximum rotary revolution of 1500 rpm. The rotary piston (4) is connected to the motor through a gear/belt box (2) with a ratio of 1:1000:1000000, which allows the imposed angular velocity to cover

nine orders of magnitude (resulting in an equivalent slip velocity on standard samples, see below, spanning from 1 nm/s to 1 m/s). The angular velocity and rotary angle are recorded with the high-resolution encoder and potentiometer, respectively (3). For setting up each experiment, the upper rotating column was centered within 5 μm with respect to the loading frame axis. The hydrothermal vessel (5) and rock specimen assembly are placed along the rotary axis in the center of the machine. Normal (axial) load up to 10 kN is applied to the samples with an air pressure-driven actuator (12), recently increased to 60 kN after the installation of a new air actuator. Normal load is measured with a load cell with a resolution of 10 N (11). Shear torque is recorded by the cantilever-type torque gauge (8) consisting of a horizontal arm and axial force gauges with a resolution of 0.01 Nm. The torque gauge assembly is connected to the axial column through a ball spline. Axial displacement (i.e., sample plus loading column) is measured by a linear voltage displacement transducer (LVDT) with a resolution of 1 μm (9). The acquisition rate ranges from 1 Hz to 25 KHz.

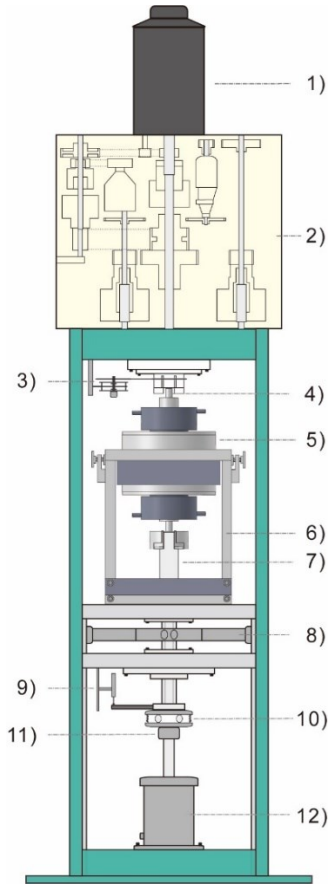

Figure 2.1: Schematic diagram of the Low to High-velocity rotary shear apparatus equipped with a dedicated hydrothermal vessel (LHVR-Beijing). 1) servomotor, 2) gear and belt system, 3) rotary encoder and potentiometer, 4) rotary shaft, 5) hydrothermal pressure vessel, 6) metal frame, 7) axial loading column, 8) cantilever-type torque gauge, 9) liner voltage displacement transducer, 10) thrust bearing, 11) axial force gauge, 12) air actuator.

2.2 Hydrothermal vessel

The hydrothermal pressure vessel (Figure 2.2), also designed by Prof. Toshihiko Shimamoto, consists of a pressure vessel, upper and lower glands (Figure 2.3), upper and lower nuts, an external furnace and two pistons (Shimamoto, 2022). This vessel is capable of imposing temperatures up to 500℃ and pore fluid pressures up to 70MPa on the specimens.

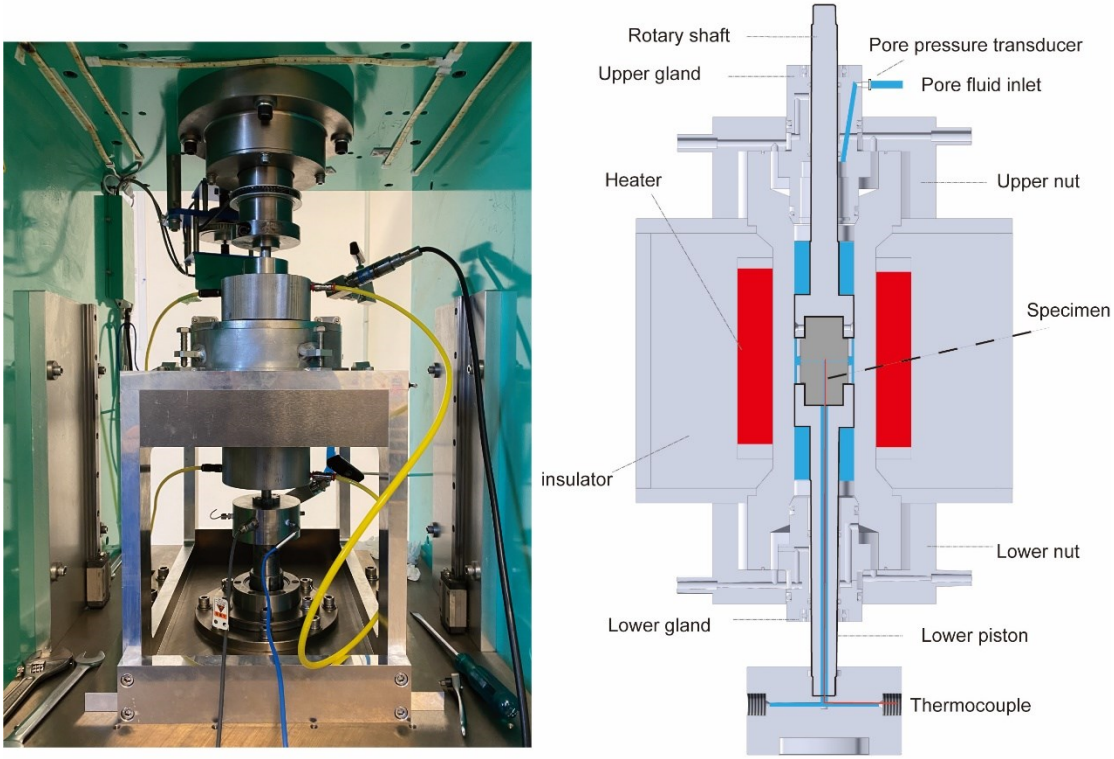

Figure 2.2: Photograph (left) and sketch (right) of the hydrothermal vessel with the main parts indicated in the diagram.

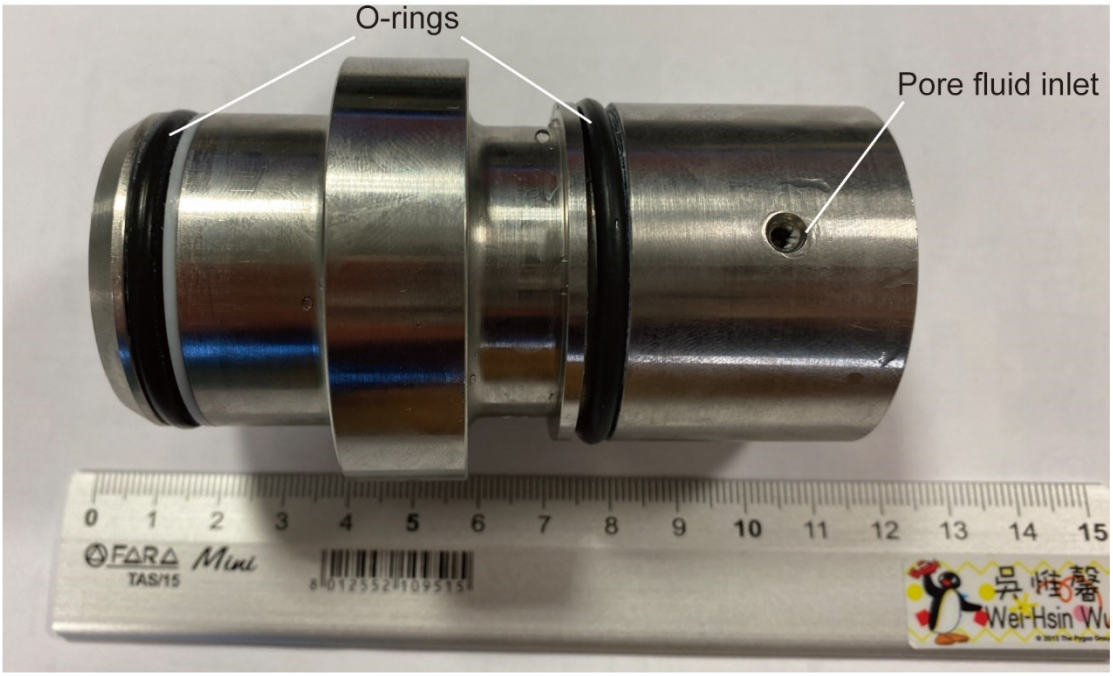

Figure 2.3: Photograph of the upper gland.

The furnace is set on the pressure vessel with furnace wires connected in parallel inside the furnace casing, which consists of an aluminum cylinder, upper and lower split lids, and an aluminum belt with a pair of aluminum shafts. The position of the furnace casing can be adjusted by means of four bolts. One K-type thermocouple is inserted into the interface between the pressure vessel and the furnace to measure the furnace temperature. The insulating material "Microtherm", consisting of silica and TiO_2 with a grain size of 5-25 nm and having thermal conductivities of 0.02-0.04 W/m K, one of the materials with the lowest thermal conductivity ever made, fills the furnace casing. To measure the sample temperature during the experiments, a K-type thermocouple is placed ~1 mm away from the slip surface. The thermocouple passes through a hole made on the axis of the lower stationary piston. A servo-controlled system installed in the furnace controlled based on the temperature measurements in the external furnace and in the sample chamber allows the operator to impose an almost constant temperature (e.g., temperature oscillations < 2℃ at 400℃) during the experiments (Figure 2.4).

Figure 2.4: Photograph of the furnace controller.

A syringe (ISCO) pump is connected to a pressure inlet in the upper gland and used to inject the pore fluid into the vessel chamber for the experiments with pressurized water (Figure 2.5). The pore pressure is measured by a pressure transducer (100 MPa full range with 0.01 MPa resolution) placed on the upstream side of the sample. In the case of RoSA in Padova, two pressure transducers are installed to monitor the upstream and downstream pore fluid pressure. Leakage of fluid from the vessel is impeded by a series of O-rings in the upper and lower glands. Since O-rings are made of rubber and must be protected from failure at high temperatures, an external chiller pumps cold water continuously into the glands and O-ring. The O-rings are lubricated with HT-resistant grease before the experiments. The upper and lower glands are made of Inconel 625 with a tensile strength of 850 MPa at temperatures up to 600°C. Moreover, the upper gland is equipped with two sets of ball bearings to prevent the jamming of the piston and gland. Two nuts with trapezoidal threads are used to hold the glands in position and also to provide channels for cooling water.

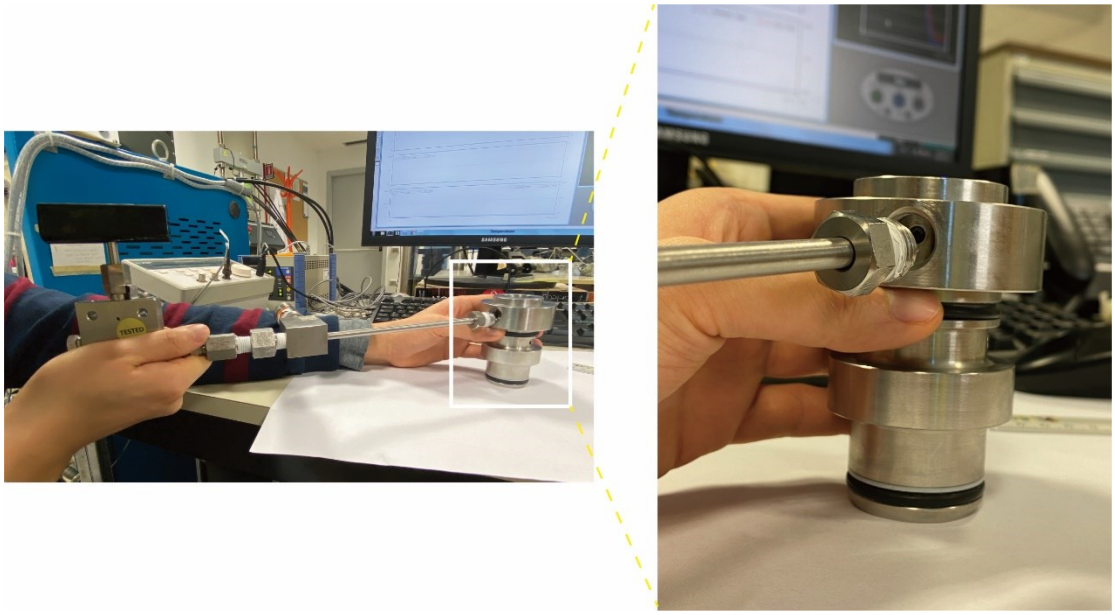

Figure 2.5: Photograph showing the connection of high pressure pore fluid inlet in the upper gland. A ring with screws is used as a connector.

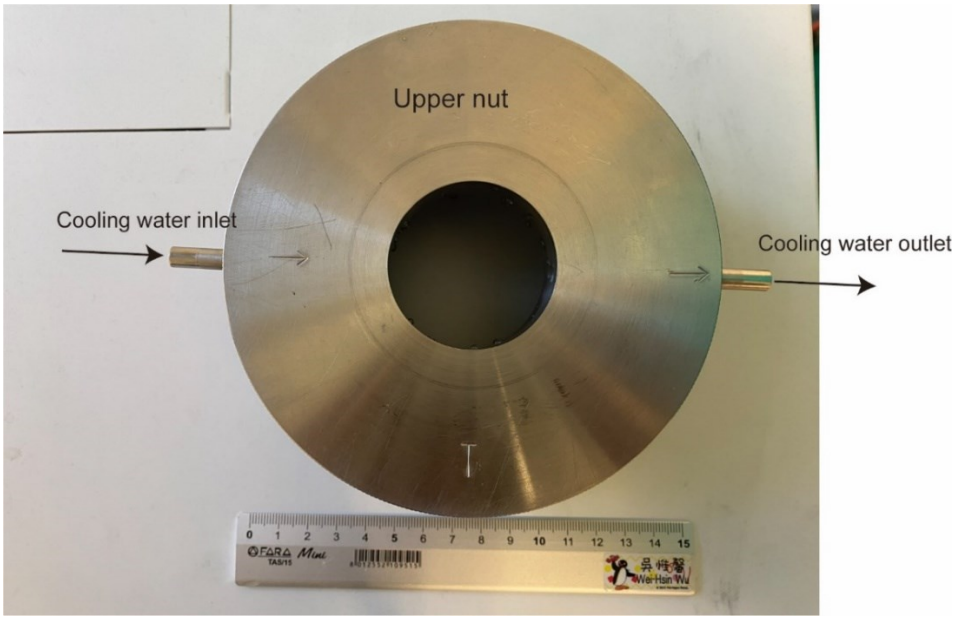

Figure 2.6: Photograph of the upper nut.

The upper piston (i.e., rotary piston) is connected to the column attached to the clutches and the rotary motor, and the lower piston (axial piston) is fixed tightly to the lower header block, which is connected to the lower axial column with a mechalock (Figures 2.1 and 2.2a). The axial and rotary pistons inserted into the hexagonal hole of the

columns of the LHVR machine can withstand sufficiently high torques and transmit the torque to the arm and to the installed gauges. The header block has four connectors allowing for the connection of thermocouples and pore pressure transducers. A 2 mm in diameter hole in the lower piston provides a channel for a thermocouple to pass through for measuring the temperature inside the vessel and close to the samples (Figure 2.3a).

2.3 Sample assembly

Upper and lower pistons with sample holders for cylindrical specimens are shown in Figure 2.7. The diameter of the pistons is 15 mm. Graphite rings of 20 μm diameter smaller (34.98± 0.005 mm) than the internal diameter (35.00 mm) of the vessel chamber are used as adjusters on the pistons for alignment and sustaining the pistons. The upper view of the sample holder is shown in Figure 2.7a. The rock cylinders are prepared after including coring, cylindrical grinding, saw cutting, and surface grinding. The samples ready for the experiments are 28.00±0.01 mm in diameter and ~25 mm in length. The lower part of the cylinder (from the bottom up to 12 mm) is cut to form two parallel surfaces. This technically challenging operation is made to allow the rock sample to be inserted and coupled to the sample holders for transmitting the torque, through the sample slip zone, from the upper rotary column to the lower axial column. In fact, because of the high temperatures (up to 500°C) imposed to the samples, glues (they breakdown and also release contaminating chemicals in the liquid and in the rock specimen) and mechanical clamps (they fail because of thermal expansion) cannot be used. A 2 mm hole is cored in the stationary-side rock to allow the thermocouple to pass through to reach the slip surface. Under hydrothermal conditions in our study, samples are jacketed with Nickel-made rings (Figure 2.7b) rather than Aluminum-made rings, commonly used for room-temperature experiments, to avoid rock failure during the shearing. Before loading to the machine, the rock surfaces are roughened with 80# silicon carbide.

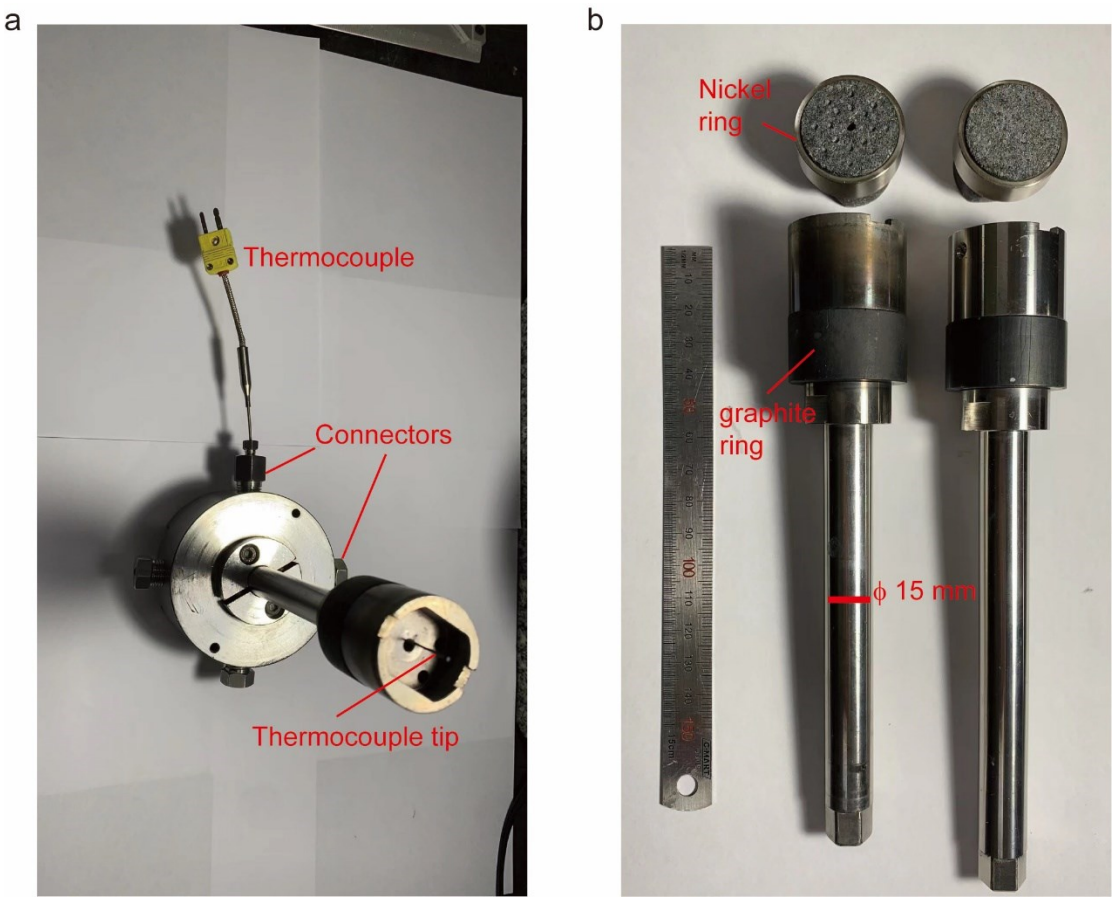

Figure 2.7: Photograph of piston assembly for cylindrical rock specimens **a-b**, showing the head block, thermocouple, pistons, and rock cylinders jacketed with Nickel-rings.

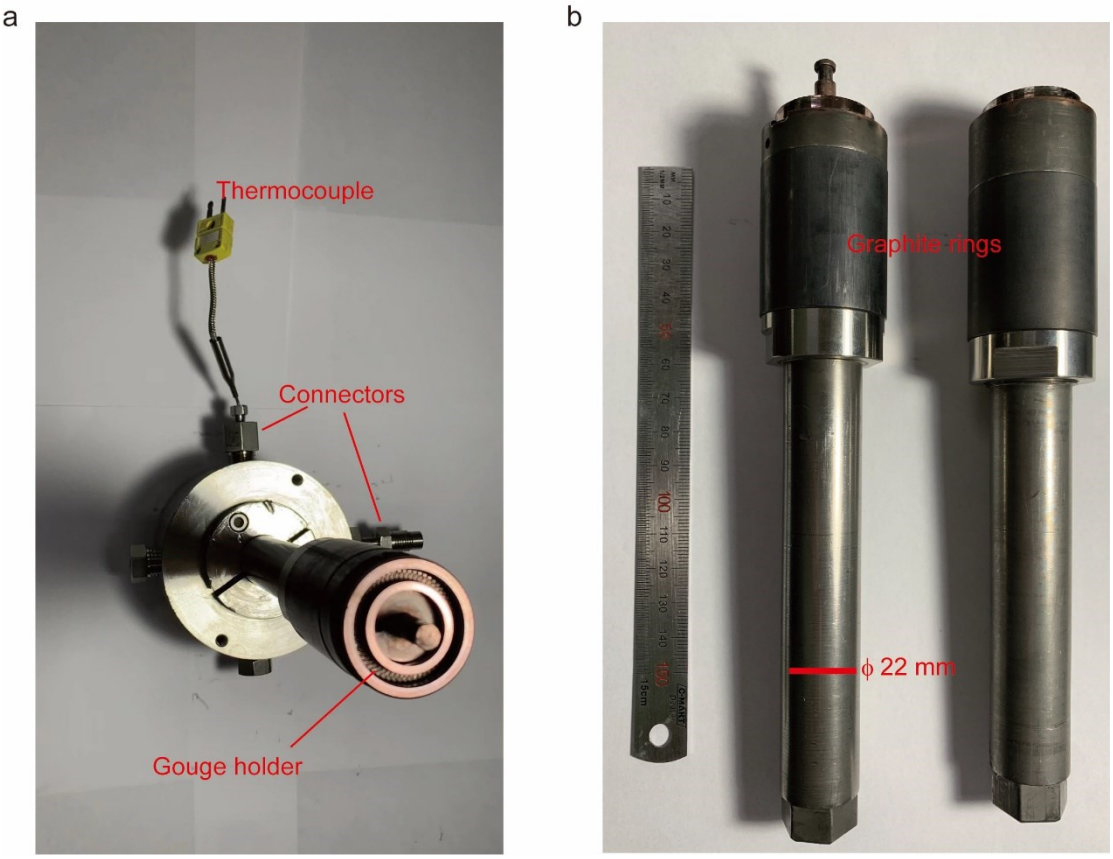

Figure 2.8: Labelled photograph of piston assembly for gouge experiments **a-b**. See text for description.

For gouge experiments, the diameter of the pistons is increased to 22 mm for improving the stiffness of the entire system (vessel plus sample holders: Figure 2.8). This increase in the diameter of the pistons required also the design and installation of new glands and header blocks. The gouges are prepared by crushing the bulk rock and sieving it to pass through a 180-mesh sieve (= grain size below 88 μm). The rock gouge is sandwiched between two ring-shaped pistons (22/28 mm inner/outer diameter, respectively, Figure 2.9). The surfaces of the metal holder are grooved with 0.25 mm in depth, 0.5 mm in width and 1 mm spacing to promote that shearing occurs within the gouge layers and not at the gouge-metal holder interface. The gouge layer is confined by inner and outer rings made of the same alloy (titanium/aluminum/vanadium, Ti90-Al6-V4) of the pistons to obtain the same thermal expansion coefficient and minimize the gouge extrusion during compaction and shearing. The confining rings are lubricated

with Molykote D-321R antifriction coating to minimize the extra torque to the measurement. These two pistons are attached to each other by a locking screw, housing the sample properly.

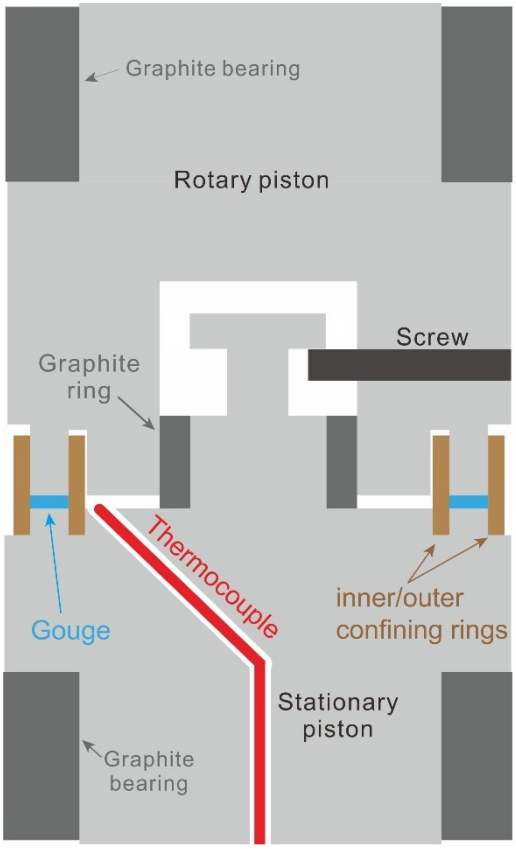

Figure 2.9: Schematic diagram of the sample assembly for gouge experiments (modified based on the sample assembly of the ring-shear machine at Utrecht University (Niemeijer et al., 2008)).

2.4 Experimental materials

Friction experiments are performed on gabbro and basalt. Gabbro, named "Jinan dark green" is supplied by a rock dealer in China, and basalt is collected from a quarry from the Etna in Italy. The mineralogical and chemical compositions are determined with X-Ray Powder Diffraction (XRD) and X-Ray Fluorescence (XRF), reported in Tables 2-1 and 2-2. Basalt consists of feldspar, augite, olivine, magnetite, and minor amounts of amorphous minerals (same material as reported by Giacomel et al., 2021), and gabbro consists of feldspar, pyroxene, olivine, and biotite. Both gabbro (intrusive igneous rock)

and basalt (extrusive igneous rock) are mafic in composition and typical rocks of the oceanic crust (and also of the lower continental crust in the case of gabbro), and can be found along plate boundary faults (transform, subduction faults), volcanic environments and geothermal reservoirs. Therefore, and because often homogenous and with small grain size (< 1 mm), gabbro and basalt rocks have been widely investigated in rock friction experiments. For instance, high-velocity experiments (Tsutsumi et al., 1997, 2007; Hirose et al, 2005; Di Toro et al., 2005; Mizoguchi et al., 2007; Niemeijer et al., 2011; Brown and Fialko, 2012; Violay et al., 2014a, b) or under hydrothermal conditions (He et al., 2006, 2007; Mitchell et al., 2015; Zhang et al., 2017).

Table 2-1: XRD results of gabbro and basalt

Gabbro	Phase Quantity (wt-%)	ESD (wt-%)
Biotite	4.0	0.2
Diopside	27.8	0.2
Dolomite	1.5	0.1
Forsterite	12.2	0.2
Lizardite	1.3	0.1
Magnetite	2.6	0.1
Andesine	47.4	0.3
Sanidine	2.8	0.1
Quartz	0.4	0.1
Basalt	Phase Quantity (wt-%)	ESD (wt-%)
Augite	23.2	0.3
Forsterite	5.1	0.2
Ilmenite	0.3	0.1
Magnetite	5.8	0.1
Nepheline	3.7	0.2
Olivine	5.0	0.3
Anorthite	5.3	0.4
Andesine	34.2	0.5
Phlogopite	1.0	0.1
Sanidine	11.3	0.4
Sodalite	1.3	0.1
Tridymite	0.6	0.1
Amorphous	3.1	0.7

Table 2-2: XRF results of gabbro and basalt

	SiO_2	TiO_2	Al_2O_3	Fe_2O_3	MnO	MgO	CaO	Na_2O	K_2O	P_2O_5	Tot
gabbro	50.36	0.54	14.23	9.76	0.16	10.61	10.66	2.50	0.80	0.13	99.75
basalt	47.54	1.70	16.73	11.61	0.18	5.69	9.66	3.85	1.55	0.56	99.07

2.5 Data processing

During the experiments, time, normal load, shear torque, angular position and velocity, axial compaction and dilation, temperature and pore pressure are acquired at a frequency of up to 25 KHz. All raw data are post-processed in MATLAB.

Because of rotary shear configuration, there is a gradient in tangential slip velocity ($V = \omega r$ with ω angular velocity and r sample radius) from the center (V = 0 m/s for r = 0 m) to the rim (V_{max}) of the cylindrical sample. So, we use "equivalent slip rate" V_{eq} as a slip velocity applied to the samples assuming shear stress independent of radial position (Shimamoto and Tsutusmi, 1994):

$$V_{eq} = \frac{4\Pi R\ (r_1^2 + r_1 r_2 + r_2^2)}{3(r_1 + r_2)} \qquad (2\text{-}1)$$

Where R is the revolution rate of the motor, r_1 and r_2 are the internal and external diameter of the samples (r_1 = 0 m for full cylinders). All the sample velocities referred to in this thesis are V_{eq}. Correspondingly, the slip displacement δ is "equivalent slip displacement" obtained by integrating V_{eq} with respect to time.

For processing the raw data recorded from each experiment, the normal stress (σ_n), shear stress (τ) and slip displacement (d) are converted from the measured normal load (F), shear torque (M) and rotary displacement (rev: the number of revolutions), respectively, using the following equations:

$$\sigma_n = \frac{F}{\Pi(r_2^2 - r_1^2)} \qquad (2\text{-}2)$$

$$\tau = \frac{3M}{2\Pi(r_2{}^3 - r_1{}^3)} \qquad (2\text{-}3)$$

$$d = rev\,\frac{4\Pi(r_1{}^2 + r_1 r_2 + r_2{}^2)}{3(r_1 + r_2)} \qquad (2\text{-}4)$$

Friction coefficient is defined by the ratio of shear stress to effective normal stress ($\mu = \tau/\sigma_{\text{eff}}$). The axial displacement data obtained are taken to calculate changes in the sample height (gouge layer thickness), though this measure includes also elastic deformation of the pistons and of the metal parts and their thermal expansion and cooling. The shortening or dilation is determined as $z = w_0 - w$, where w is measured axial displacement during the experiment and w_0 is initial axial displacement before shearing. Positive z means shortening (compaction), negative z dilation.

2.6 Microanalysis of experimental products

After the experiments, the solid rock samples or gouge layers are recovered carefully from the machine and prepared for further microanalysis. The techniques I used in this study include:

X-ray powder diffraction (XRPD): to determine the mineral assemblage before and after the experiments qualitatively and quantitively, XRPD measurements are performed at the Department of Geoscience at the University of Padova using a Philips X'Pert Pro MPD diffractometer. The instrument is equipped with a long-fine-focus cobalt anode tube working at 40 kV – 40 mA and a 240 mm goniometer radius that operates in the θ/θ geometry. Incident beam optics includes the Bragg-BrentanoHD (BBHD) module: a wafer crystal of W/Si manufactured to improve signal-to-noise and peak-to-background ratios while maintaining a divergent beam and reducing Kα-2 and Kβ lines. Divergence slits of ¼°, antiscatter slits of 1° and Soller slits of 0.04 rad complete the incident beam setup. Diffracted beam optics are composed of antiscatter slit of 9.1 mm aperture, Soller slits of 0.04 rad and X'Celerator Position Sensitive Detector with a 2.122° 2θ active length.

Micro-Raman spectroscopy: to determine vibrational modes of molecules of the samples before and after the experiments, Micro-Raman spectra are collected at the Department of Geoscience at the University of Padova, using WITec AlphaR confocal microscope with a XYZ motorized stage and equipped with the 532 nm laser diode (maximum power: 60 mW) and with a 300 lines/mm grating that ensures a ~2 cm-1 resolution over a spectral range from 0 to 4000 cm-1.

Field Emission Gun Scanning Electron Microscope: to obtain microstructure of the samples before and after the experiments to investigate the deformation processes, recovered samples are first impregnated with a low viscosity epoxy resin and then prepared into thin sections, cut in an orientation parallel to the shear direction and perpendicular to the shear plane. SEM images are collected on a Tescan Solaris Field-Emission SEM equipped with SE (secondary electrons) and BSE (back scattered electrons) detectors (resolution 1-2 nm) and Energy Dispersive X-ray Spectroscopy (SEM-EDS), wavelength-dispersive spectrometer (WDS), cathodoloumiscence (CL) and Electron Backscatter Diffraction (EBSD) at the Department of Geoscience at the University of Padova.

Non-contact optical profilometer: to quantify the roughness of the sample surface before and after the experiments, the surface morphometrics is performed at the Department of Geoscience at the University of Padova with a portable non-contact 3D optical profilometer Nanovea Jr25, equipped with an optical pen providing a vertical resolution (height repeatability) of 3.4 nm. The 3D maps are processed with the software Gwyddion v2.61 (Czech Metrology Institute).

Chapter 3 Physical state of water controls friction of gabbro-built faults

Authors: Wei Feng[1,2], Lu Yao[2], Chiara Cornelio[3], Rodrigo Gomila[1], Shengli Ma[2], Chaoqun Yang[4], Luigi Germinario[1], Claudio Mazzoli[1] and Giulio Di Toro[1,3]

[1] Dipartimento di Geoscienze, Università degli Studi di Padova, Padua, Italy

[2]State Key Laboratory of Earthquake Dynamics, Institute of Geology, China Earthquake Administration, Beijing, China

[3]Sezione Roma 1, Istituto Nazionale di Geofisica e Vulcanologia, Rome, Italy

[4]State Key Laboratory of Oil and Gas Reservoir Geology and Exploitation, Chengdu University of Technology, Chengdu, China

Status: Under review at *Nature Communications*

Contributions: W.F., L.Y. and G.D.T. conceived the study. W.F. and L.Y. performed the experiments. C.C. performed the temperature simulations. W.F. and R.G. carried out the microstructural analysis. L.G. and C. M. carried out the roughness analysis. W.F. wrote the first draft of the manuscript with inputs from L.Y. and G.D.T. All authors discussed and interpreted the results.

3.1 Abstract

Rock stiffness and the evolution of rock friction with slip velocity and slip displacement control earthquake mechanics and the seismic cycle. Because of this, rock friction has been investigated for decades with different experimental machines and configurations, also in the presence of hot and pressurized water (hydrothermal conditions) typical of earthquake nucleation depths. However, the investigation of rock friction under hydrothermal conditions at slip velocities (0.1-10 m/s) and slip displacement (> 0.3 m) typical of moderate to large magnitude earthquakes has been hindered by technical challenges. Here we exploit a new experimental device to investigate the frictional behavior of gabbro under hydrothermal conditions at seismogenic depths (e.g., water pressure and temperature up to 30 MPa and 400 °C, respectively) over a large range of imposed slip velocities (from 1 μm/s to 100 mm/s) and slip displacement (up to 3 m). These experimental conditions allow us to measure the evolution of fault friction in the presence of water under vapor, liquid and supercritical state. In particular, when pressurized water is in vapor state, the rock friction decreases with increasing slip displacement and slip velocity, similarly as in room temperature experiments. However, when pressurized water is in liquid or in supercritical state, friction decreases with slip displacement regardless of the imposed slip velocity. Based on the interpretation of mechanical data and microanalysis of experimental faults, we propose that water-rock interaction and elastohydrodynamic lubrication explain the experimental observations. The transition from the liquid to vapor state of water results in an abrupt increase in fault friction that can stop or delay the nucleation stage of an earthquake under hydrothermal conditions (e.g., geothermal fields).

3.2 Introduction

Seismological, geophysical and deep borehole data plus field observations of exhumed faults are consistent with the hypothesis that crustal earthquakes often originate and

propagate in the presence of hot and pressurized (i.e., hydrothermal) fluids (Scholz, 2019; Sibson, 2020, Ross et al., 2020). Moreover, experimental studies indicate that hydrothermal fluids (usually water) govern the seismic cycle by means of a plethora of physical and chemical processes (pore pressure variations, diffusive mass transfer, mineral precipitation, sub-critical crack growth, etc.) which determine, for instance, faults frictional instabilities or their healing and sealing (Sibson, 1973; Violay et al., 2014; Verberne et al., 2015; Moore and Lockner, 2013). However, the role of the physical state (liquid, vapor and supercritical) of water in the seismic cycle remains unclear, especially in relation to the safe exploitation of deep geothermal reservoirs (Piana Agostinetti et al., 2017; Acosta et al., 2018). Rock friction experiments performed over a broad range of slip displacement (up to meters) and slip velocities (from a few μm/s, or sub-seismic, up to m/s, or seismic) can contribute to the understanding of the seismic cycle under hydrothermal conditions (Rice, 2016; Heaton, 1990; Marone, 1998; Byerlee, 1978; Dieterich, 1979; Tustsumi and Shimamoto, 1997; Blanpied et al., 1995; Steaky et al., 1974; Verberne et al., 2014; den Hartog et al., 2012; Okuda et al., 2023). So far, because of technical challenges, rock friction experiments have been limited to low slip velocities (≤ 100 μm/s) and short slip displacement (≤ 80 mm) (Blanpied et al., 1995; Okamoto et al., 2020; He et al., 2007; Mitchell et al., 2015; An et al., 2020; Niemeijer et al., 2008; Acosta et al., 2018). As a consequence, the frictional properties of fault rocks at seismic deformation conditions in the presence of water under different physical states are still poorly understood.

Here we exploit a new experimental setup to investigate the effect of the physical state of water on fault friction in the seismic cycle. In the case of gabbro, a common oceanic crustal rock, liquid (but at high temperature and pressure) and supercritical water result in a large decrease in fault friction regardless of the imposed fault slip velocity, while in the case of vapor fault friction decreases with slip velocity. Interpretation of the experimental results and analysis of the deformed samples is consistent with the hypothesis that the elastohydrodynamic lubrication and chemical bonding properties of

water at hydrothermal conditions can reduce fault friction during shear.

3.3 Methods

We performed 25 rock friction experiments on cylindrical samples (28 mm external diameter) of gabbro in a rotary shear machine (Ma et al., 2014) equipped with an on-purpose designed hydrothermal vessel (experimental setup, list of experiments and data reproducibility see Figures 3.1-3.3 and Table 3.1). Two gabbro cylinders were sheared for slip displacement up to 3 m at constant sub-seismic to seismic slip velocities (V from 1 μm/s to 0.1 m/s) under "hydrothermal conditions" in the presence of pressurized distilled water in liquid (temperature T = 300°C, pore fluid pressure P_p = 10 MPa), vapor (T = 400°C, P_p = 10 MPa) and supercritical (T = 400°C, P_p = 30 MPa) states.

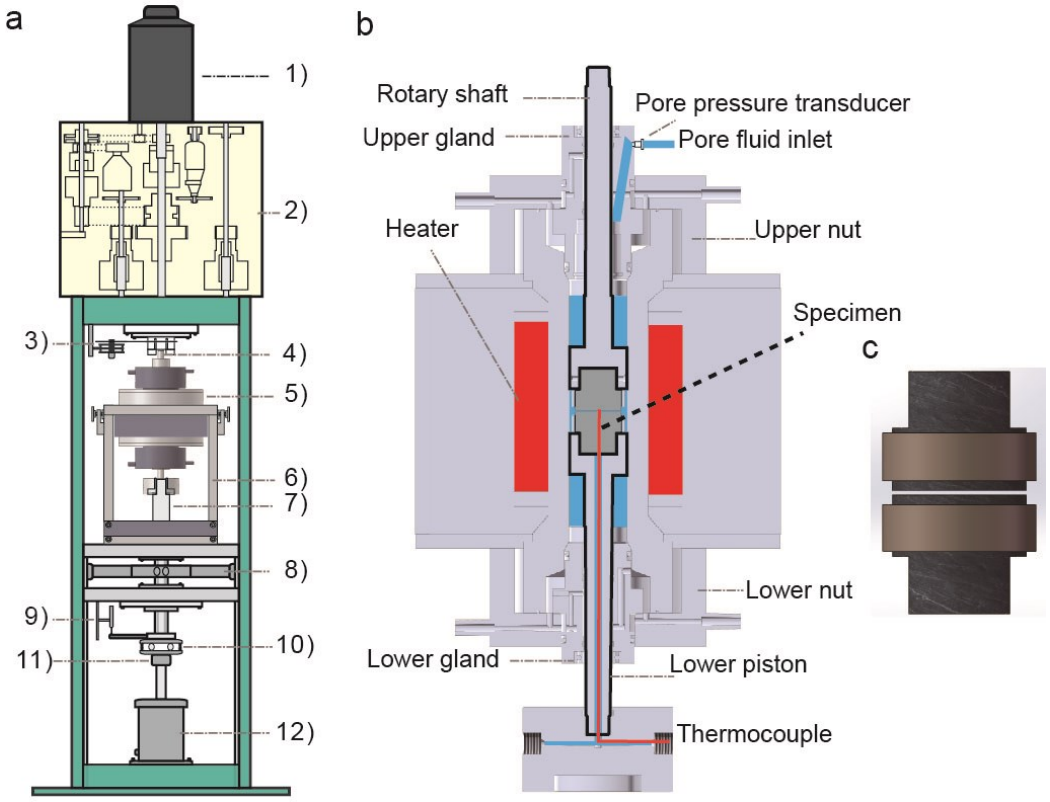

Figure 3.1: Experimental setup. **a.** The Low to High velocity rotary shear apparatus, equipped with a dedicated hydrothermal vessel (modified from Ma et al., 2014). 1) servomotor, 2) gear and belt system, 3) rotary encoder and potentiometer, 4) rotary shaft, 5) hydrothermal pressure vessel, 6) metal frame, 7) axial loading column, 8) cantilever-type torque gauge, 9) liner voltage displacement

transducer, 10) thrust bearing, 11) axial force gauge, 12) air actuator. **b.** The sketch of the hydrothermal vessel with the main parts indicated in the diagram. **c.** Sample assembly: pair of gabbro cylinders jacketed by nickel rings for friction experiments.

The experiments were all performed under drained conditions (ISCO syringe pump maintained the system at a constant pore pressure). An effective normal stress of 10 MPa was imposed to the rock and remained constant throughout each experiment. The temperature was measured with a thermocouple located approximately at the center of the rock cylinder and 1 mm-3 mm away from the slip surface.

The experimental sequence was: (1) pre-grinding process was conducted at 2 cm/s, under 0.5 MPa normal stress to reduce the misalignment of rock surfaces until the oscillation of axial displacement is less than 5 μm; (2) powders produced on the sliding surfaces were removed by using pressurized air and ethanol-wetted papers; (3) the sample assemblage was re-mounted into the machine; (4) the vessel was vacuumed to 2000 Pa; (5) water was injected into the vessel and the pore pressure increased to the target value; (6) the normal stress was loaded to the target value; (7) the vessel was heated with the external furnace and the pore pressure was kept at a constant value (the amplitude of the pressure osculation was less than 0.5%, see Figure 3.2a); (8) once the desired temperature was achieved (this takes 1-2 hours, Stage 1, Figure 3.2a), samples were sheared at a constant velocity spanning from 1 μm/s to 0.1 m/s for a slip displacement up to 3 m (slip displacement, slip velocity and shear stress were determined using the methods outlined in Tsutsumi and Shimamoto, 1997) (Stage 2, Figure 3.2a-b). Normal load, shear torque, fluid pressure and temperature, velocity, revolution, and axial displacement were acquired at a frequency up to 1 kHz. When the target slip displacement was achieved, we stopped the motor and turned off the furnace. The cooling process to room temperature lasted about 2 hours (Stage 3, Figure 3.2a); (9) the samples were recovered from the vessel chamber and prepared for micro-analyses.

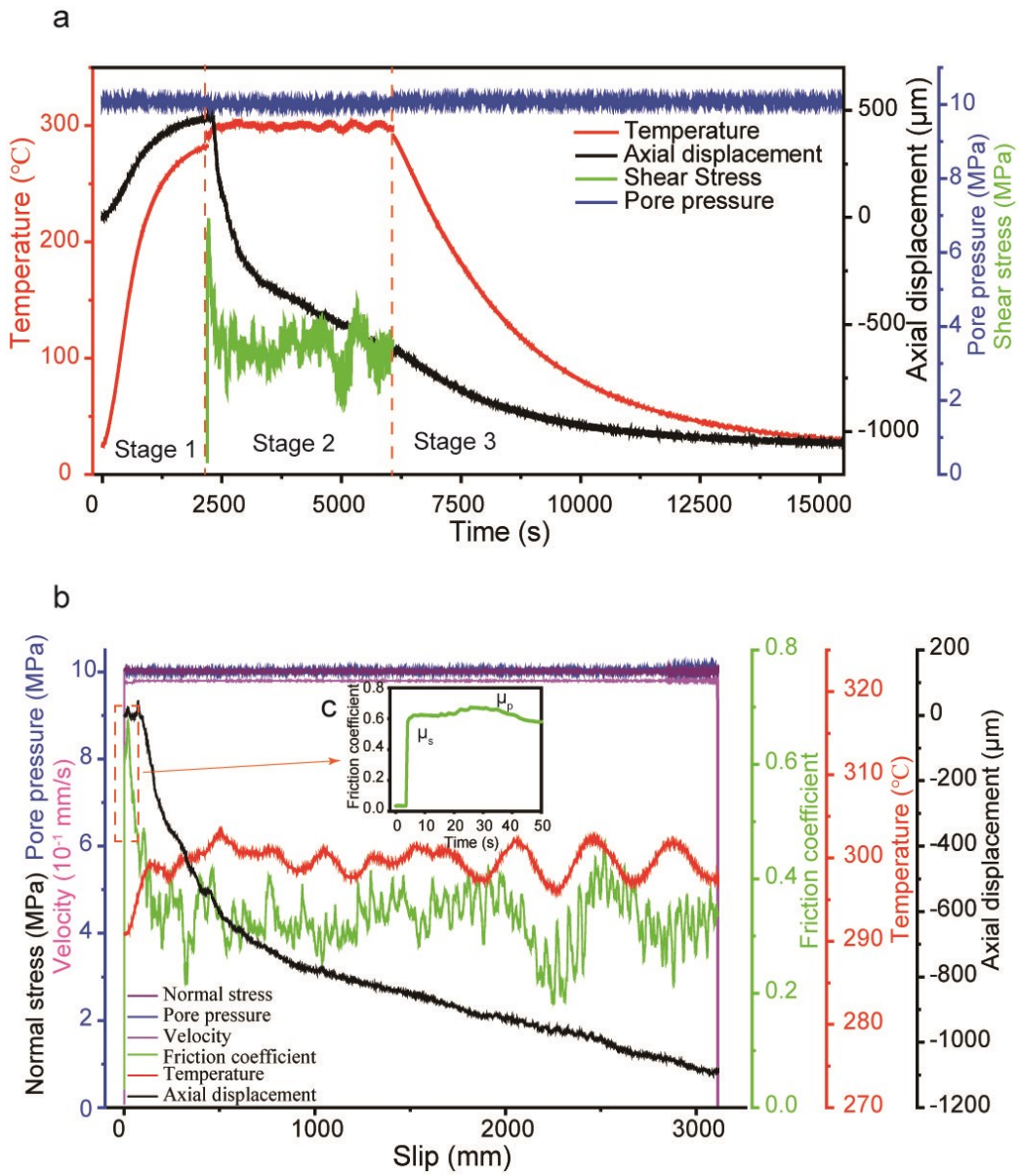

Figure 3.2: Representative experiment (LHV2359) conducted at σ_{eff} = 10 MPa, T = 300°C, P_p = 10MPa, V =1 mm/s (i.e., water in the liquid state) showing the experimental procedure and mechanical data. **a.** Temperature, axial displacement, shear stress and pore pressure versus time for the entire experiment. Stage 1: heating, the temperature increases to the target value. Stage 2: friction test, temperature and pore pressure are kept constant within 2% oscillation. Stage 3: quenching, the temperature cools down to room condition. **b.** Zoom of Stage 2 showing the normal stress, pore pressure, slip velocity, friction coefficient, temperature and axial displacement as a function of slip displacement. During slip, friction coefficient overcomes the static friction (μ_s) and increases to a peak value (μ_p), followed by a decay to the steady-state value (μ_{ss}). Axial displacement shortens faster in the running-in stage and evolves into steady state shortening. **c.** Zoom of the initial part of

the slip with the definition of μ_s and μ_p.

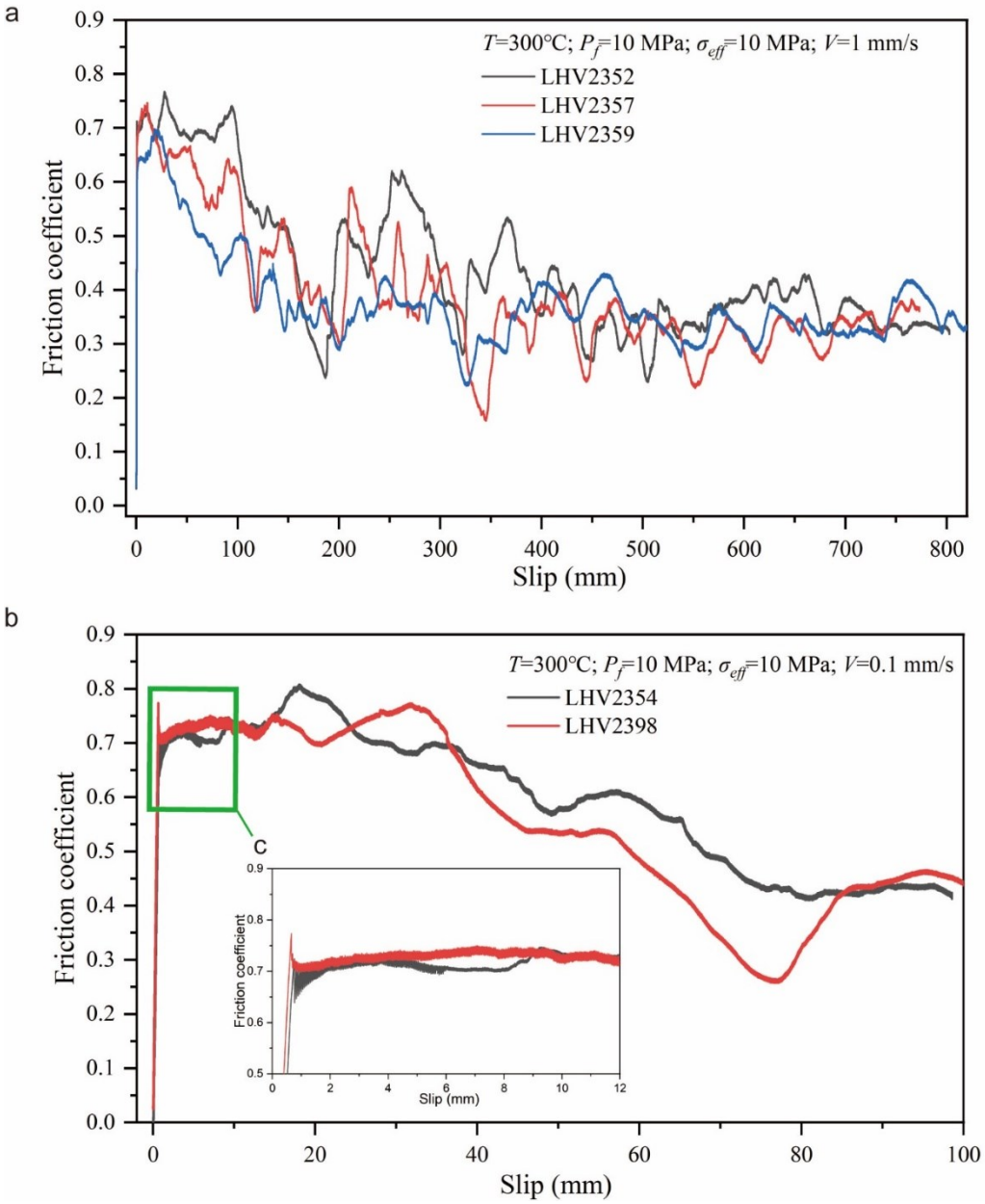

Figure 3.3: Repeated experiments performed under T = 300°C and 10MPa pore pressure, at velocities of 1 mm/s and 0.1 mm/s (water in the liquid state) verifying the data reproducibility. **a.** V = 1mm/s data. For these experiments, the friction coefficient has a similar evolution: μ increases to a peak at the beginning of the slip and then gradually decays to a steady-state value of ~ 0.35 over a displacement of 400 mm. **b.** V = 0.1 mm/s data. After the initial elastic loading, μ remains at 0.7-0.75 for ~ 35 mm displacement, then decreases to a lower value of ~ 0.4 after ca. 90 mm of displacement. **c.** Zoom of the initial slip stage. Stick-slip events occur in the first 6mm of

displacement. Associated stress drops progressively decrease toward stable slip.

Fault strength was presented as friction coefficient μ, the ratio of measured shear stress to effective normal stress. For each experiment, the static friction coefficient (μ_s) or the friction coefficient value when sliding starts on the fault, and peak friction coefficient (μ_p) were obtained from the curve of friction coefficient with time (Figure 3.2). We determined the steady-state friction coefficient (μ_{ss}) as the average value within a displacement window of ~200 mm which covers ~4 rotations of the cylindrical samples to minimize the effects of the frictional fluctuations due to the rotary configuration (see Table 3.1 and Figure 3.2). Correspondingly, the shortening (or dilatancy) rate at steady-state was calculated as the ratio of axial displacement to slip displacement over the same slip displacement range.

The samples were recovered after the experiments for microanalysis with Field Emission Gun Scanning Electron Microscope (FESEM), X-Ray powder diffraction (XRPD), Micro-Raman spectroscopy and non-contact optical profilometer (OP) techniques. Detailed parameters are as follows:

XRPD: Measurements for phase identification were carried out between 3° and 85° 2θ angle, using a 0.017° step size, counting 100 s per virtual step on a spinning sample (1 revolution per second): total scan time is 1 hour and 6 minutes. Samples were prepared using the front-loading procedure onto a Si-crystal sample holder produced to have no diffraction lines (zero-background) suitable for the small amount of material available. Oriented and Ethylene glycol saturated samples were measured between 2.5° and 42° 2θ angle, using a 0.033° step size, counting 200 s per virtual step. Mineralogical species in bulk samples were identified using the search and match procedure implemented in PANalytical High Score Plus v.4.9.0 (Malvern Panalytical Ltd, Malvern, UK).

Micro-Raman: Raman spectra were recorded with an integration time of 0.25/0.5 s and for each spectrum, 30 scans were accumulated. The applied power ranges from 5 to 10

mW.

OP: The measurements were done on 2 x 2 mm^2 areas, using a lateral resolution (step size) of 2 µm and a scan speed of 4 mm/s (2000 Hz). The 3D maps were processed with the software Gwyddion v2.61 (Czech Metrology Institute). The final calculation (selected 1 x 1 mm^2) of the texture parameters, including those from the standard EN ISO 25178-2, was performed by a 3D analysis of the height maps including the high-pass roughness component and the low-pass waviness component together (that is, no wavelength cut-off was set).

FESEM: Images have been acquired with an in-beam mid-angle backscattered detector using an accelerating voltage of 5 KeV, current of 300 pA and a working displacement of 3 or 4 mm.

Table 3.1: List of experiments (Summary of experimental conditions and results) T: temperature, σ_{eff}: effective normal stress, P_p: pore pressure, L: liquid, V: Vapor, SC: Supercritical, δ: slip displacement μ_s: static friction, μ_p: peak friction, μ_{ss}: steady-state friction, Displacement (d) window was chosen to calculate the μ_{ss} and shortening rate, ΔT: estimated increase of temperature in the slipping zone.

Experiment (LHV)	***T*** **(°C)**	σ_{eff} **(MPa)**	P_p **(MPa)**	**Phase of water**	**Velocity (mm/s)**	***d*** **(mm)**	***d*** **window (mm)**	μ_s	μ_p	μ_{ss}	**shortening rate (mm/mm = mm shortening vs. mm of slip displacement)**	ΔT **(°C)**
2379	25	10	10	L	1	3000	2000-2200	0.599	0.721	0.674±0.034	0.033	
2374	300	10	10	L	0.001	380	240-300	0.864	0.864	0.511±0.039	/	
2354	300	10	10	L	0.01	100	80-200	0.742	0.824	0.449±0.012	/	
2398	300	10	10	L	0.01	300	240-300	0.772	0.772	0.261±0.076	0.118	0.04
2349	300	10	10	L	0.1	180	80-180	0.61	0.622	0.370±0.018	0.551	
2356	300	10	10	L	0.1	670	80-200	0.65	0.683	0.442±0.060	0.89	0.42

2400	300	10	10	L	0.1	1000	600-800	0.715	0.797	0.280±0.014	0.371	0.3
2352	300	10	10	L	1	800	600-800	0.71	0.766	0.362±0.029	0.925	
2357	300	10	10	L	1	772	600-772	0.73	0.745	0.328±0.022	0.595	
2359	300	10	10	L	1	3100	2000-2200	0.642	0.695	0.319±0.036	0.174	3.2
2358	300	10	10	L	10	3900	2000-2200	0.621	0.671	0.414±0.016	0.25	104
2360	300	10	10	L	100	3200	2000-2200	0.572	0.572	0.268±0.012	0.014	
2361	300	10	10	L	100	3200	2000-2200	0.574	0.58	0.263±0.027	0.091	842
2391	400	10	10	V	0.01	300	80-200	0.69	0.793	0.695±0.026	0.107	0.07
2388	400	10	10	V	0.1	1000	600-800	0.87	0.915	0.718±0.031	0.065	0.8
2362	400	10	10	V	1	3000	2000-2200	0.793	0.839	0.717±0.010	0.017	6.02
2395	400	10	10	V	10	3000	2000-2200	0.51	0.66	0.469±0.024	0.064	54.4
2363	400	10	10	V	100	3300	2000-2200	0.577	0.637	0.262±0.010	0.025	806
2365	400	10	30	SC	0.01	150	80-150	0.381	0.529	0.400±0.013	/	
2380	400	10	30	SC	0.01	300	80-200	0.514	0.558	0.509±0.027	0.01	0.06
2390	400	10	30	SC	0.1	1000	600-800	0.563	0.588	0.281±0.020	0.421	0.31
2367	400	10	30	SC	1	3000	2000-2200	0.531	0.717	0.279±0.038	0.107	2.1
2373	400	10	30	SC	10	3500	2000-2200	0.499	0.658	0.260±0.050	0.088	35.6
2383	400	10	30	SC	10	3000	2000-2200	0.565	0.565	0.296±0.022	0.117	16
2369	400	10	30	SC	100	3000	2000-2200	0.575	0.575	0.212±0.018	0.037	789

3.4 Results

3.4.1 Mechanical data

In the experiments, the friction coefficient of gabbro evolved with slip displacement, slip velocity and physical state of water as follows (Figure 3.4):

W*ater in liquid state.* Regardless of the imposed slip velocity, the friction coefficient of gabbro increased over a slip displacement of 10-30 mm from an initial static friction

coefficient μ_s = 0.61–0.80 to the peak one μ_p = 0.75±0.10, and then decayed over a slip displacement of ~200–500 mm to the steady-state μ_{ss} = 0.20–0.35 (Figure 3.4a). The μ_s, μ_p and μ_{ss} values, though with some scatter, decreased with increasing slip velocity (Figure 3.4b).

Water in supercritical state. Regardless of the imposed slip velocity and similar to experiments performed with water in liquid state, the friction coefficient of gabbro increased over a slip displacement of 10–280 mm from μ_s = 0.5–0.58 to μ_p = 0.6±0.10, and then decayed over a slip displacement of ~ 300–500 mm to μ_{ss} = 0.2–0.3 (Figure 3.4c). The μ_s, μ_p and μ_{ss} values were almost independent of slip velocity (Figure 3.4d).

Water in vapor state. Differently from the experiments with water in liquid and supercritical states, the friction behavior of gabbro was velocity-dependent (Figure 3.4e). In particular, for 0.01 ≤ V ≤ 1 mm/s, the friction coefficient remained high: from μ_s = 0.75±0.05 it increased to μ_p = 0.81–0.92 and then decreased to μ_{ss} = 0.67–0.72 (Figure 3.4f). Instead, for V = 10 mm/s, the friction increased from μ_s = 0.51 to μ_p = 0.66 and then first decayed to 0.47±0.05 over a slip displacement of 2200 mm and then further decreased to 0.2 till the end of slip. At V = 100 mm/s, the friction coefficient decayed from μ_s = 0.57and μ_p = 0.64 to μ_{ss} = 0.26 after ca. 250 mm of slip. The μ_s, μ_p and μ_{ss} values evolved from velocity-neutral to velocity-weakening with increasing slip velocity (Figure 3.4f).

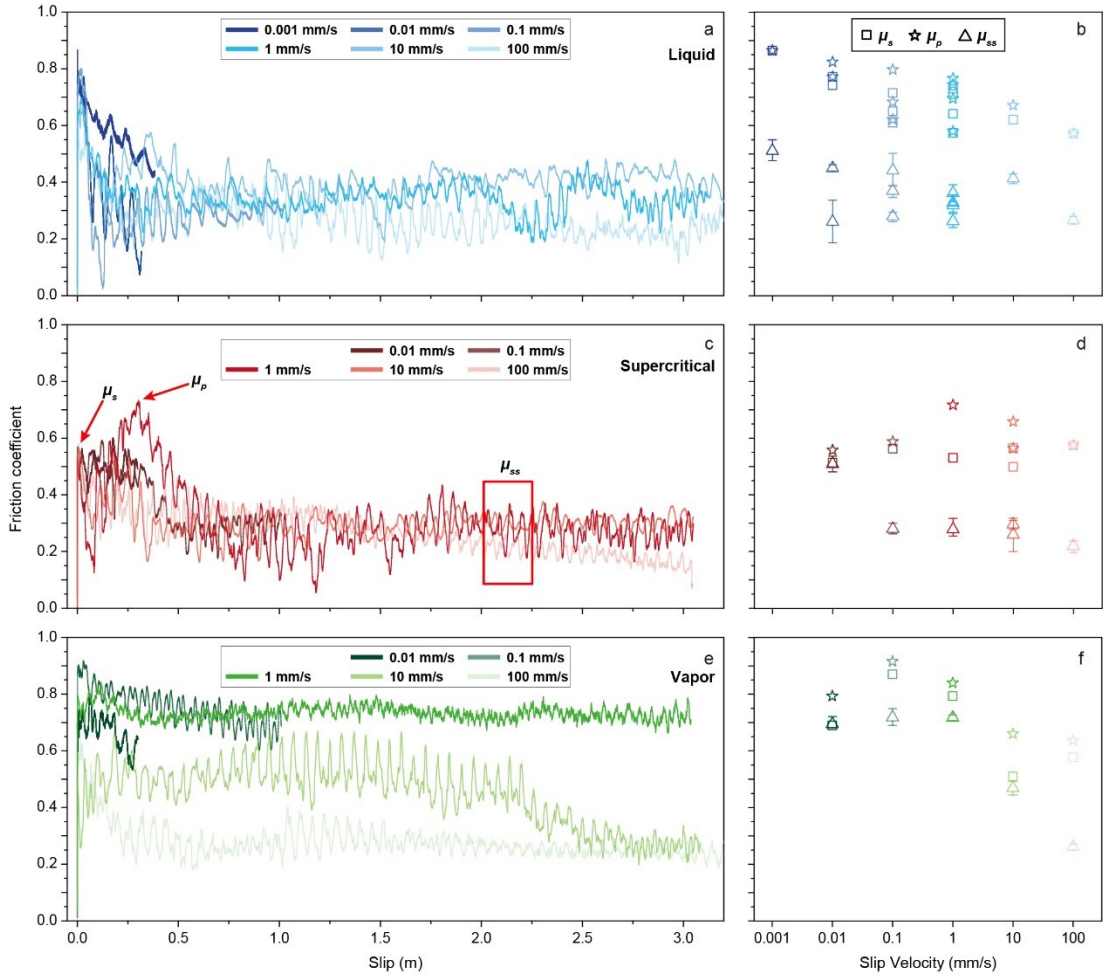

Figure 3.4: Friction coefficient of gabbro rocks under hydrothermal conditions. The gabbro cylinders were sheared up to 3 m of slip displacement under a constant effective normal stress of 10 MPa. Left side graphs: evolution of friction coefficient with slip displacement. Slip velocities ranged from 0.001 mm/s to 100 mm/s (colors coded). Right side graphs: static (μ_s, open squares), peak (μ_p open pentagrams) and steady-state (μ_{ss} open triangles) friction coefficients with slip velocity. **a, b.** Water in liquid state (T = 300°C, P_p = 10 MPa). **c, d.** Water in supercritical state (T = 400°C, P_p = 30 MPa). **e, f.** Water in vapor state (T = 400°C, P_p = 10 MPa).

The mechanical data show that the physical state of water impacts the friction properties of the experimental fault to a larger extent than previously thought. For instance, in experiments performed with tri-axial machines (i.e., slip displacement < 1 mm, slip velocity < 0.1 μm/s) on quartz gouges , the decrease of friction coefficient at the water transition from the liquid to the vapor state was limited to ~0.05 (Mizoguchi et al.,

2007). Instead, we measured an increase of friction coefficient at this transition for larger slip displacement and velocities (Figure 3.4b, f).

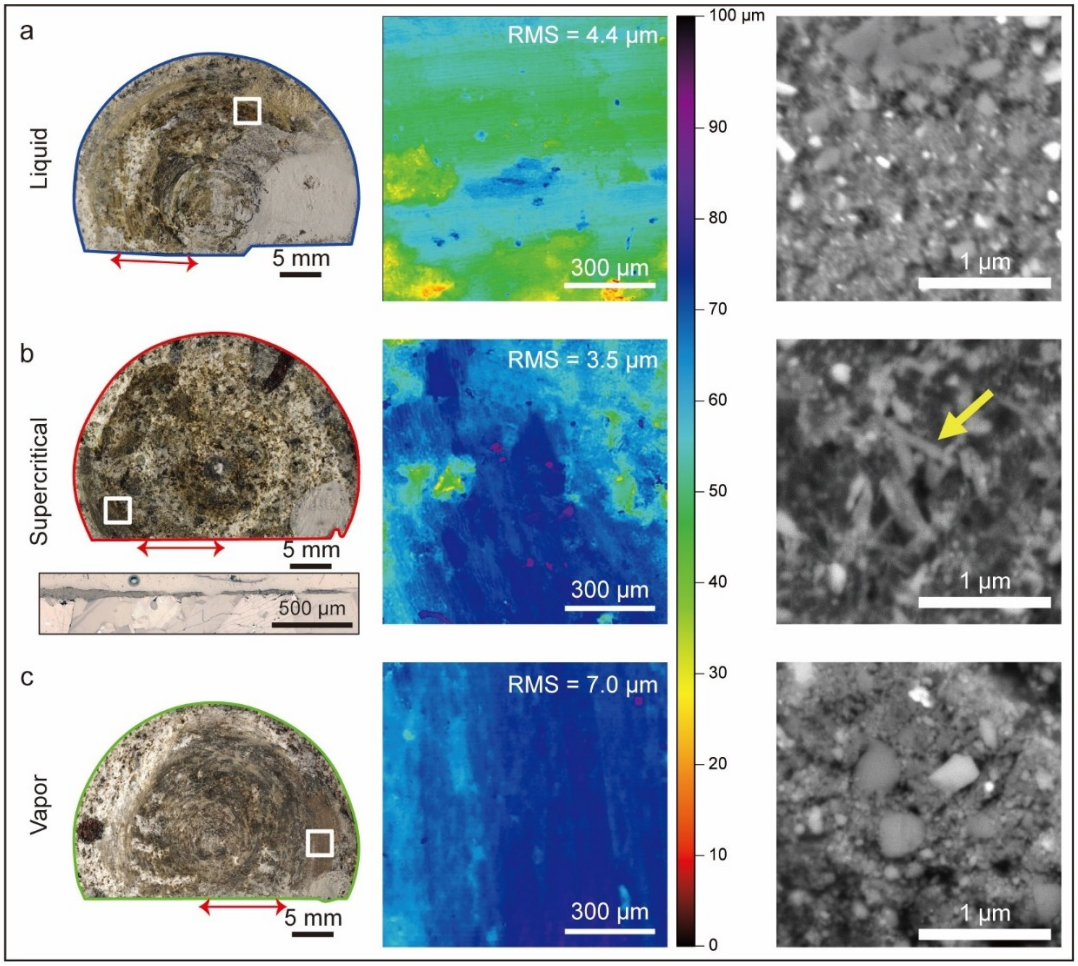

Figure 3.5: Microstructural and mineralogical analysis on post-experimental samples. The gabbro cylinders were recovered after shearing under hydrothermal conditions. **a, b, c.** Data for tests performed at V=10 µm/s with water in liquid (LHV2398), supercritical (LHV2380) and vapor (LHV 2391) states. The left panel shows photographs of the slip interface. The middle panel shows the digital elevation model of slip surface derived from white light interferometry over area of 1 x 1 mm^2 (square in the left panel). The right panel shows scanning electron microscope images perpendicular to the slip zone along the profile marked by red arrow in the left panel. In b, a panoramic view of the slip zone is shown in the inset in left panel, and the newly-formed clay-like minerals are indicated by yellow arrow (LHV2380).

3.4.2 Microanalysis of deformed samples

To identity the possible deformation mechanisms responsible for these large measured differences in the frictional behavior of gabbro rocks, the samples were recovered for mineralogical and microstructural investigations. Unfortunately, part of the non-cohesive powder produced during shearing in the slip zone might have been flushed away during fluid ejection and sample unloading. However, regardless of the imposed slip velocity, the slip surfaces of the faults that were whitish in color before the experiments acquired a dark green color in the experiments with liquid and supercritical water and medium green color in the experiments with water in vapor state (Figure 3.5a-c). After the experiments, the slip surfaces were ultra-polished and lineated (i.e., *striae* parallel to the slip vector) and, based on OP measurements, had a micro-roughness with a root mean square (RMS) of ~3.5-7 μm (for starting surface see Figure 3.6) (Figure 3.5a-c). The slip zones beneath the slip surfaces were <30 μm thick and made of ultrafine powders with grain size down to few nm (Figure 3.5a-c). In particular, the powders from the experiments conducted with water in supercritical state included ultra-fine (~200 nm long and ~30 nm thick) newly formed clay-like minerals, which were not found in the other experiments (Figure 3.5a-c). However, their size was too small for FESEM-elemental analysis. XRPD analysis performed directly on the slip surfaces and on the powders (~10 mg, after ethylene glycol treatment) (Figure 3.7) recovered from the slip zone revealed the presence of a broad peak at 8° in the spectra of the gabbro sheared with water in the liquid or supercritical state. This broad peak, typical of smectite and chlorite (Brindley & Brown, 1980), was absent in the XRD spectra of the surfaces of the starting (not sheared) gabbro and of the slip surfaces recovered after the experiments with water in the vapor state. Based on XRD semi-quantitative analysis, the abundance is estimated to be less than 5 wt.%. Similarly, a peak at a wavenumber of 1595–1600 cm^{-1} was present only in the micro-Raman spectra of the ultra-polished slip surfaces recovered from the experiments performed with water in the liquid and supercritical states (Figure 3.8). This wavenumber corresponds to the

H–O–H bending vibrational mode of H_2O (Yu et al., 2020) and is possibly associated with the water absorbed in the slip surfaces or immediately beneath (the micro-Raman exciting signal can penetrate < 1 μm). In the micro-Raman spectra map (600 x 600 μm^2) of the slip surfaces, the signal of the H–O–H bending overlaps with the location of the *striae* (Figure 3.9). This implies that the formation of this particular H-O-H bond is associated with the development of high-strain zones.

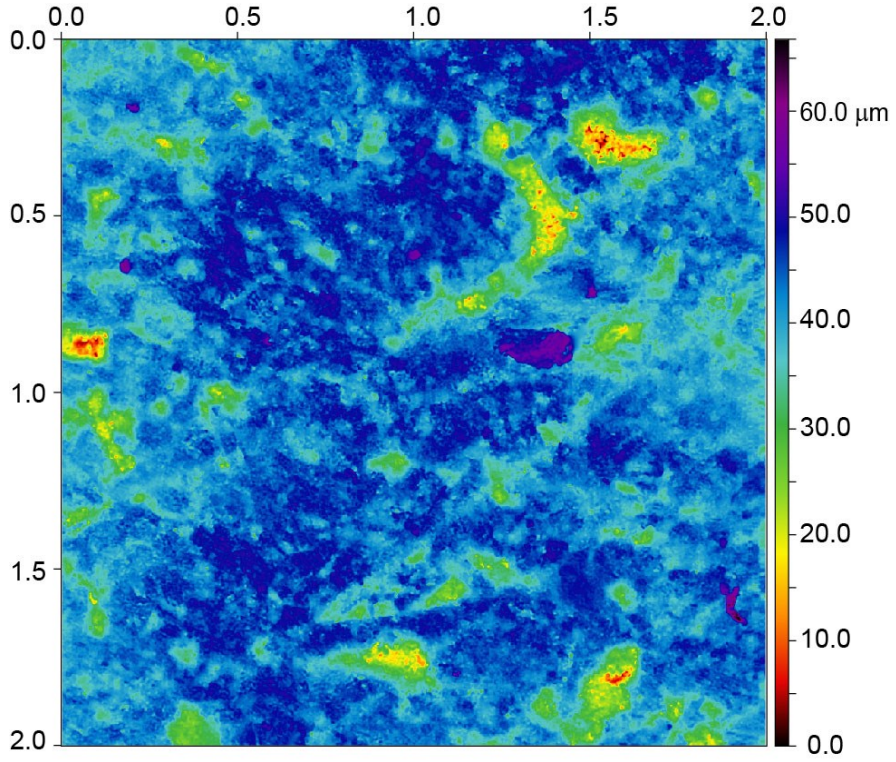

Figure 3.6: Roughness of the starting surface measured by WLI. The root mean square (RMS) value is 5.7 μm.

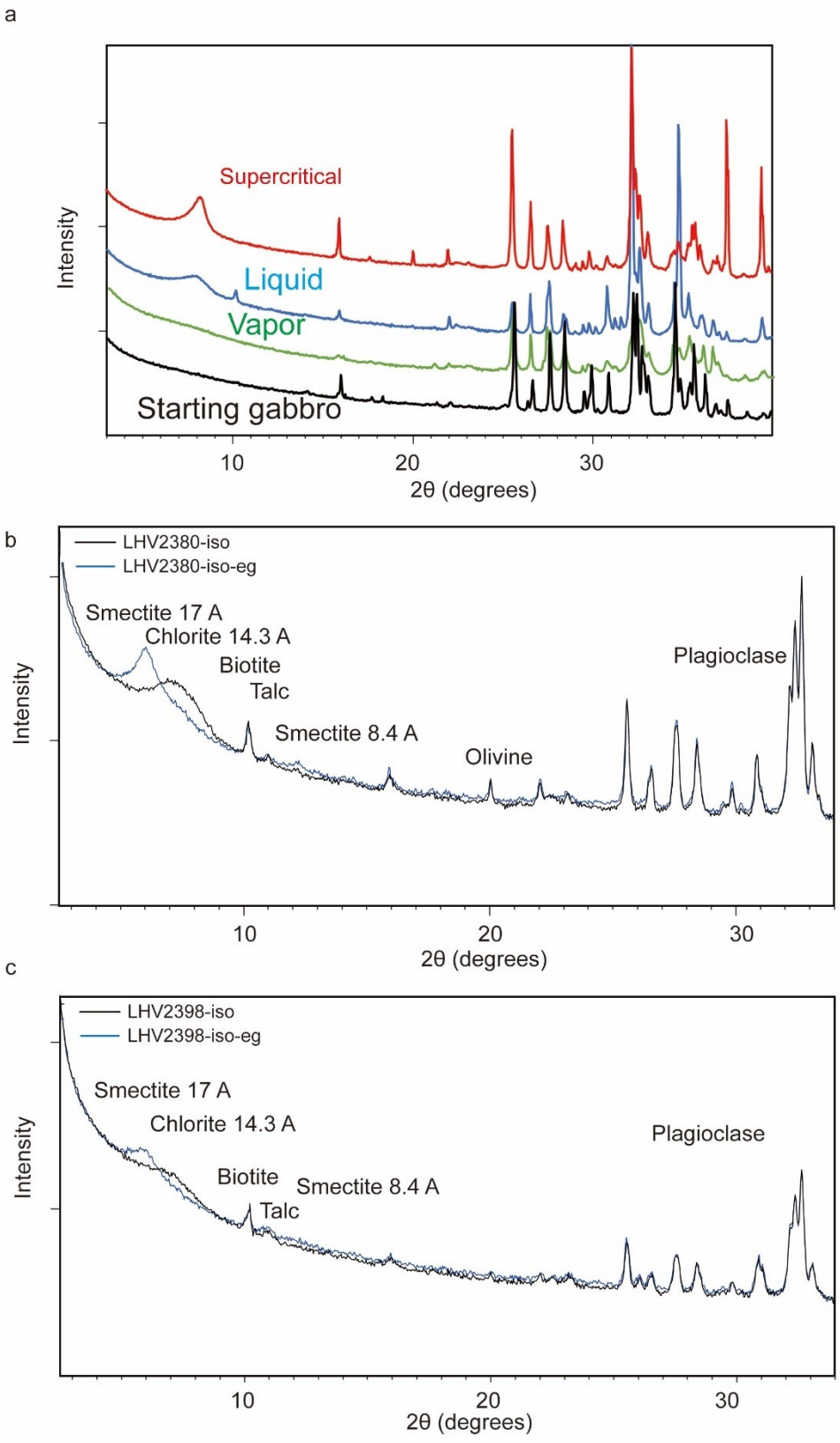

Figure 3.7: X-ray powder diffraction data. **a.** The peak at ~8° suggests the formation of clay minerals and phyllosilicates in experiments LHV2398 (liquid state water) and LHV2380 (supercritical state water). XRD spectra after iso-oriented and ethylene glycol treatment of 10 mg

of powders recovered from the slip zones of experiments LHV2380 and LHV2398. The spectra show that a mixture of smectite and chlorite is present in both the slip zones. **b.** Experiment LHV2380, water in supercritical state. **c.** Experiment LHV2398, water in liquid state.

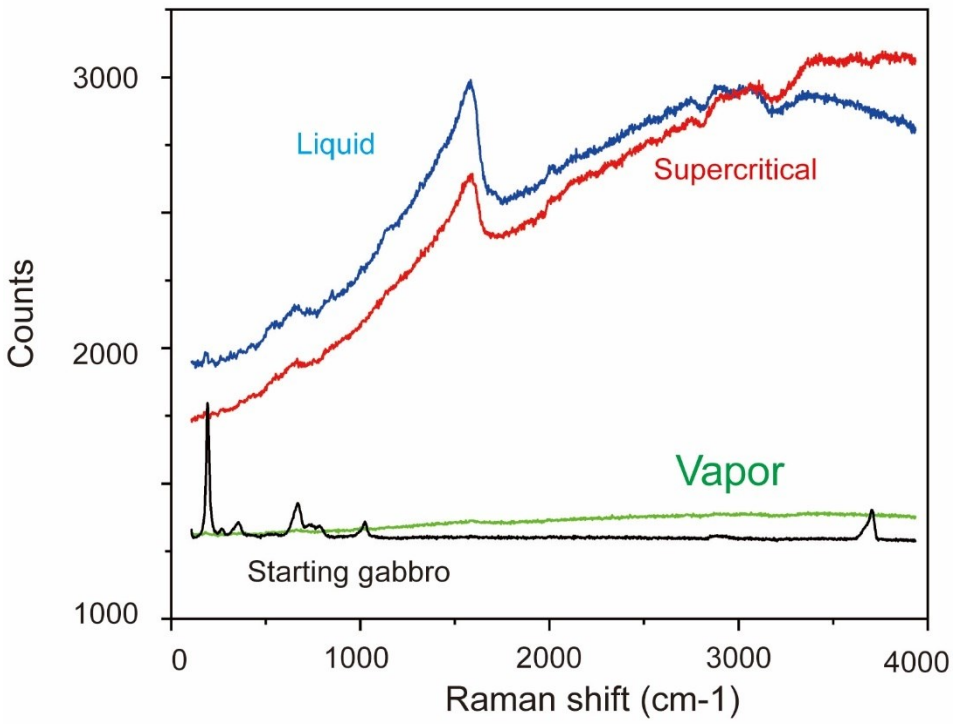

Figure 3.8: Micro-Raman spectra data for experiments performed at V =1 mm/s with water in liquid (LHV2359), supercritical (LHV2367) and vapor (LHV 2362) states. A broad peak at a wavenumber of ~1600 cm^{-1} (corresponding to H–O–H bending vibration mode) is only present in experiments with liquid and supercritical water.

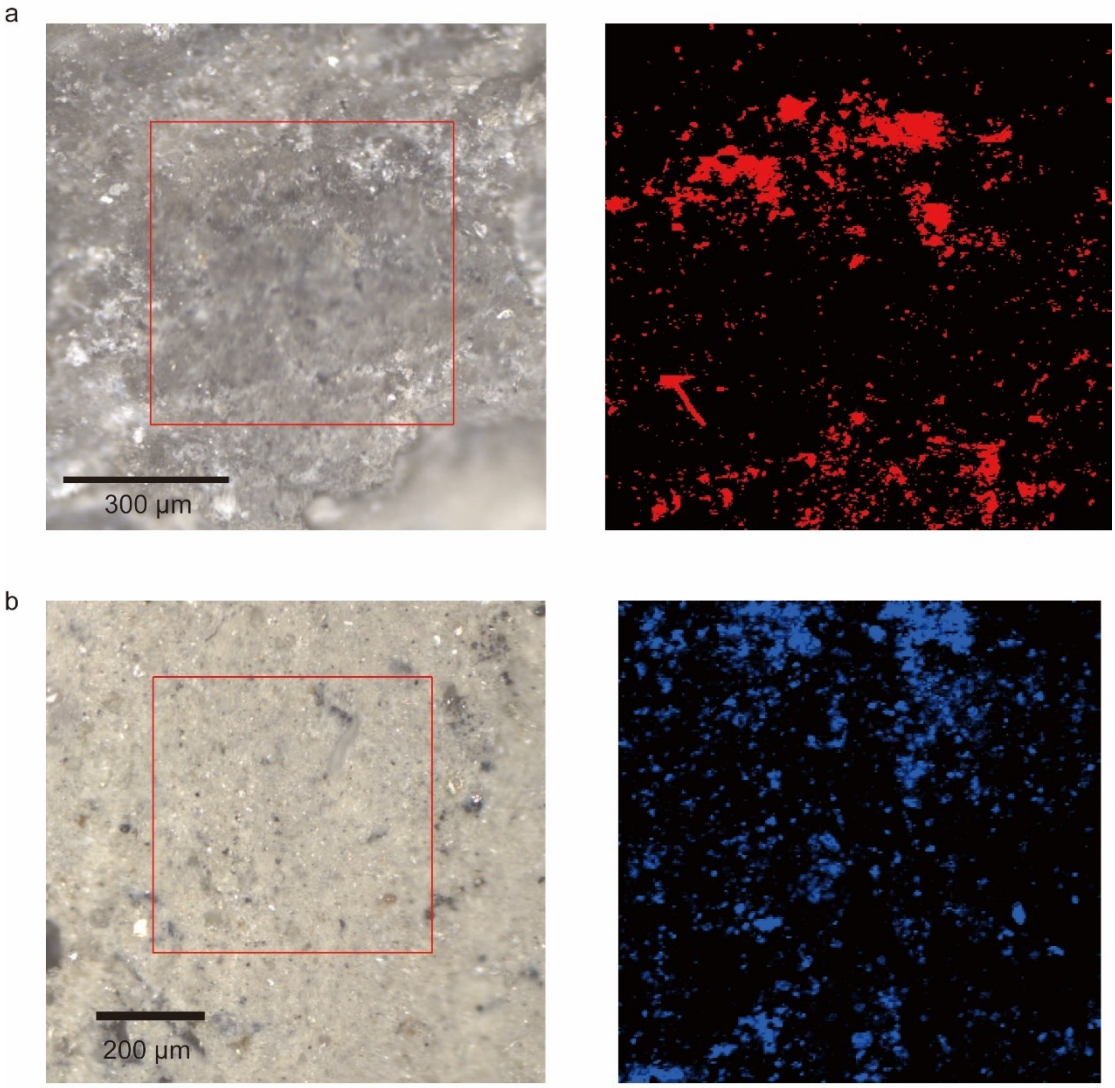

Figure 3.9: Micro-Raman map (scanned area is marked by red square) showing the spatial distribution of H–O–H bending bonds in the slip zone. Left: the scanned areas of the Raman map are marked with a color square. The Raman map (right) show that the H-O-H bending bonds approximatively overlap the striations of the slip surface. **a.** experiment LHV2367 (supercritical water); **b.** experiment LHV2359 (liquid water).

In conclusion, the microstructural and microanalytical analysis confirm the formation of an ultra-polished slip surface topping a few tens of micrometer (Figure 3.5b) thick slip zone in all the experiments. However, only in the experiments performed with liquid or supercritical water (i.e., when, regardless of the imposed slip velocities, the lowest values of the friction coefficient were measured) the slip zone is enriched in H–

O–H bonds water and includes newly-formed water-bearing minerals.

3.5 Discussion

In this study, we imposed with the external furnace and pressuring fluid pump, temperature and pressure conditions to obtain a constant physical state of water (liquid, supercritical and vapor) inside the hydrothermal vessel during the experiments. However, frictional heating can lead to an increase in the temperature in the slipping zone which may determine the transition of the physical state of water. Numerical modelling shows that the temperature rise in the slipping zone required for the transition of water from liquid to vapor state is achieved in experiments performed at $V \geq 10$ mm/s (Figure 3.10). This result is supported by the observation that μ_{ss} is similar between the experiments in liquid and vapor water at $V > 10$ mm/s (Figure 3.4b and 3.4f). Whereas in the experiments performed at $V \leq 1$ mm/s, temperature increase in the slipping zone is negligible and the physical state of water should not change.

Thousands of experiments performed in the last 25 years aimed at approaching or reproducing seismic deformation conditions (e.g., $V \geq 0.1$ m/s) measured low values of μ_{ss} independently of rock composition and of the pressure of water (Di Toro et al., 2011; 2021). This so-called dynamic weakening is due to the activation of several temperature and possibly grain-size dependent weakening mechanisms (Wibberley & Shimamoto, 2005; Pozzi et al., 2021; Nielsen et al., 2021; Tullis, 2015). However, these previous observations are at odds with the experimental data presented in Figure 3.4. For instance, in previous experiments performed at room temperature on gabbro in the presence of pressurized liquid water, μ_{ss} decreases only for $V \geq 10$ mm/s (Togo et al., 2015; Violay et al., 2014), not for $V \geq 0.01$ mm/s when pressurized (hot) water is in liquid and supercritical states (Figure 3.4a-b).

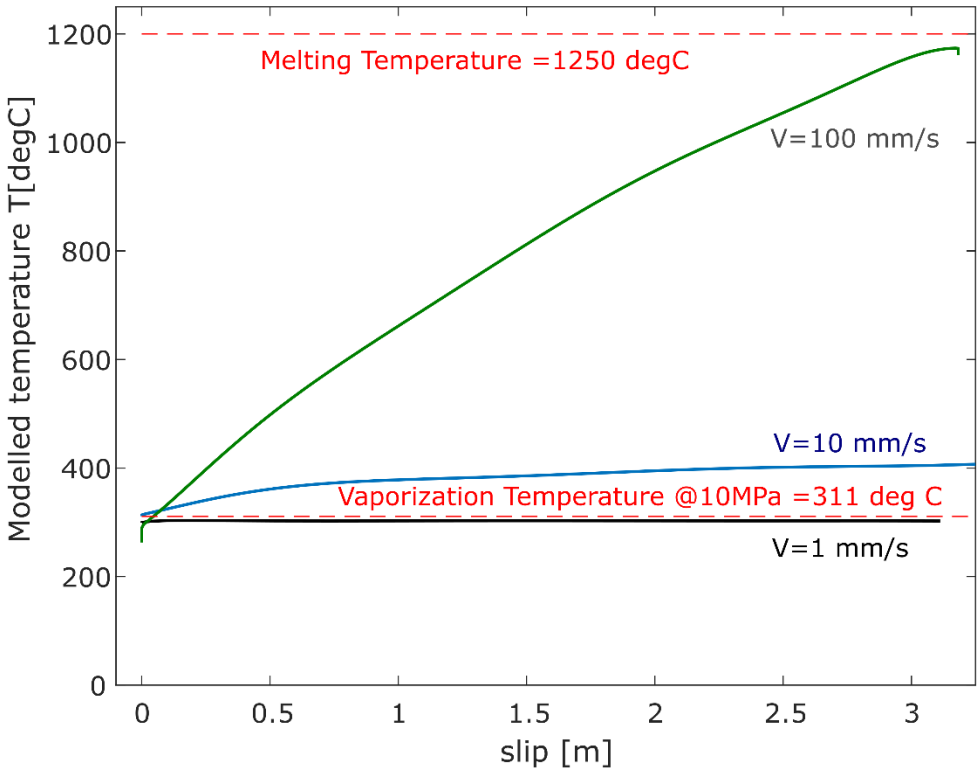

Figure 3.10: Numerical model results of the evolution of temperature in the slipping zone with slip displacement. The liquid-vapor transition temperature of water at P_p = 10 MPa is 311°C and is indicated by red in color dashed line. The modelled maximum temperatures for the experiment (LHV2359) preformed at V = 1 mm/s, for the experiment (LHV2358) at V = 10 mm/s, and for the experiment (LHV2361) at V = 100 mm/s reach ~30, 504 and 1142°C, respectively.

Alternatively, low values of μ_{ss} were measured in experiments performed on particular clays and phyllosilicates (e.g., saponite, Na-smectites, talc) gouges sheared at sub-seismic slip velocities ($V \leq$ 10 mm/s) (Sone et al., 2012). Also mixtures of these particular clays/phyllosilicates with "hard" minerals (e.g., quartz, calcite, dolomite) may result in a bulk low friction coefficient if the "weak" minerals form a continuous layer (Collettini et al., 2009). As a consequence, the low friction coefficient measured at sub-seismic slip rates in the experiments performed with water in liquid or supercritical state could be related to the formation of minerals with low frictional strength. Their formation, due to fluid-rock interaction, would be boosted by the

increased mineral reactivity due to tribo-chemical effects in the slip zone because of grain size reduction and the high temperature of the fluid. In fact, newly-formed clay-like minerals are present in the recovered slip zones (Figure 3.5a-c). Although it cannot be ruled out that clay-rich parts of the slip zones were lost during sample recovery, their abundance is very low (< 5 wt. %), and clays are not arranged to form a continuous layer that could weaken the fault (Collettini et al., 2009) (Figure 3.6).

Alternatively, rather than to the formation of new minerals phases, the measured low μ_{ss} could be related to the chemical effects of water in the slipping zone. The micro-Raman spectra of the slip zones recovered from the experiments performed with water in liquid and supercritical state have a peak at ~1600 cm^{-2} (Figure 3.7) that indicates a vibrational mode of absorbed water typical of H–O–H bending. This signal is detected only in the slip zones associated with low measured friction, suggesting that the presence of water and this particular type of chemical bonding of absorbed water contributes to fault lubrication. Therefore, we propose that the hydrogen-bonding between silanol (Si–O–H) on the surfaces of newly formed grains may contribute to the weakening of the fault. In fact, the peak (~1600 cm^{-2}) measured in the low frequency range (1580-1650 cm^{-2}) of the H–O–H bending mode corresponds to weaker intermolecular O···H hydrogen–bonding (Seki et al., 2020), which would contribute to the decrease of the fault strength. However, further studies are required to quantify the role of chemical bonds of absorbed water in fault slip zones.

A possible "physical" weakening mechanism could be the elastohydrodynamic (EHD)-lubrication (Cornelio et al., 2019; Brodsky & Kanamori, 2001). The a-dimensional parameter

$$S = \frac{6\eta V L}{H^2 \sigma_{\mathrm{n}}^{\mathrm{eff}}} \qquad (3\text{-}1)$$

(with η the fluid viscosity and H the height of the asperities and L the characteristic length for pressure changes) describes the transition, for $S \geq 0.001$, from boundary (high μ_{ss}) to mixed (intermediate μ_{ss}) and, for $S \geq 1$, to hydrodynamic lubrication (low μ_{ss}).

By re-arranging Eq. 1 for $\eta = f(H^2)$, we estimate the range of η and H values required to have $S \geq 0.001$ at $V = 10$ mm/s (graphic solution in Figure 3.11a). Assuming that the measured RMS corresponds to H (Cornelio et al., 2019) (3.5 μm < H < 7 μm, Figure 3.5a-c), the required η for $S \geq 0.001$ spans from 2.3 x 10^{-3} to 9.2 x 10^{-3} Pa·s (Figure 3.11a). These estimated viscosities are in the range of those attained by a mixture or suspension of rock powders with water in liquid (η_{H2O} = 9.0 x 10^{-5} Pa·s at T = 300 °C, P_p = 10 MPa) and supercritical (η_{H2O} = 4.0 x 10^{-5} Pa·s at T = 400 °C, P_p = 30 MPa) states. In fact, the viscosity of the mixture increases significantly as the volume fraction of powder increases (Brodsky & Kanamori, 2001; Brandt & Coletti, 2022), facilitating the activation of mixed and EHD lubrication. Indeed, the highest shortening rates are measured in the experiments performed with liquid and supercritical water (Figure 3.12), implying that the fluid expelled from the slipping zone is mixed with rock debris. This is in agreement with the presence of water in the recovered slip zones (Figure 3.7). Instead, the rock powder is hardly dissolved or suspended in vapor (Morey, 1957), therefore the viscosity of water vapor is barely affected by powders and remains very low. Consequently, the slip velocity for EHD mixed lubrication activation ($S \geq 0.001$) is estimated to be 9.2 mm/s (Cornelio & Violay, 2020) (Figure 3.11b), which agrees with the low μ_{ss} measured at V=10 mm/s (Figure 3.4f).

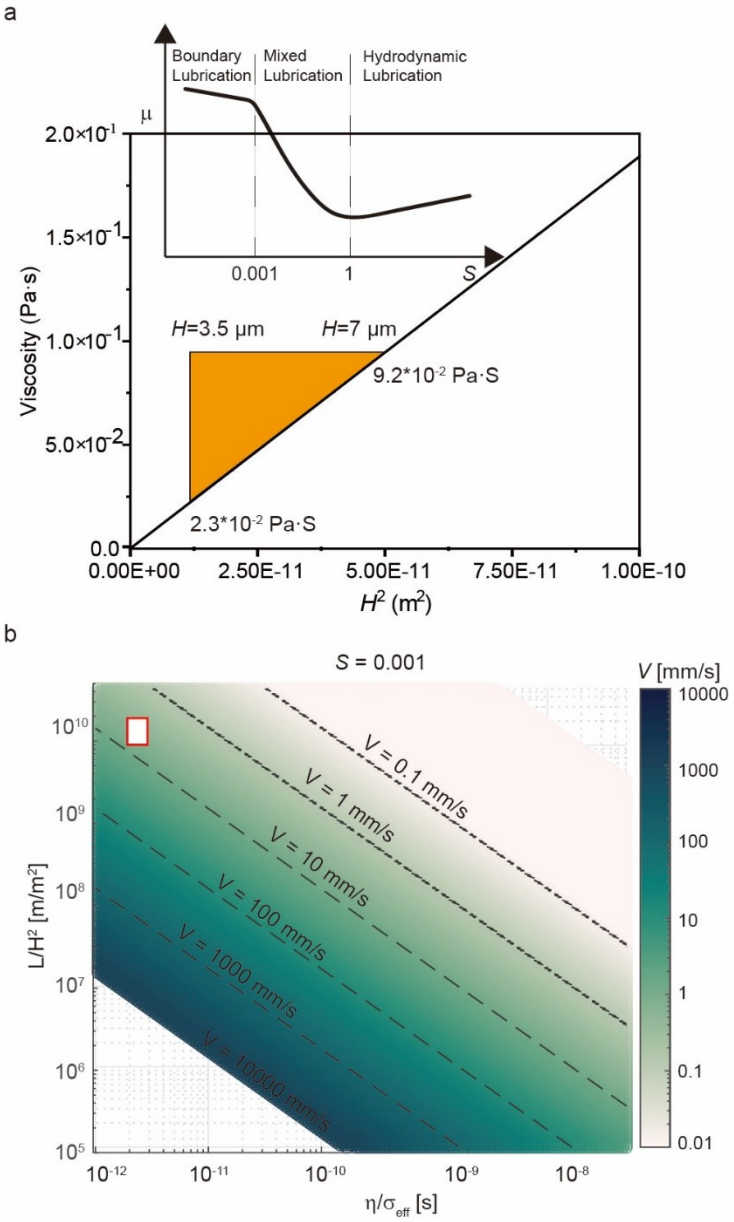

Figure 3.11: Estimate of the conditions for the activation of the EHD mixed lubrication. **a.** Viscosity η vs. H^2. Inset shows the friction coefficient vs. Sommerfeld number (S). By re-arranging equation 1 for $\eta = f(H^2)$, the range of η for having $S \geq 0.001$ according to the measured H values (Figure 3.5) spans from 2.3 x 10^{-3} to 9.2 x 10^{-3} Pa·s. **b.** The multiaxis plot of the Sommerfeld number for $S \geq 0.001$. The slip velocity for the activation of EHD mixed lubrication in the presence of water in vapor state is roughly 10 mm/s (red in color box). This slip velocity is consistent with the one at which a drastic reduction in the friction coefficient is observed in experiments conducted in the presence of water in vapor state (Figure 3.4f).

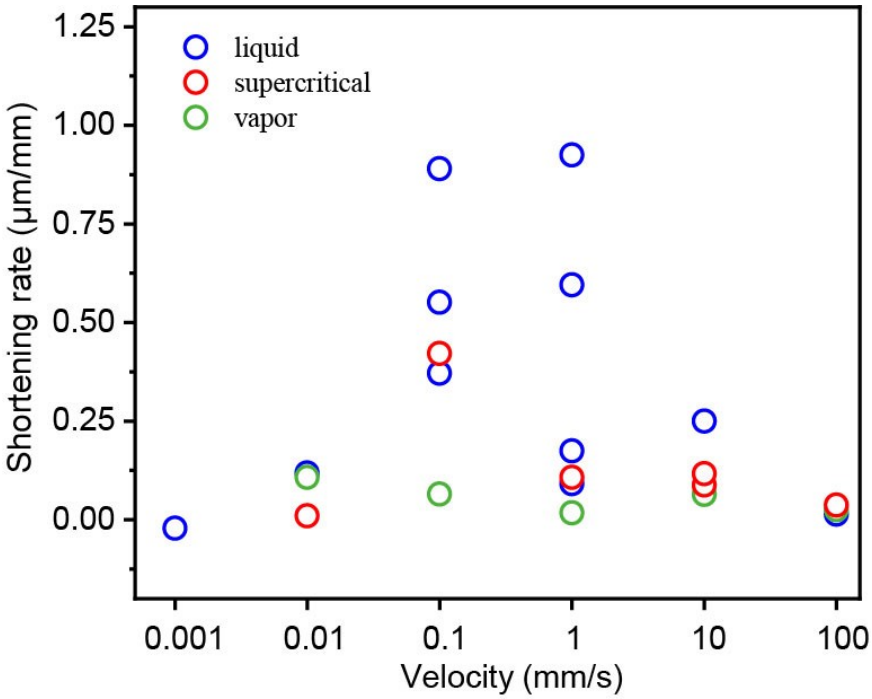

Figure 3.12: Sample shortening rate vs. slip velocity under hydrothermal conditions. In experiments with gabbro samples, at the same effective stresses and regardless of the imposed slip velocity, the measured wear rates are lower in the presence of water in the vapor state than in the presence of water in the liquid and supercritical state.

In this study we show that the friction of gabbro rocks is controlled by the physical state of water. Experimental and microanalytical investigations suggest that fault weakening at low slip velocities is probably related to the physical (EHD lubrication) and chemical (e.g., H–O–H bending) role of water together with the formation of newly-formed minerals (Figure 3.13). The physical state of water on fault friction has significant implications for earthquake physics such as rupture nucleation, propagation and arrest. For instance, slip zone dilatancy can cause drops in pore pressure and the transition of water from liquid to vapor state and, as a result, an abrupt increase in fault friction that may arrest or delay the earthquake nucleation stage (see high-temperature slip transients in subduction zones: Shelly et al., 2006). Our work emphasizes that such a fault restrengthening process is not only caused by increased effective normal stress as previously recognized, but also promoted by the increase in intrinsic friction. Similarly, during rupture propagation, slip zone dilatancy along extensional jogs and step-overs

may result in instantaneous transitions from liquid to vapor which may increase fault strength (Brantut, 2020; Weatherley & Henley, 2013). Our results provide new insights into the processes responsible for stabilizing the fault slip and arresting the rupture propagation in natural and human-induced earthquakes.

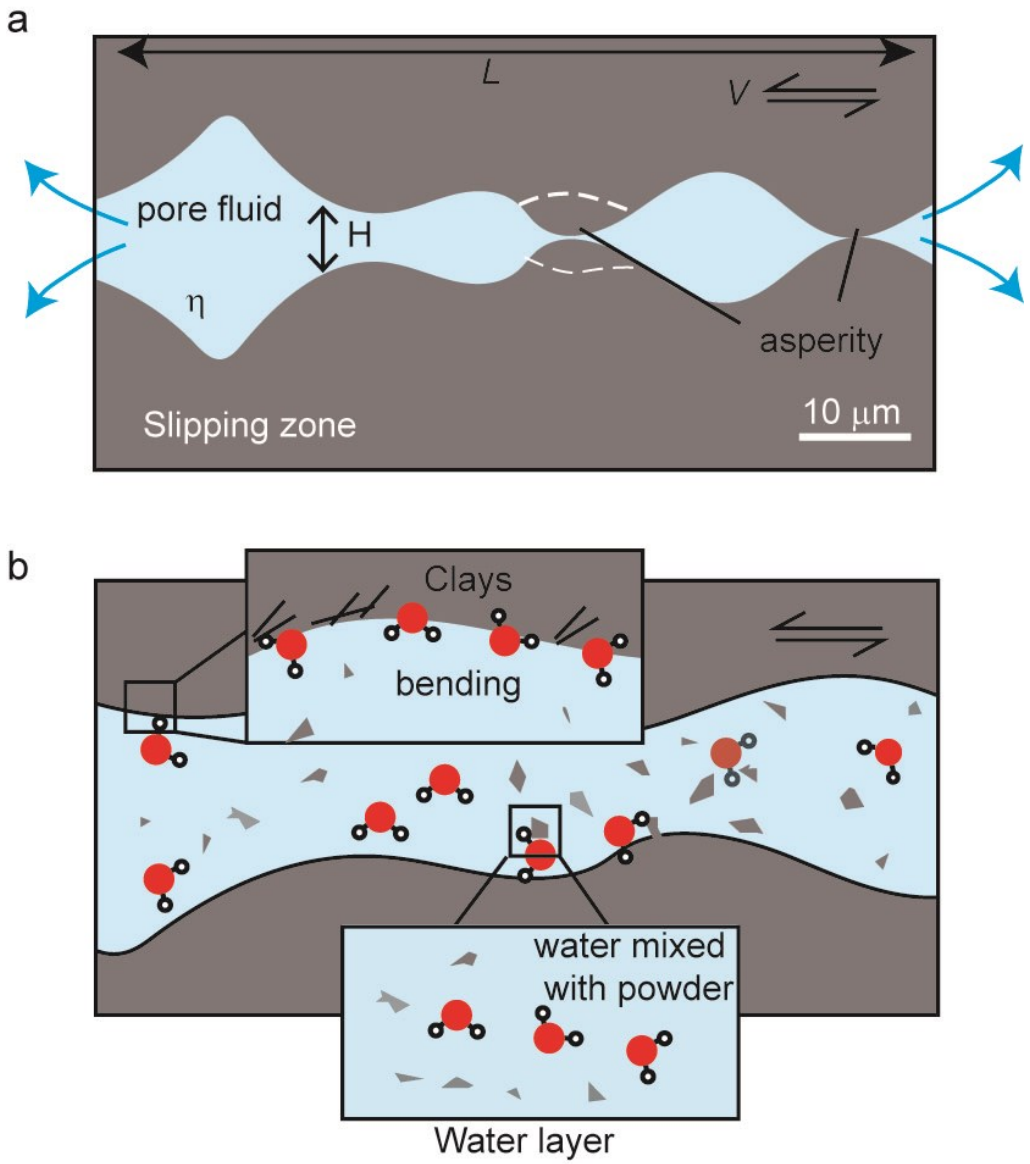

Figure 3.13: Schematic diagram showing the weakening mechanisms operating during fault sliding in the presence of water in liquid and supercritical states. **a.** At the beginning of the experiment, the slip zone includes hot, pressurized water and two fault surfaces have microscopic asperities. **b.** During sliding, the rubbing of the surfaces produces rock powders; water-rock interaction result in the formation of clay minerals and phyllosilicates (Figure 3.6). This assemblage of slip zone traps water which has a vibrational mode (Figure 3.7) typical of H-O-H bending. This bending may result

in a weakening of the intermolecular hydrogen–bonding O···H. The water in liquid and supercritical states mixed with rock powders exhibits a significant increase in viscosity, potentially facilitating the activation of EHD mixed lubrication (Figure 3.11).

3.6 Conclusions

In this study, we exploited a dedicated hydrothermal vessel to shear solid gabbro in the presence of water in liquid, vapor and supercritical state. Results demonstrated that the frictional strength of the gabbro-built fault can be as low as 0.3 at subseismic slip velocity when water is in liquid and supercritical state and suggested that the physical state of the water can control the fault friction. To investigate the underlying causes of the differences in friction behavior, microanalyses of the sheared samples showed that newly formed clay minerals and detected H-O-H bending mode of H_2O was associated with measured low friction. In addition, EHD could be activated at low velocities in the liquid and supercritical water conditions, potentially lubricating the fault. Our results suggest that the phase change of pore water from liquid to vapor may stabilize the fault sliding and rupture in nature.

3.7 Appendices

3.7.1 Modeling of the temperature evolution in the slipping zone

The temperature increase due to shear heating was estimated using a coupled Finite Element Analysis 2-D time-dependent model in Matlab®. In this model, we computed the heat source and heat dissipation in time and space. We considered a 2-D sample (28 x 25 mm, or the diameter versus height of each cylinder of gabbro) bounding the water-saturated slip zone. The initial effective normal stress was equal to the one imposed in the experiments. Fluid thermal and physical (e.g., thermal conductivity, density, compressibility) properties were taken from NIST database as a function of temperature T_0 and fluid pressure P_0 imposed during the experiments (e.g., vapor, supercritical and

liquid states; see Supplementary Table 3). Two different materials were used to simulate the experimental slip zone and the wall rocks (gabbro). The wall rock was regarded as very low porous media, whereas the initial porosity of the slip zone was $\phi = 1 - A_r/A = 0.95$, where A_r is the real contact area and A is the nominal area of the slip surface. The thermal and hydraulic properties of the slipping zone were defined as a linear combination of the thermal properties $k_{eff} = (1- \phi)$ x $k_r + \phi$ x k_f and $\rho C_{eff} = \rho_r$ x C_r x $(1- \phi) + \rho_f$ x C_f x ϕ, where the subscripts r and f are related to the rock and fluid properties, respectively. The fluids and rock properties were considered constant during the modeled experiments. In the model, the experimental fault is sheared at the imposed slip velocity $V(t, r)$. We assumed that all the mechanical energy is dissipated as heat, so the heat flux $Q(r,t) = 0.5 \cdot \tau(t) \cdot V(r,t)$ is a function of time t and the radial displacement r from the center of the sample. A Neumann boundary condition was applied to the bottom external edge (i.e., slip zone) of the model to consider the flux of heat due to shearing. On the other three external boundaries, a constant temperature $T = T_0$ as the initial experimental temperature of the two materials and a constant fluid pressure $P_p = P_0$ function of the experimental conditions (Table 3.2) for the slipping zone were imposed. At the inner boundary between the slip zone and the wall rock, the continuity of the solution was granted.

Table 3.2: Fluid and rock properties. K thermal conductivity, ρ density, C specific heat. Properties were taken from NIST database for thermophysical properties of fluids (based on the IAPWS97 industrial thermodynamic formulation) at different pressures. Gabbro properties from (Rempel and Weave, 2008).

	K **[W/mK]**	***r*** **[kg/m^3]**	***C*** **[J/(kgK)]**
Liquid (T = 577K, P_p = 10 MPa)	0.54841	700	5830
Vapor (T = 675K, P_p = 10 MPa)	0.06878	40	3075
Supercritical (T = 675K, P_p = 30 MPa)	0.32453	250	27000
Gabbro	2.5	2590	1480

3.7.2 Micro-Raman spectroscopy data

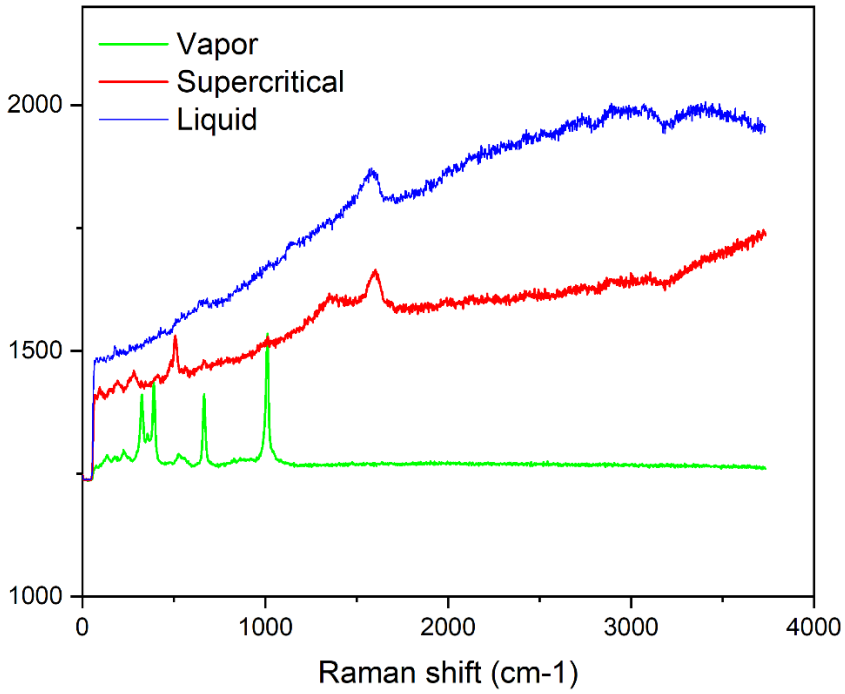

Figure 3.13: Micro-Raman spectra data for experiments performed at V =10 μm/s with water in liquid (LHV2398), supercritical (LHV2380) and vapor (LHV 2391) states. Similar to the experiment at V = 1 mm/s, a peak of H–O–H bending vibration mod is only present in experiments with liquid and supercritical water.

3.7.3 Data from the experiments performed at effective normal stress of 20 MPa

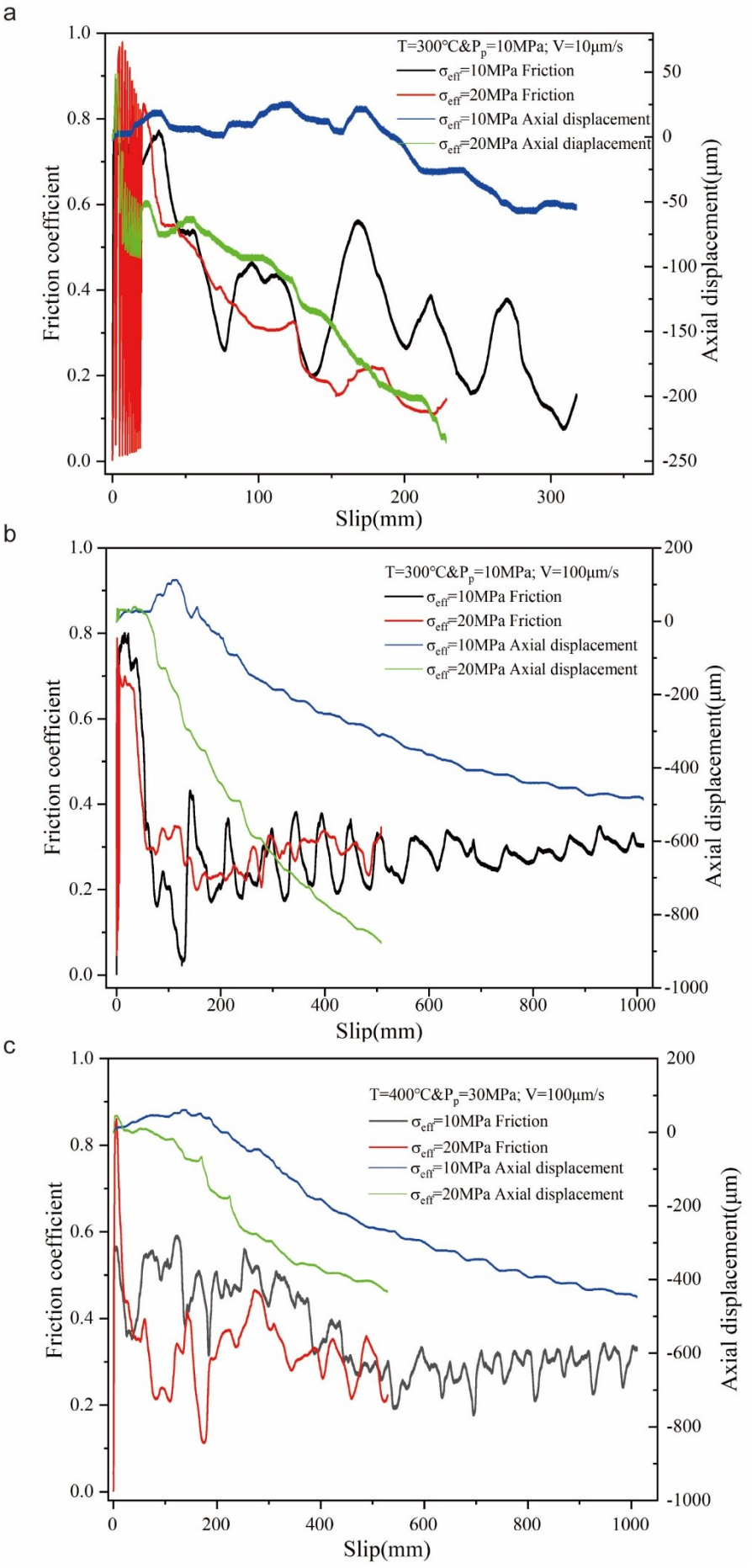
a
T=300°C&P$_p$=10MPa; V=10μm/s
σ$_{eff}$=10MPa Friction
σ$_{eff}$=20MPa Friction
σ$_{eff}$=10MPa Axial displacement
σ$_{eff}$=20MPa Axial diaplacement
Friction coefficient
Axial displacement(μm)
Slip(mm)
b
T=300°C&P$_p$=10MPa; V=100μm/s
σ$_{eff}$=10MPa Friction
σ$_{eff}$=20MPa Friction
σ$_{eff}$=10MPa Axial displacement
σ$_{eff}$=20MPa Axial displacement
Friction coefficient
Axial displacement(μm)
Slip(mm)
c
T=400°C&P$_p$=30MPa; V=100μm/s
σ$_{eff}$=10MPa Friction
σ$_{eff}$=20MPa Friction
σ$_{eff}$=10MPa Axial displacement
σ$_{eff}$=20MPa Axial displacement
Friction coefficient
Axial displacement(μm)
Slip(mm)

Figure 3.14: Friction coefficient and shortening versus slip displacement from the experiments performed at 20 MPa effective normal stress including experiments at 10 MPa normal stress for comparison (Curves in black and red are friction coefficient, and curves in blue and green are shortening under 10MPa and 20MPa normal stress, respectively). **a**. T=300°C, Pp=10 MPa, V=10 μm/s; **b.** T=300°C, Pp=10 MPa, V=100 μm/s; **c.** T=400°C, Pp=30 MPa, V=100 μm/s. Collectively, the friction coefficient shows similar evolution regardless of normal stress and the shortening rate is greater at 20 MPa normal stress.

3.7.4 Microstructures of deformed samples

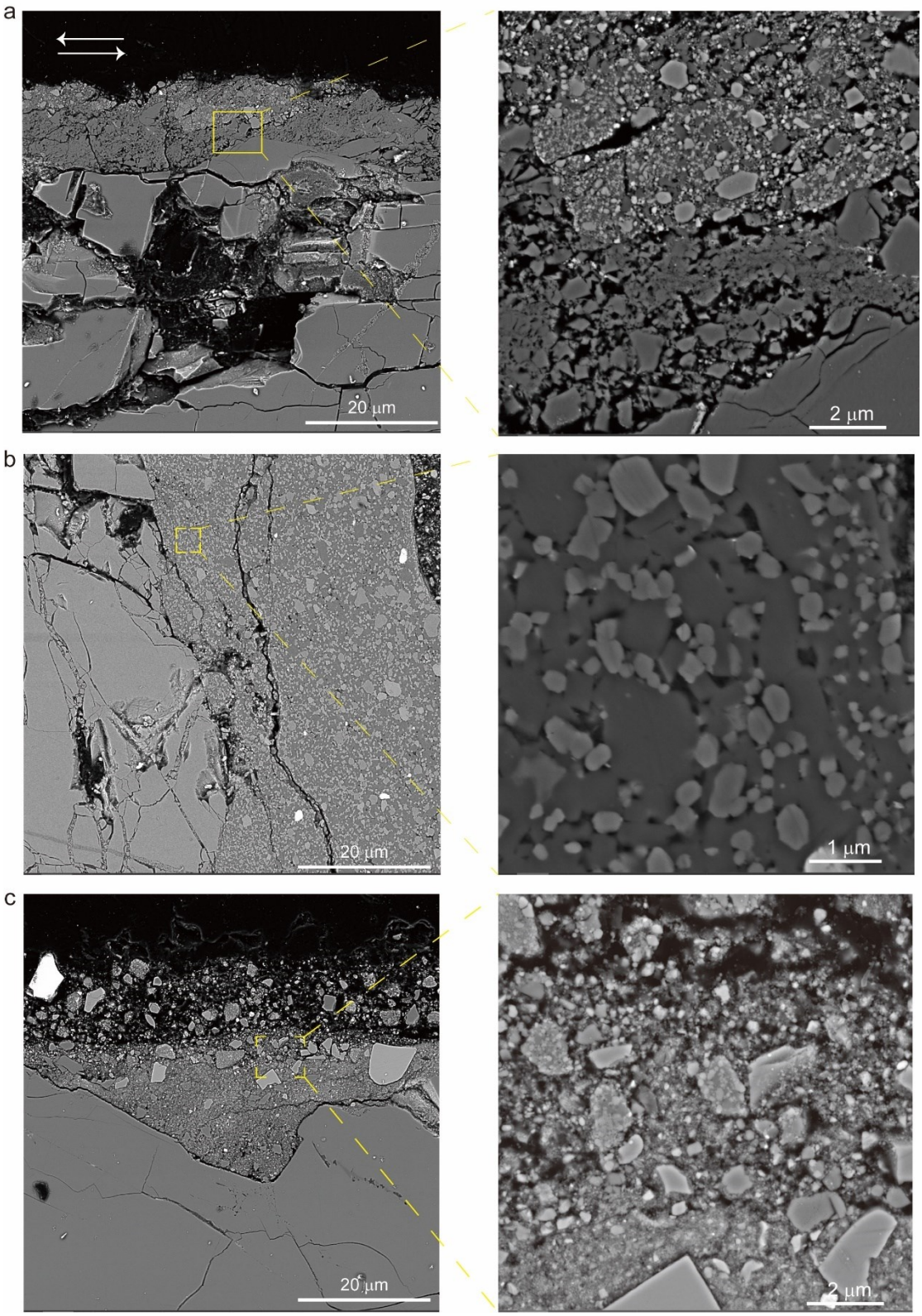

Figure 3.15: Characteristic microstructures of the experiments performed at seismic slip velocity V=0.1 m/s. **a.** Experiment LHV2360 (water in liquid state); **b.** Experiment LHV2369 (water in supercritical state); **c.** Experiment LHV2363 (water in vapor state).

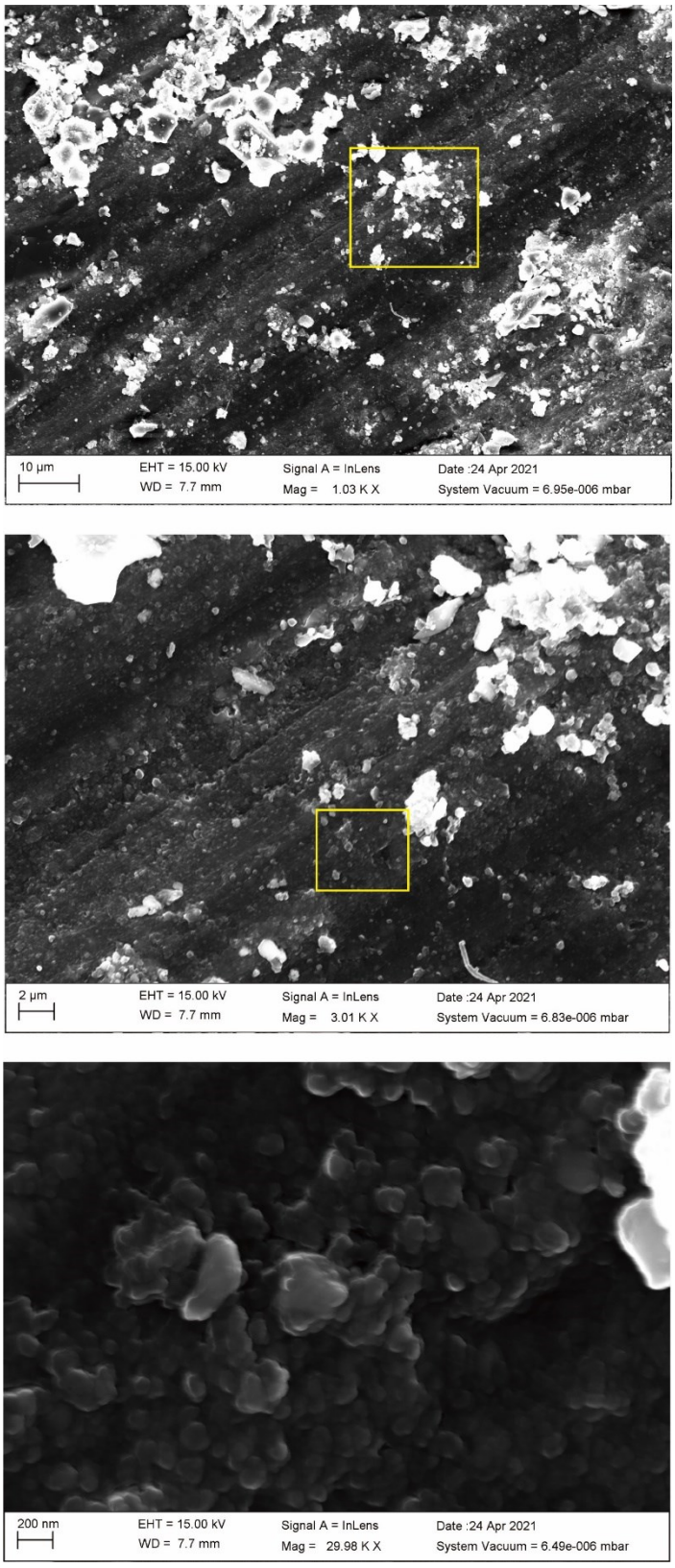

Figure 3.16: lnLens SEM images of the slip surfaces from experiment (LHV2340) performed at V = 100 mm/s, T=300°C and P_p=10 MPa (water in liquid state). The yellow square marks the position of the respective lower image.

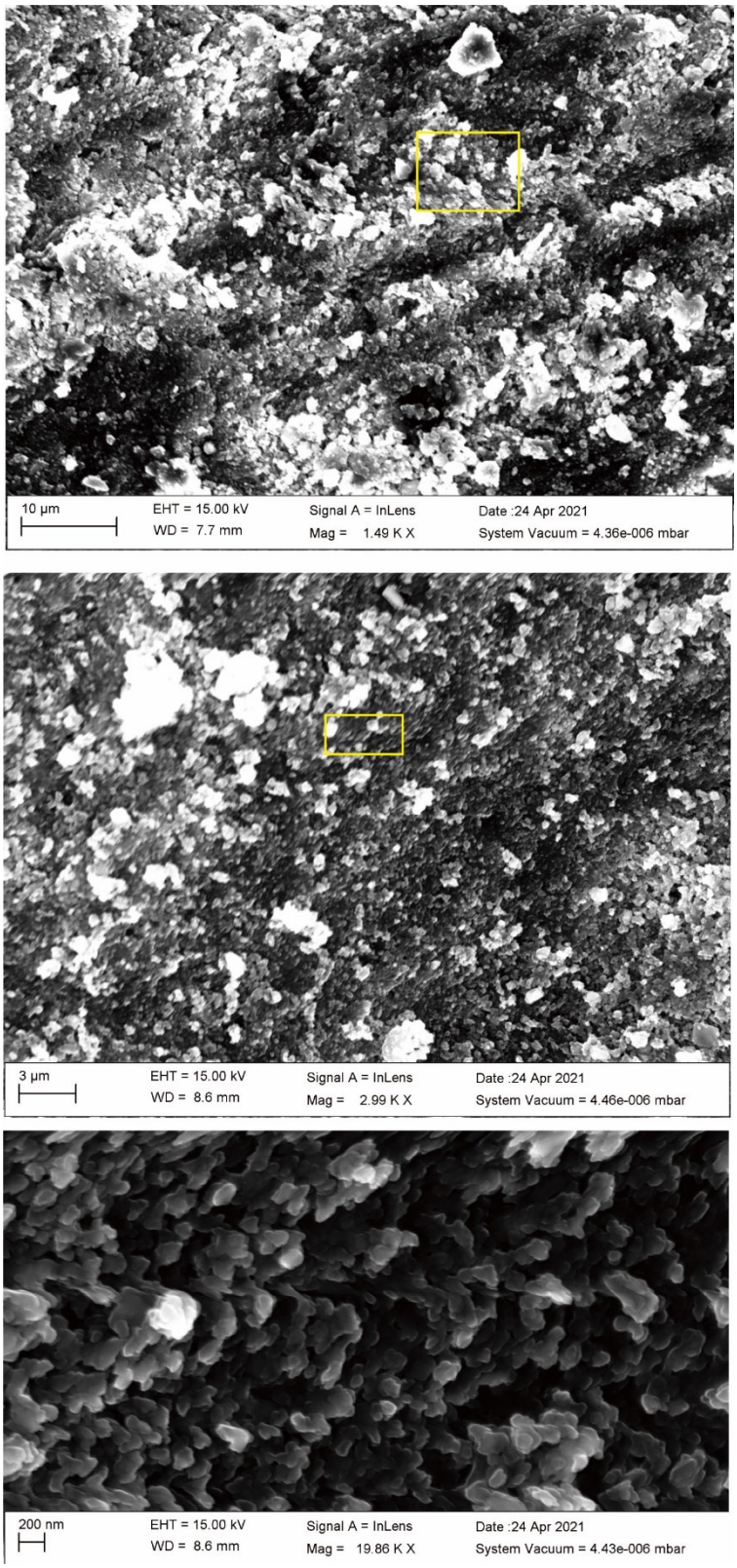

Figure 3.17: lnLens SEM images of the slip surfaces from experiment (LHV2388) performed at V = 100 mm/s at T=400°C and P_p=10 MPa (water in vapor state).

Chapter 4 Frictional healing of gabbro-built fault gouges under hydrothermal conditions

Authors: Wei Feng[1,2], Lu Yao[2], Rodrigo Gomila[1], Shengli Ma[2] and Giulio Di Toro[1,3]

[1] Dipartimento di Geoscienze, Università degli Studi di Padova, Padua, Italy

[2]State Key Laboratory of Earthquake Dynamics, Institute of Geology, China Earthquake Administration, Beijing, China

[3]Sezione Roma 1, Istituto Nazionale di Geofisica e Vulcanologia, Rome, Italy

Status: to be submitted to *Geophysical Research Letters*

Contributions: W.F., L.Y. and G.D.T. conceived the study. W.F. and L.Y. performed the experiments. W.F. and R.G. carried out the microstructural analysis. W.F. wrote the first draft of the manuscript with inputs from L.Y. and G.D.T. All authors discussed and interpreted the results.

4.1 Abstract

Fault frictional restrengthening (healing) allows country rocks to store elastic strain energy during the interseismic period to be released in the next earthquake. Laboratory studies revealed that fault healing increases linearly with the log-duration of the interseismic period (i.e., hold time). Here, by using an on-purpose hydrothermal vessel, we investigate frictional healing in the presence of hot and pressurized fluids, or ambient conditions often met at crustal seismogenic depths but poorly investigated so far. We show that (1) the log-linear relation between frictional healing and hold time is relaxed at temperature > 200°C, especially in the presence of pressurized water, and (2) the healing rate switches from positive to negative for hold durations longer than a threshold time. These observations can be interpreted as a result of the competing effects of increased contact area and decreased contact strength. In nature, the reduction of the fault healing rate under hydrothermal conditions may slow down the rate of elastic energy storage in the country rocks over time, which in turn lowers the shear stress required for the next earthquake rupture.

4.2 Introduction

Earthquakes are the result of ruptures that nucleate, propagate and terminate mostly along pre-existing faults (Scholz, 2019). During an earthquake, faults slip at average velocities of meters per second (Heaton, 1990). Under these deformation conditions, in the upper Earth's crust, depending on rock composition, state of cohesion, presence of fluids, etc., various fault dynamic weakening mechanisms can be activated, resulting in a significant reduction in fault strength (Sibson, 1972; Bizzarri and Cocco, 2006; Rice, 2006; Goldsby and Tullis, 2011; Hirose and Shimamoto, 2005; Wibberley and Shimamoto, 2005; Han et al., 2007; Reches and Lockner, 2010; Di Toro et al., 2004; 2006; 2011; Pozzi et al., 2021; Tullis, 2015; De Paola et al., 2015). However, for earthquakes to repeatedly occur, faults require to regain their strength during the

interseismic period: this process allows the country rocks to restore the elastic strain energy that will fuel the next earthquake (Reid, 1910; Brace and Byerlee, 1966; Burridge and Knopoff, 1967; Dieterich, 1972; Perrin et al., 1995; Heimpel, 1997). The occurrence of fault postseismic to interseismic restrengthening (or healing) has been confirmed by geological, seismological and geophysical field studies (Di Toro and Pennacchioni, 2005; Masoch et al., 2019; Scholz et al., 1986; Marone et al., 1995). However, our understanding of how faults recover their strength when they are held in quasi-stationary contact is matter of discussion.

Laboratory studies can provide insights into the mechanisms of fault healing. Over the last 40 years, frictional healing has been extensively investigated by performing slide-hold-slide (SHS) experiments aimed at reproducing the seismic cycle on a broad range of rock types (Carpenter et al., 2016 and references therein) and also in single-asperity at the atomic scale (Li et al., 2011). SHS experiments consist of three steps: (1) sliding the rocks at a constant slip velocity V, (2) holding the rocks for increasing time intervals t_h and, (3) sliding the rocks at the former V before the hold (Dieterich, 1972; Marone, 1998). Experiments revealed that frictional healing increases with the logarithm of the hold time t_h (Dieterich, 1972; Marone, 1998; Nakatani and Scholz, 2004). Starting from the asperity model of solid friction proposed by Bowden and Tabor (1950), the time-dependence of frictional healing is interpreted as due to the "*quantity*" and "*quality*" of the asperity contacts. "*Quantity*" refers to the increase in the real area of contact of the microscopic asperities (i.e., larger the real area of contact, higher the fault strength), while "*quality*" refers to the chemical bonding of contact (i.e., stronger the bonds between the asperities, higher the fault strength) (Dieterich and Kilgore,1994; Li et al., 2011). Thus, fault healing is related to mineral composition, normal stress, loading velocity, temperature and pore fluid pressure (Frye and Marone, 2002; Dieterich, 1972; Mitchell et al., 2013; Chen et al., 2015). Since natural faults in the upper Earth's crust heal and seal in most cases under hydrothermal conditions, fluid-assisted and thermally-activated processes (reaction kinetics, pressure-solution transfer, mineral precipitation,

sub-critical crack growth, etc.) play a pivotal role in fault healing (Sibson, 1973; Violay et al., 2014; Verberne et al., 2015; Moore and Lockner, 2013).

In this study, we perform SHS experiments on gabbro-built gouges under dry and hydrothermal (temperature up to 400℃ and pore fluid pressure of 30 MPa) conditions to investigate how the experimental faults recover their strength during quasi-stationary contact periods. We observe that frictional healing of gabbro increases linearly with the logarithm of the hold time at dry and relatively low temperatures conditions, whereas at higher temperature and especially under hydrothermal conditions, the healing rates switches from positive to negative with increasing the hold time. We interpret that frictional healing is attributed to the competing effects of contact quantity and quality under hydrothermal conditions when the thermally-activated chemical processes are active.

4.3 Methods

The rock powders used in the experiments were obtained from the "Jinan green black" gabbro. The mineralogical (XRD) and chemical (XRF) compositions are presented in Chapter 2. The samples were crushed and sieved using a 180-mesh sieve to produce gouges with grain size < 88 μm for the experiments.

Friction experiments were performed with the Low to High Velocity Rotary shear apparatus (LHVR-Beijing) equipped with an on-purpose hydrothermal pressure vessel at the Institute of Geology, China Earthquake Administration in Beijing, China (Ma et al., 2014). All experiments were conducted at a constant effective normal stress (σ_{eff}) of 50MPa and temperature (T) ranging from 25 to 400 ℃ under nominally "dry" or pore fluid pressure (P_p) of 30 MPa. In the dry experiments, the vessel was open to the atmosphere. When $T \geq 100$℃, the moisture inside the vessel evaporated to water vapor and the sample was in a "dry" condition. The P_p= 30MPa experiments were conducted under drained conditions and constant pore pressure was maintained by a syringe pump.

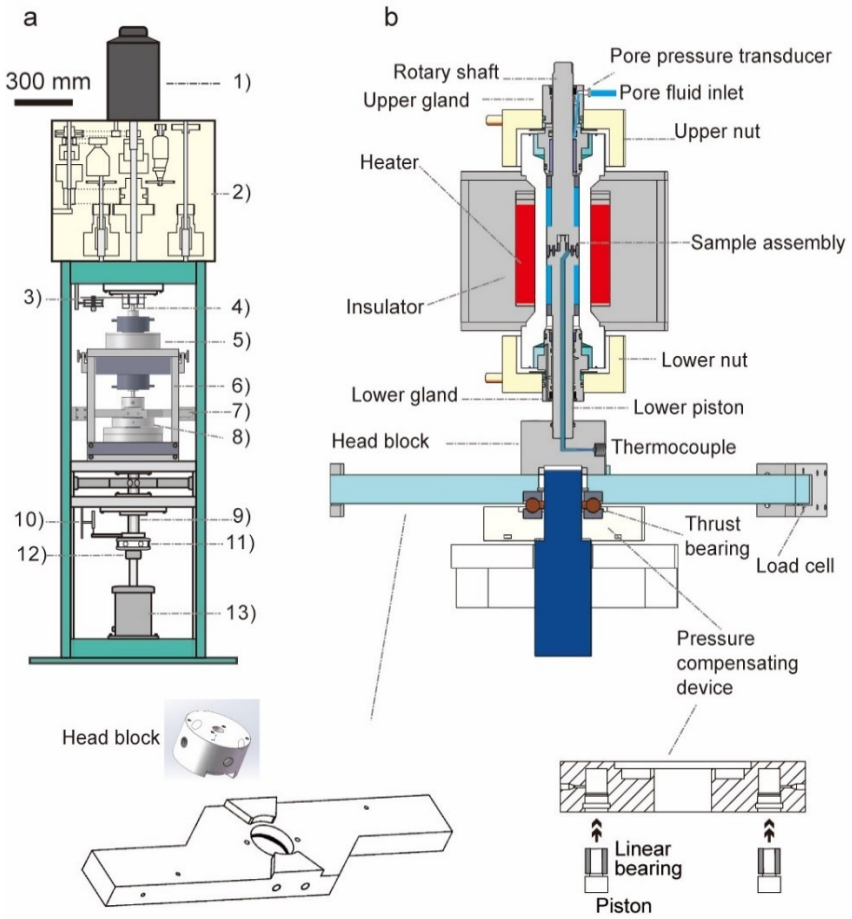

Figure 4.1: Experimental setup. a. The Low to High velocity rotary shear apparatus, equipped with a dedicated hydrothermal vessel (modified from Ma et al., 2014). 1) servomotor, 2) gear and belt system, 3) rotary encoder and potentiometer, 4) rotary shaft, 5) hydrothermal pressure vessel, 6) metal frame, 7) cantilever-type torque gauge, 8) pressure compensating device (designed by Lu Yao), 9) axial loading column, 10) liner voltage displacement transducer, 11) thrust bearing, 12) axial force gauge, 13) air actuator. Note that when the new torque measurement unit 7) was used, the old one connected to the lower loading column (8) in Figure 2.1) did not support any shear torque as the load cells attached to the arms were removed. **b.** The sketch of the hydrothermal vessel with the main parts indicated in the diagram and the updated pressure compensating system.

In each experiment, about 0.8 g of gouge powder was sandwiched between two ring-shaped and surface-grooved holders and flanked by inner and outer metal rings (22/28 mm internal/external diameter), resulting in an initial gouge thickness of 1.5 mm. The sample assembly was subsequently mounted inside the hydrothermal vessel and to the

machine. Then, the sample assembly and the vessel were evacuated to 2000 Pa with a vacuum pump, and then saturated with deionized H_2O. Afterward, the normal stress σ_n was slowly increased to the desired value, while the pore fluid pressure (P_p) was increased in a stepped manner and kept at a constant target value before heating.

After achieving the desired experimental conditions, the gouge layer was sheared (run-in) at V = 10 μm/s for 7 mm slip displacement (d), allowing friction to evolve to a steady state value. After the "run-in" stage, velocity-stepping and SHS sequences were imposed. The SHS sequences consisted of three steps: (1) sliding the gouge later at V = 10 μm/s for 1 mm of slip displacement, (2) holding the gouge for hold times (t_h) ranging from 3 s to 10,000 s by setting the load point velocity as null and, (3) resuming the sliding velocity at the former one (V = 10 μm/s). Upon reloading, the friction coefficient typically reached a peak value and then decayed to a steady state value. There was no unloading stage during the holds (Karner and Marone, 1998) and frictional strength relaxed non-linearly due to the creep of the machine and gouge samples (Figure 4.2). To ensure that no rotation was applied by the machine on the gouge layer during holds, the motor control system was set to stop once the imposed velocity was less than a certain value. No angular rotations were detected during the holds (Figure 4.2). In each experiment, two SHS sequences separated by a slip displacement of 40 mm were imposed to investigate the effect of slip displacement on frictional healing and healing rates (Figure 4.3). Additional experiments were performed with only one SHS sequence for microstructural comparison.

During the experiments, axial load, shear torque, fluid pressure and temperature, velocity, revolution, and axial displacement were acquired at a frequency of 100 Hz. Evolution of axial displacement, i.e., dilatation or shortening (Δw) of the gouge layer, was recorded using the LVDT (1 μm resolution and 10 mm stroke) placed on the axial column of the machine (Figure 4.1). In data processing, no correction for system stiffness was applied for the calculation of the shear displacement. The measured shear torque was converted to shear stress (MPa) without correcting the additional shear

resistance from O-rings.

After the experiments, the gouge samples were carefully retrieved for microanalysis. To investigate the microstructure of the slip zone, part of the recovered gouge layer was impregnated with a low-viscosity epoxy resin, and then cut perpendicular to the slip surface and tangential to the shear direction to prepare thin sections. The microstructural images were collected using a Field Gun Scanning Electron Microscope (SEM) at the Department of Geosciences (Padua University). To determine whether mineralogical reactions caused by fluid-rock interactions occurred, ~10 mg of powders collected from the recovered slip zones were analyzed with X-Ray diffraction (XRD).

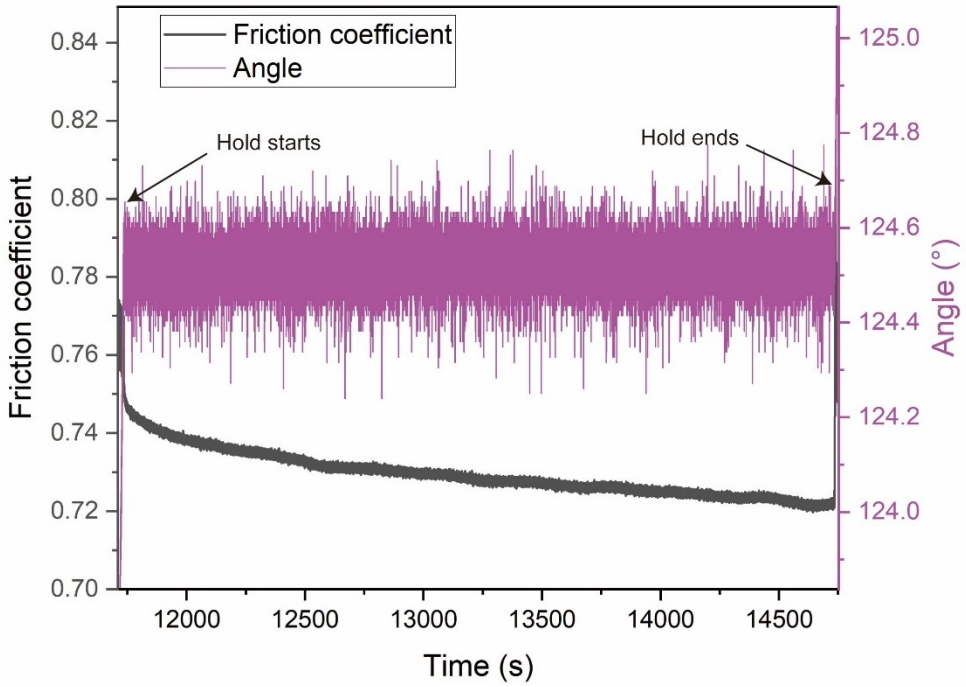

Figure 4.2: Evolution of friction coefficient (black in color line) and angular position (magenta in color line) with time during a 3,000 s hold in the experiment LHV 2755 performed at T= 300°C and P_p = 30 MPa. During the hold, the friction coefficient decay with time due to the gouge and machine system relaxation. No change in angular position (or slip displacement) was detected.

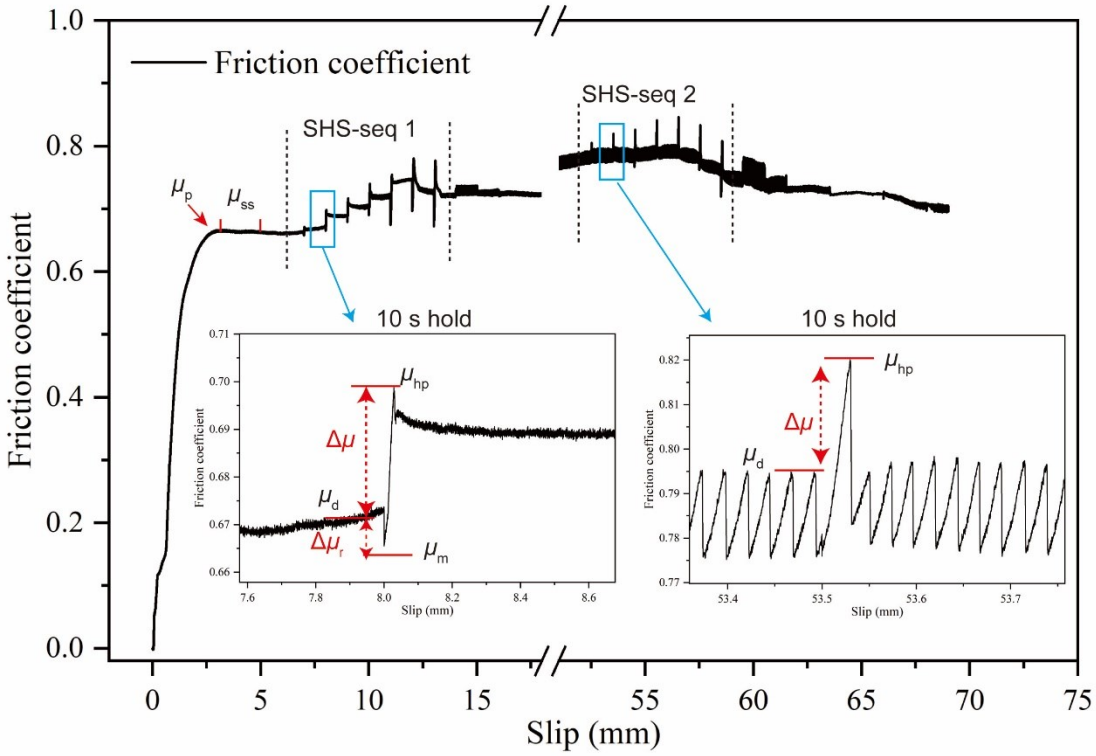

Figure 4.3: Example of an experiment (LHV 2755, T=300, P_p=30 MPa, σ_{eff} =50 MPa) showing the evolution of the friction coefficient with slip. In each experiment, two SHS sequences (SHS-seq 1 and SHS-seq 2) are conducted with a slip interval of 40 mm in between. Frictional healing $\Delta\mu$ is defined as the difference between post hold peak friction (μ_{hp}) upon re-shearing and steady-state friction (μ_d) before the hold (see left inset for the 10 s hold). Stick-slip events occurred in some experiments performed at elevated temperatures and pore pressure. In this case, $\Delta\mu$ was measured as the difference between the peak friction of the stick-slip events after and before the holds (μ_{hp} - μ_d, see right inset for the 10 s hold). The $\Delta\mu_r$ is the frictional relaxation during the hold measured as the difference between steady state friction (μ_d) before the hold and the friction at the end of the hold (μ_m).

4.4 Results

4.4.1 Mechanical data

As an example, the friction coefficient ($\mu = \tau/\sigma_{eff}$, or the ratio of shear stress to effective normal stress) versus slip displacement from experiment LHV2755 conducted at T=300°C

and P_p= 30MPa is plotted in Figure 4.3. During the run-in, the friction coefficient increases in the first 2 mm of slip displacement and near-linearly to a peak value μ_p of 0.63-0.71. This μ is followed by an evolution towards a steady state value μ_{ss} of 0.62-0.74 (picked at 3-5 mm of slip displacement, Figure 4.4), consistent with previous experiments performed on gabbro gouges (He et al., 2006, 2007). There is a slight dependence of the μ_{ss} achieved at slip initiation with temperature: in the dry experiments, μ_{ss} increases, with some scatter, from 0.66 to 0.74 with temperature (T≤ 400 °C). In the presence of pressurized water (P_p= 30MPa), μ_{ss} increases from 0.62 to 0.74 until T = 200 °C and then it remains at ~ 0.67 at T =300 and 400 °C. At these latter high temperatures, the presence of pressurized water reduces μ_{ss} with respect to the dry cases (Figure 4.4).

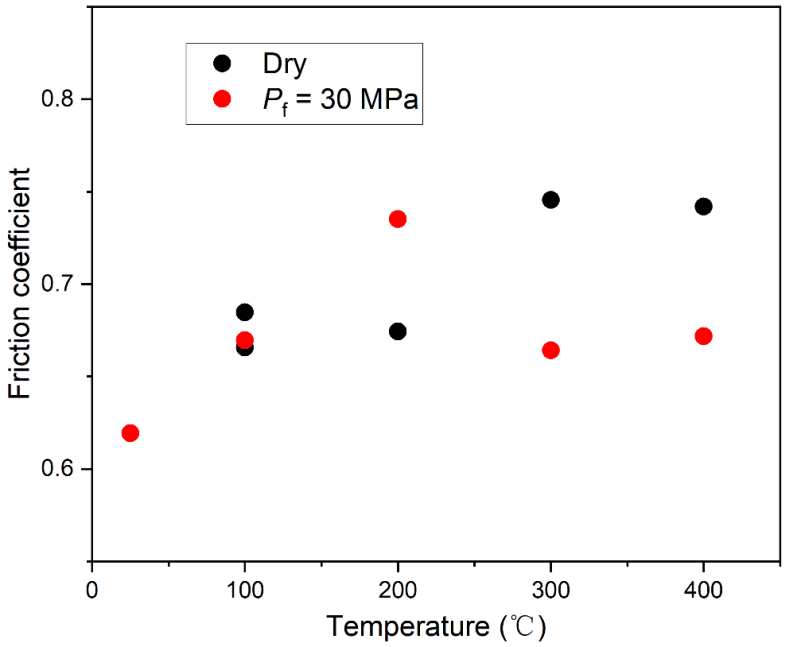

Figure 4.4: Steady state friction coefficient μ_{ss} of gabbro gouges at 3-5 mm slip displacement versus temperature under dry conditions or in the presence of pressurized water (P_p =30 MPa). See main text for description.

After run in and reaching steady state, the first SHS sequence is started. During each hold, μ decays with time (Figure 4.2) and we measure (1) frictional healing $\Delta\mu$ or difference between μ peak value (μ_{hp}) during the resuming of sliding velocity and

steady state friction (μ_d) before the hold (Dieterich, 1972; Marone, 1998) and, (2) the relaxation $\Delta\mu_r$ or difference between μ_d before the hold and μ_m at the end of hold (Figure 4.3 inset). Stick-slip events occurred in some experiments performed at elevated temperatures and pore pressure. In this case, $\Delta\mu$ is measured as the difference between the μ peak value of the stick-slip events after and before the holds (Figure 4.3 inset).

In most experiments reported in the literature (Carpenter et al., 2016 and references therein), $\Delta\mu$ increases linearly with the $\log_{10}t_h$, and the healing rate β is (Marone, 1998):

$$\beta=\Delta\mu / \Delta\log_{10}t_h$$

Dry conditions experiments. $\Delta\mu$ increases linearly with $\log_{10}t_h$ at most investigated temperatures. However, in the 2nd sequences at T=300°C and 400°C (empty purple and green in color triangles in Figure 4.5a), the log-linear relation $\Delta\mu$ vs. t_h is relaxed. For t_h >300 s, $\Delta\mu$ saturates and even decreases with the hold time. The slope of $d(\Delta\mu)/d[\log_{10}t_h]$ decreases, resulting in a change in β (i.e., $\beta_2<\beta_1$). Moreover, β values scatter with temperature (Figure 4.5b). T=100°C results in the maximum β value of 0.0145-0.0174, T= 200°C the minimum β= 0.0027-0.0073. Collectively, the values of $\Delta\mu$ at a given t_h and β in the linear $\Delta\mu$–t_h regime are slightly higher in the 2nd sequence than in the 1st sequence (Figure 4.5b). This indicates a slip-dependence of fault healing.

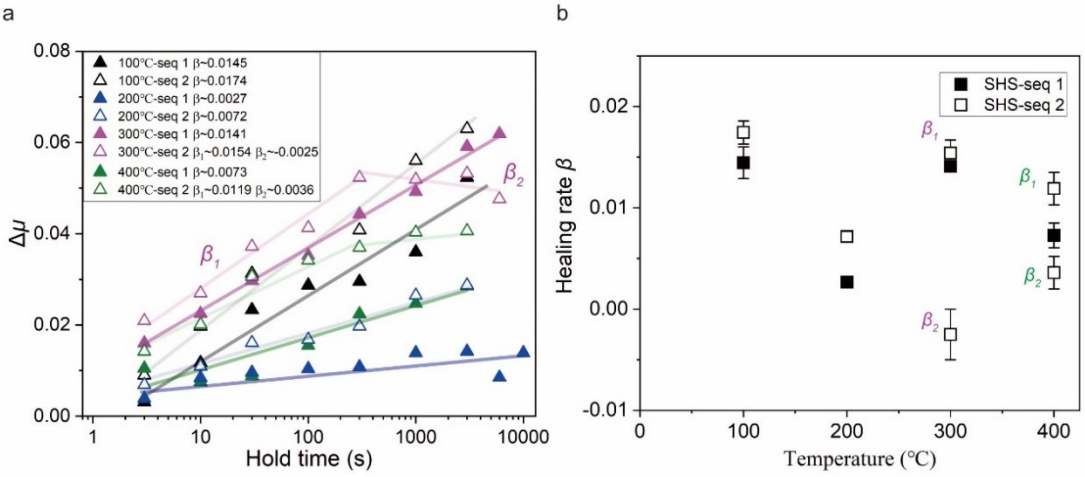

Figure 4.5: Dry conditions experiments: **a.** Frictional healing $\Delta\mu$ versus the logarithm of hold time t_h. Two types of SHS behaviors are observed: (1) log-linear relation between $\Delta\mu$ and $\log_{10}t_h$ for most investigated ambient temperatures and, (2) for the 2nd sequence at T=300 and 400°C, $\Delta\mu$ saturates

or decreases with increasing $\log_{10}t_h$, resulting in a change in β. **b.** Frictional healing rates β versus temperature. No monotonic linear relation between the healing rate β and temperature is observed.

Pressurized water experiments. In the presence of pressurized water (P_p=30 MPa), the gabbro gouges have a more complex frictional healing behavior than under dry conditions (Figure 4.6). At T=25°C and 100°C, $\Delta\mu$ increases linearly with $\log_{10}t_h$, and both $\Delta\mu$ and β are larger in the 2nd SHS sequence than in the 1st SHS sequence (room T: β=0.0096 for seq-1 and 0.0118 for seq-2; T = 100°C: β=0.0091 and 0.0119, respectively, see Figures 4.6a, b, f), in agreement with the data obtained under dry conditions (Figure 4.5). Instead, at T = 200°C, $\Delta\mu$ is small, has a poor dependence with t_h and decreases with increasing t_h for t_h >300 s (β_2= ~ -0.0073 and -0.0053 for two sequences, Figures 4.6c, f). At T = 300 and 400°C, the linear relation between $\Delta\mu$ and $\log_{10}t_h$ does not hold in either sequence. Moreover, in the 2nd sequence (empty triangles in Figures 4.6d, e), β switches from positive to negative at t_h =300 s and 100 s for T = 300°C (β_1= 0.016 to β_2= -0.0074) and 400°C (β_1= 0.0057 to β_2= -0.0227), respectively (Figure 4.6f).

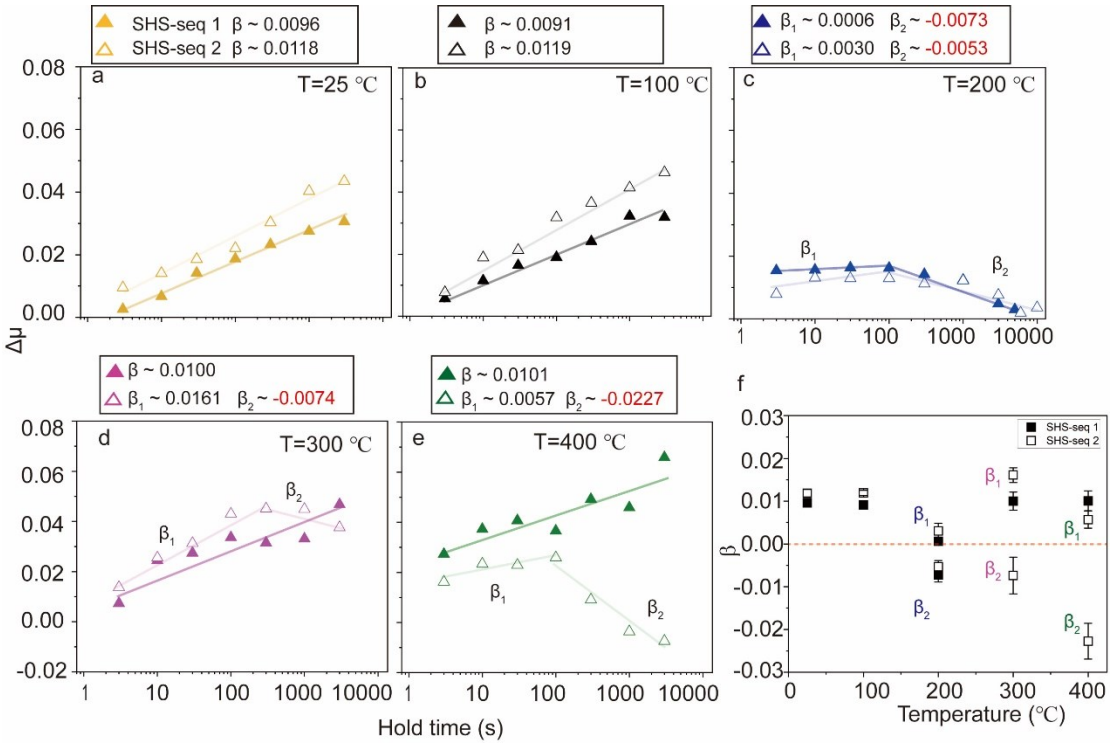

Figure 4.6: Pressurized water experiments: **a-e.** Frictional healing $\Delta\mu$ as a function of the $\log_{10}$ of

hold time t_h at T from 25°C to 400°C. Above 200°C, $\Delta\mu$ decreases with $\log_{10}t_h$ when t_h is longer than a certain threshold time. **f.** Frictional healing rate β versus temperature. See main text.

4.4.2 Microanalysis of starting and deformed gouges

Microstructures

The microstructures of the deformed samples were investigated under the FESEM in backscatter electron (BSE) mode. The samples sheared at T = 300°C and 400°C were not fully recovered since they were non-cohesive after the experiments. In all the experiments, grain size reduction was observed in both the upper and lower side of the sheared gouge layer.

Dry conditions experiments: at T=100°C after the two SHS sequences (LHV2759, d=70 mm), deformation is mainly localized in a ~80 μm thick Y-shear zone (Figure 4.7a), where grain size is reduced to 1 μm (Figure 4.7b).

Pressurized water experiments: at T=100°C and P_p=30 MPa after the two SHS sequences (LHV2733, d=70 mm), the deformed gouge layer contains a well-defined 100 μm-thick upper shear band (Figure 4.7c), characterized by multiple sub-parallel Y-shears. Here, grain size reduction (<1 μm) is extreme along each slip plane (Figure 4.7d).

At T = 200°C and P_p=30 MPa the healing rate β switches from positive to negative with the hold time, similarly as in the experiments performed at T=300°C and 400°C (Figure 4.6). Consequently, the microstructure from the T=200°C experiment is considered representative for this frictional behavior. When the experiment is stopped after the 1st SHS sequence (LHV2783, d=15 mm), the gouge layer includes a ~ 500 μm-thick shear band and R-shears are highly developed (Figure 4.7e). When the experiment is stopped after the 2nd SHS sequence (LHV2760, d=70 mm), strain is localized in an upper ~500 μm-thick and in a lower ~200 μm-thick shear band. The upper shear band includes

multiple Y-shears (Figures 4.7f-g), and R-shears depart from it.

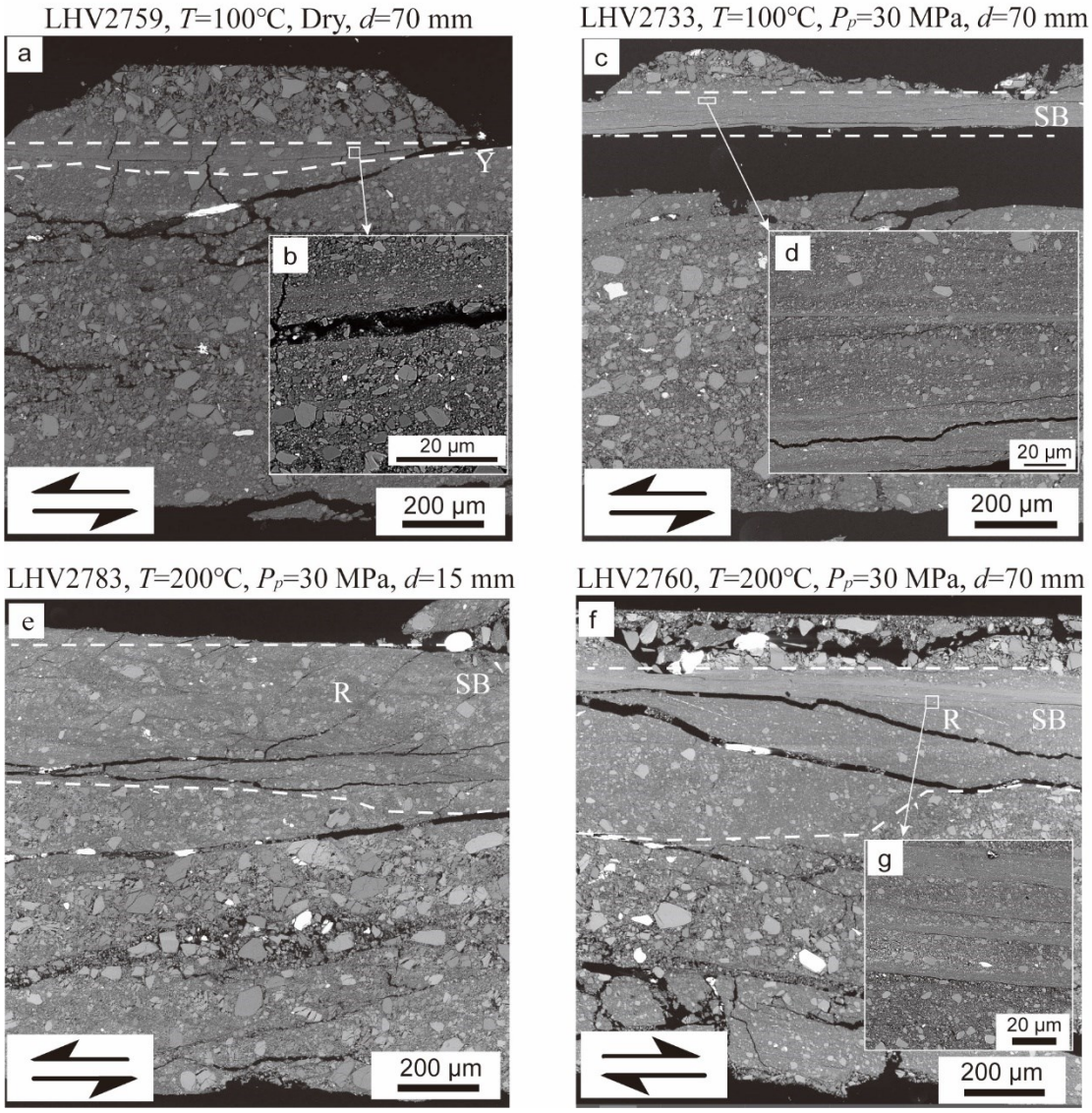

Figure 4.7: Microstructures of the sheared gouge layers under dry (a) and P_p=30 MPa (b-f) conditions. **a-b.** Experiment LHV2759 at T= 100°C and dry conditions, d=70 mm. **c-d.** Experiment LHV2733 at T= 100°C and P_p=30 MPa, d=70 mm. **e.** Experiment LHV2783 at T= 200°C and P_p=30 MPa, d=15 mm. **f-g.** Experiment LHV2760 at T= 200°C and P_p=30 MPa, d=70 mm. SB: Shear band; R: Riedel shear; Y: Y-shear.

Mineralogical composition

The mineral assemblage of deformed gouges recovered from two experiments

performed at T = 200°C (LHV2783 and LHV2760, ~15 and ~70 mm of slip displacement, respectively) and of the starting gouge is similar (Figure 4.8). This suggests that no new minerals are formed or the amount of new minerals formed by the rock-fluid interaction is negligible (that is, below the resolution of the measurement). However, we observe a gradual decrease in the intensity peaks in the spectrum of biotite with increasing slip displacement and time duration of the experiment. Moreover, a peak at 17° is detected in the experiment LHV2760. This signal corresponds to molybdenite (MoS_2), which is the main component of the lubricating coating used to reduce the extra friction from confining rings.

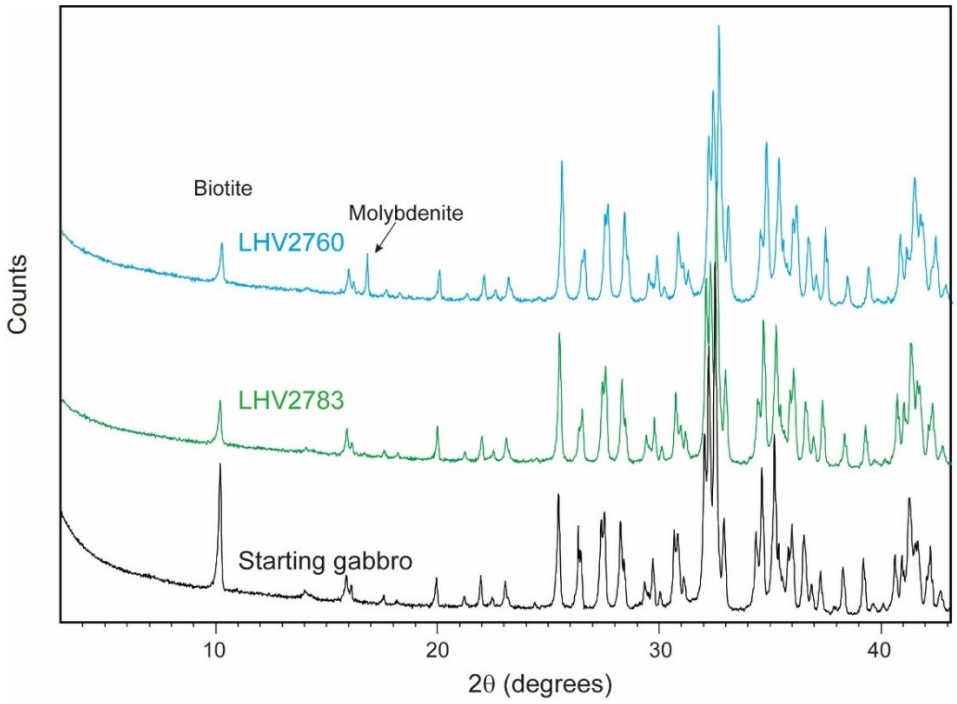

Figure 4.8: X-ray diffraction (XRD) patterns of the starting gabbro gouge and of two deformed gouge layers recovered from experiments LHV2783 and LHV2760 (~15 and ~ 70 mm of slip displacement, respectively) performed at T= 200°C and P_p = 30 MPa. A gradual decrease in the intensity of biotite with increasing slip displacement is the only significant mineralogical variation detected. Instead, the presence of MoS_2, used to lubricate confining rings, in the experiment LHV2760 is indicative of contamination.

4.5 Discussion

4.5.1 Interpretation of experimental observations

The analysis and comparison of the experimental data presented in Figure 4.5 (dry conditions) and Figure 4.6 (pressurized water conditions) reveal systematic similarities and differences in frictional healing properties of gabbro-built gouges. These include: (1) when gouges are deformed under dry conditions at $T \leq 200$°C or under hydrothermal conditions at $T \leq 100$°C, $\Delta\mu$ increases log-linearly with t_h and the healing rate β is positive (Figures 4.5 and 4.6). This observation is consistent with previous studies (Marone, 1998; Carpenter et al., 2016 and references therein). (2) when gouges are deformed under dry conditions at $T \geq 300$°C with large slip displacement or under hydrothermal conditions at $T \geq 200$°C, the log-linear relation between $\Delta\mu$ and t_h does not hold and $\Delta\mu$ transitions from time-dependent increasing to decreasing when t_h exceeds a threshold time (Figures 4.5 and 4.6). As a consequence, the healing rate β switches from positive (β_1) to negative (β_2) values with increasing hold time (Figure 4.6f).

Low values of frictional healing $\Delta\mu$ and healing rates β have been observed in experiments performed on phyllosilicate-rich samples (Bos and Spiers, 2000; Tesei et al., 2012; Carpenter et al., 2016; Niemeijer and Spiers, 2006). Saturation of real contact area due to the presence of phyllosilicates contributes to reduced frictional healing (Tesei et al., 2012; Bos and Spier, 2000; Saffer and Marone, 2003). As a consequence, the decrease in $\Delta\mu$ measured after long-duration holds in the experiments performed at $T \geq 200$°C could be related to the formation of minerals with low frictional healing properties. However, contrary to our observations, in these previous studies a friction peak upon re-shearing after the hold is absent. Moreover, newly-formed phyllosilicates were not detected in both XRD analysis and high-resolution FESEM images. Although it cannot be ruled out that phyllosilicates may be formed at higher temperatures in our experiments because the deformed samples were lost during recovery and, importantly,

a mixture of smectite and chlorite was present in the slip zones recovered from the experiments performed at T=300 and 400°C with the same but cylindrical rock (see Chapter. 3).

In fact, it has been confirmed from several aspects that the real area of contact increases over time when two surfaces are in quasi-stationary contact (Dieterich and Kilgore,1994; Im et al., 2018; 2019). For instance, the permeability across the contact surfaces decreases continuously during the hold, suggesting an increase in the contact area (Im et al., 2019). As a consequence, the decrease in $\Delta\mu$ and the transition of β from positive to negative cannot be fully explained by the change of the real area of contact. Alternatively, this may be controlled by changes in the strength of chemical bonding at the contact interface (Li et al., 2011). The negative β value observed after long t_h at high temperatures implies that thermally activated mechanisms counteract the healing processes and reduce the shear strength of the experimental fault. Our observations may suggest that the increase of the real area of contact ("contact quantity") and the decrease of the strength of the contact bonds ("contact quality") operate together, contributing to frictional healing. Although the formation or breaking of chemical bonds cannot be monitored in our experiments, we expect that time-dependent, thermally activated processes in asperity contact significantly impact frictional aging under hydrothermal conditions.

This hypothesis can be explained as follows (Figure 4.9). At relatively low-temperature conditions (e.g., T < 300°C), the contact area and formation of chemical bonds at the contact interface increase with the hold time, while the effect of bond breakage is negligible. As a consequence, $\Delta\mu$ increases log-linearly with t_h (Figures 4.5 and 4.6). The formation and breaking of chemical bonds are thermally activated processes. As the temperature increases, the formation of bonds is accelerated. At the same time, the strength of bonds decreases, promoting bond breakage. These two competing effects of temperature result in a nonmonotonic temperature and time dependence of healing (Ouyang et al., 2022; Li et al., 2018). In particular, during the short hold period, the

contact area increases due to compaction, providing more reaction sites available for bond formation. The number of new-formed bonds does not achieve saturation within this short hold. At the same time, the effect of bond breakage is insufficient to counteract the bond formation, leading to enhanced healing. Instead, when the hold duration exceeds a threshold time, the elastic interaction between neighboring bonds may results in the formation of new bonds to slow down over time. The number of newly formed bonds may achieve saturation within a long duration (Li et al., 2011; Liu et al., 2012). Bond breaking may become relatively more pronounced than bond formation, resulting in a decrease of $\Delta\mu$ with t_h. As a consequence, the decrease in $\Delta\mu$ and β values observed at high temperatures is the result of competing contributions of an increase in the contact area and a decrease in contact strength (Figure 4.9).

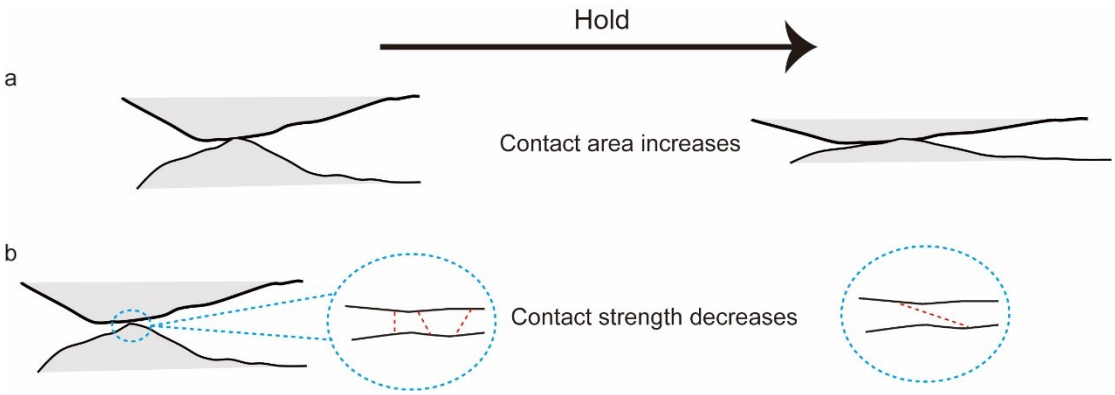

Figure 4.9: Schematic diagram showing the frictional healing process during the hold at $T \geq 200$°C and P_p=30 MPa. **a.** Contact area (or contact "quantity"). **b.** Contact strength (or contact "quality").

Bond breaking is facilitated by a hydrolysis reaction with water molecules under strained states (Michalske and Freiman, 1982; Zhu et al., 2005), providing a reasonable explanation for why the reduction of frictional healing with the hold time is easily observed in our pressurized fluids experiments than in dry experiments. The transition of β from positive to negative occurs more often in the 2nd sequence than in the 1st sequence. Based on the measurement of layer compaction (Appendices Figures 4.15d and 4.16d) and previous studies (Yasuhara and Marone, 2005), the increase in the contact area induced by compaction becomes relatively weaker in the 2nd sequence.

This may result in a more pronounced effect of reduced contact strength.

4.5.2 Geophysical implications

Our experimental observations indicate that under hydrothermal conditions frictional healing may saturate after time duration of the hold time, e.g., > 300 s and start to decrease with the hold time, which has significant implications for the seismic cycle. For instance, in enhanced geothermal systems where cold water is injected at depth into hot rocks, the diminished fault frictional healing with the hold time implies that the fault strength and the amount of elastic energy storage in wall rocks should decrease. If the other fault loading conditions remain constant, the decrease in the healing rate would result in an increased rate of earthquakes per unit time (Figure 4.10). In addition, the decrease in healing rate β observed can account for the change in the evolution effect (parameter b) in the rate and state friction law frame (or β scales as $b\ln t_h$) (Marone, 1998). This may cause an increase in the frictional stability parameter (a-b), which potentially results in the transition from velocity weakening (seismic) to velocity strengthening (aseismic) fault behavior in natural faults.

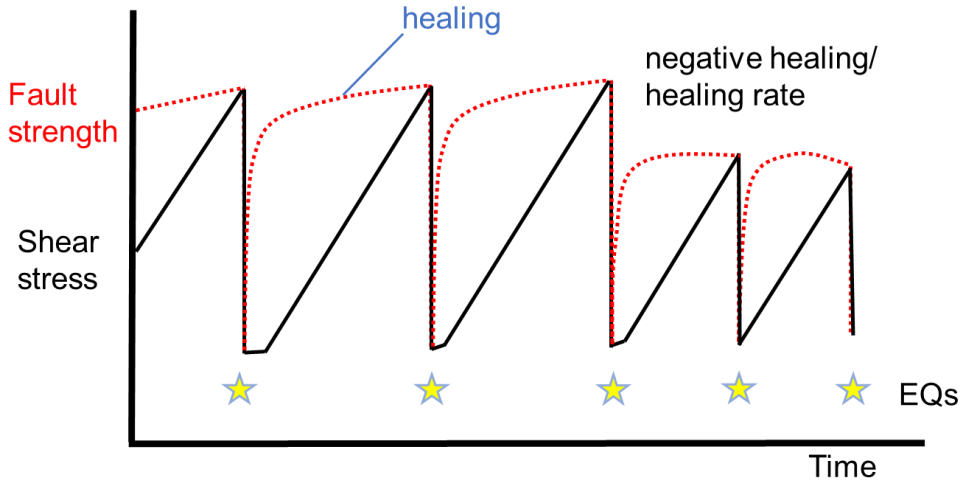

Figure 4.10: Diagram showing the evolution of fault strength and shear stress loading in a simplified seismic cycle. The negative healing rates often observed in the experiments performed under hydrothermal conditions may result, given the same fault loading rate, in an increase in the number of earthquakes per unit time.

4.6 Conclusions

In the present study, we perform SHS experiments on gabbro gouges under dry and P_p = 30 MPa conditions, at temperatures in the range of 25-400℃. We observe that the loglinear relation between frictional healing and the hold time, commonly observed in previous studies, is relaxed with increasing temperature and especially in the presence of pressurized hot water. Particularly, the healing rates switch from positive to negative with increasing hold time durations. This suggests that frictional healing is the result of multiple processes operating in competition: the increase of the real area of contact (or quantity of the contacts), which increases fault healing magnitude, and the decrease of the strength of the contact chemical bonds (or quality of the contacts), which counteracts frictional healing. Extrapolating our results to natural faults, if frictional healing and healing rates decrease with the hold period, the number of earthquakes per unit time is expected to increase, but decrease their magnitude.

4.7 Appendices

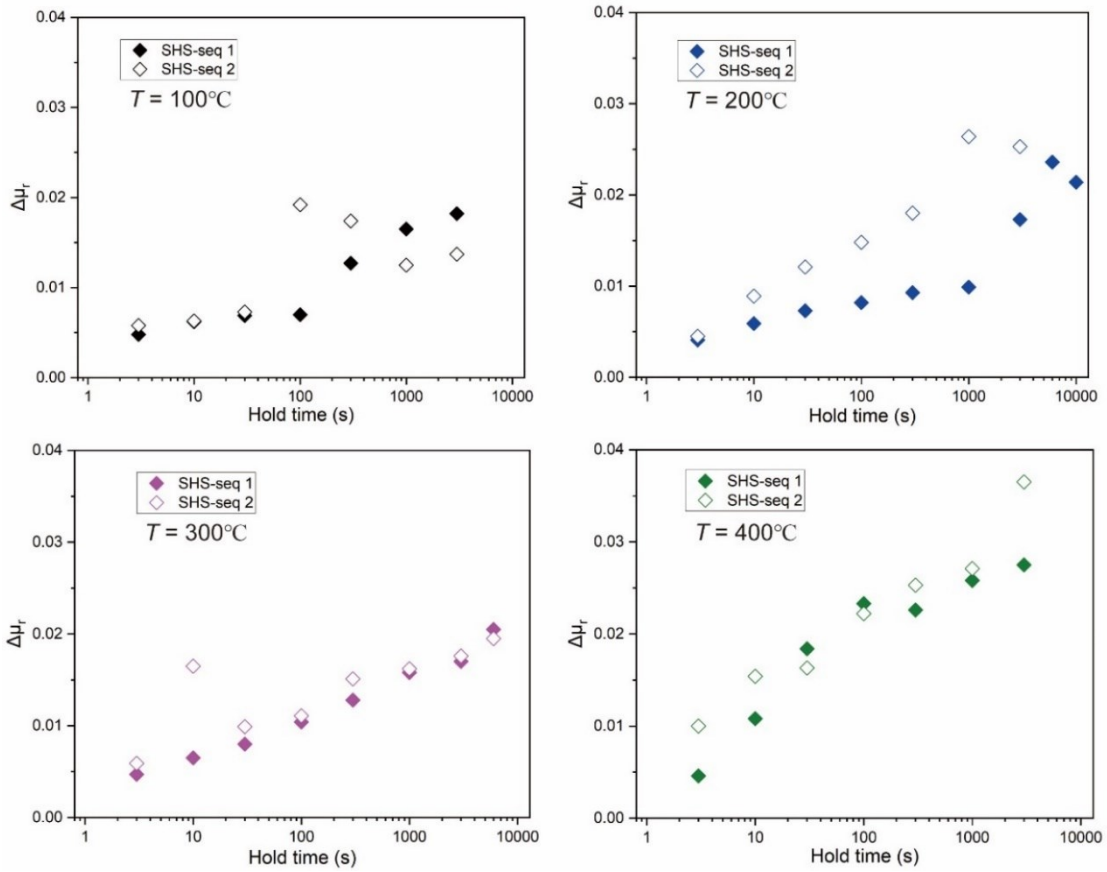

Figure 4.11: Dry conditions: frictional relaxation ($\Delta\mu_r$) versus the logarithm of hold time t_h. $\Delta\mu_r$ increases with $\log_{10}t_h$ independently of ambient temperature and SHS sequences. This trend is consistent with the one obtained at room temperature (Marone, 1998; Richardson and Marone, 1999).

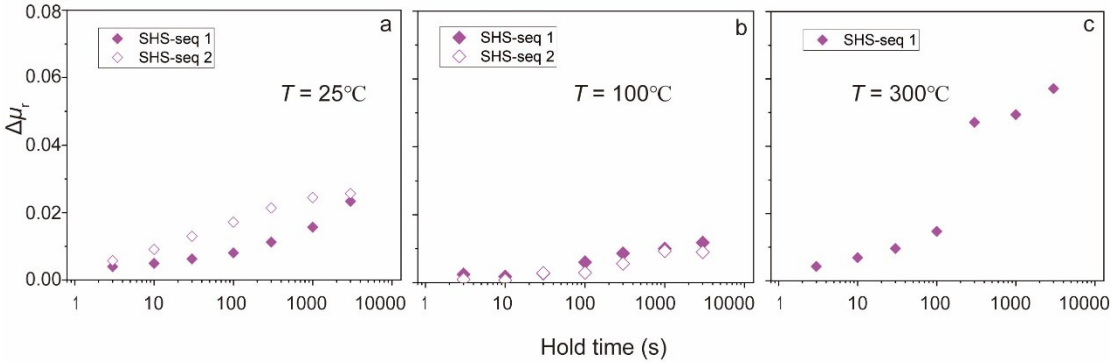

Figure 4.12: Frictional relaxation ($\Delta\mu_r$) versus hold time t_h at T =25°C, 100°C and 300°C (**a-c**). All

experiments performed at 30 MPa pore fluid pressure. Note that at $T \geq 200$°C, the relaxation $\Delta\mu_r$ during the hold is negligible, particularly in stick slip events.

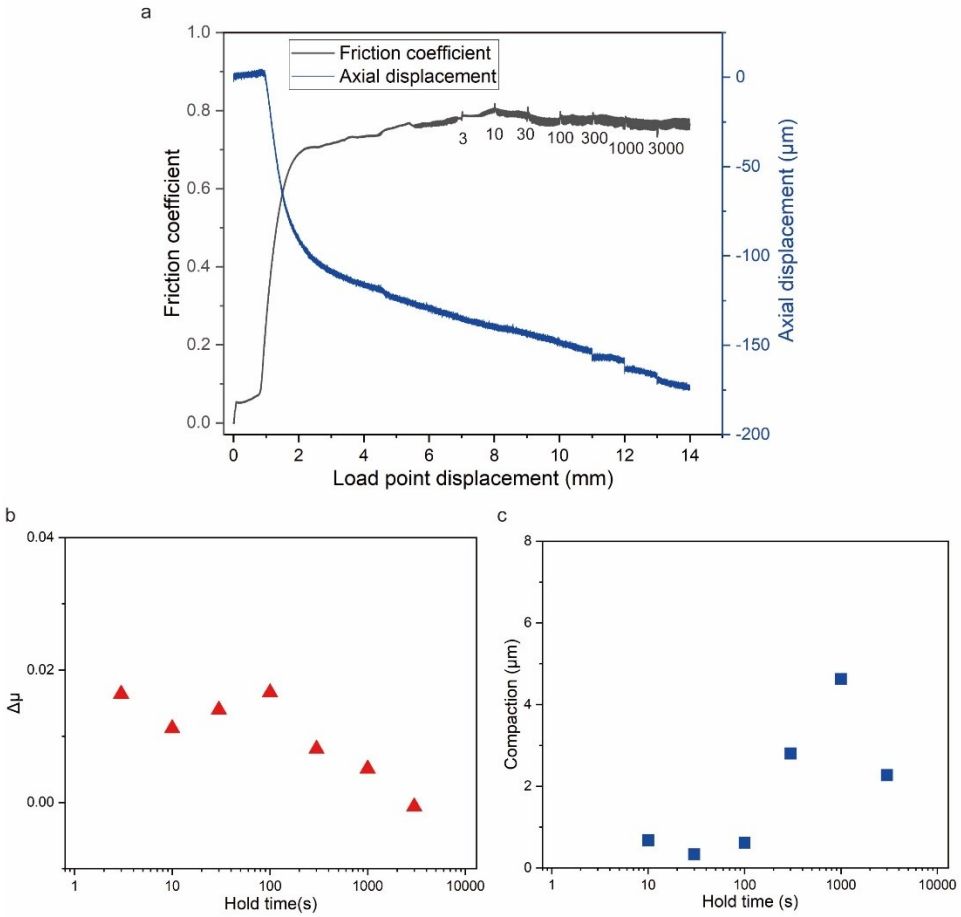

Figure 4.13: Mechanical data of the experiment (LHV2760) performed at T=200°C arrested after one SHS sequence (d = 14 mm). **a.** Evolution of the friction coefficient and axial displacement with slip displacement. **b.** healing data showing a slight decrease in $\Delta\mu$ with the hold time. **c.** Compaction data for each hold.

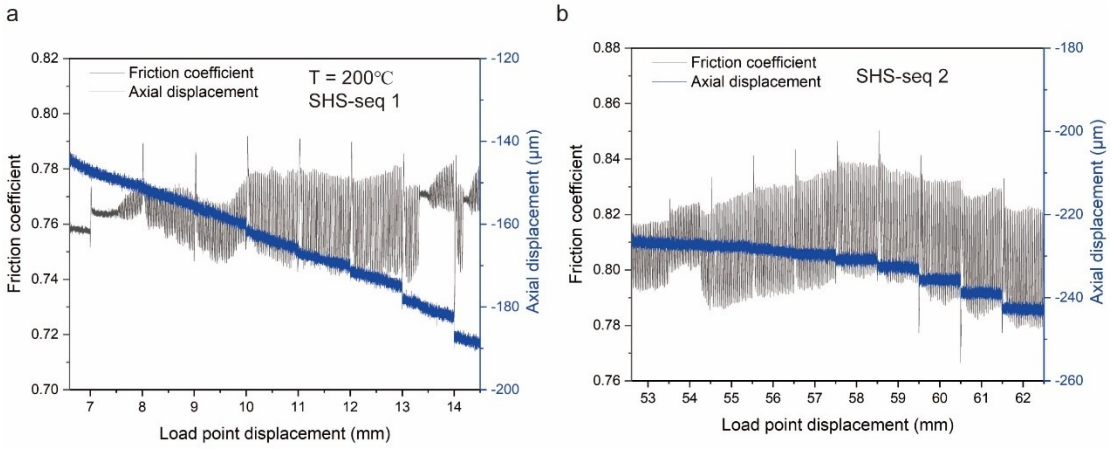

Figure 4.14: The evolution of friction coefficient and axial displacement with slip displacement for two SHS sequences (**a-b**) in the experiment performed at $T = 200$°C (LHV2760). In the 2nd sequence, the change in friction strength after each hold is observed.

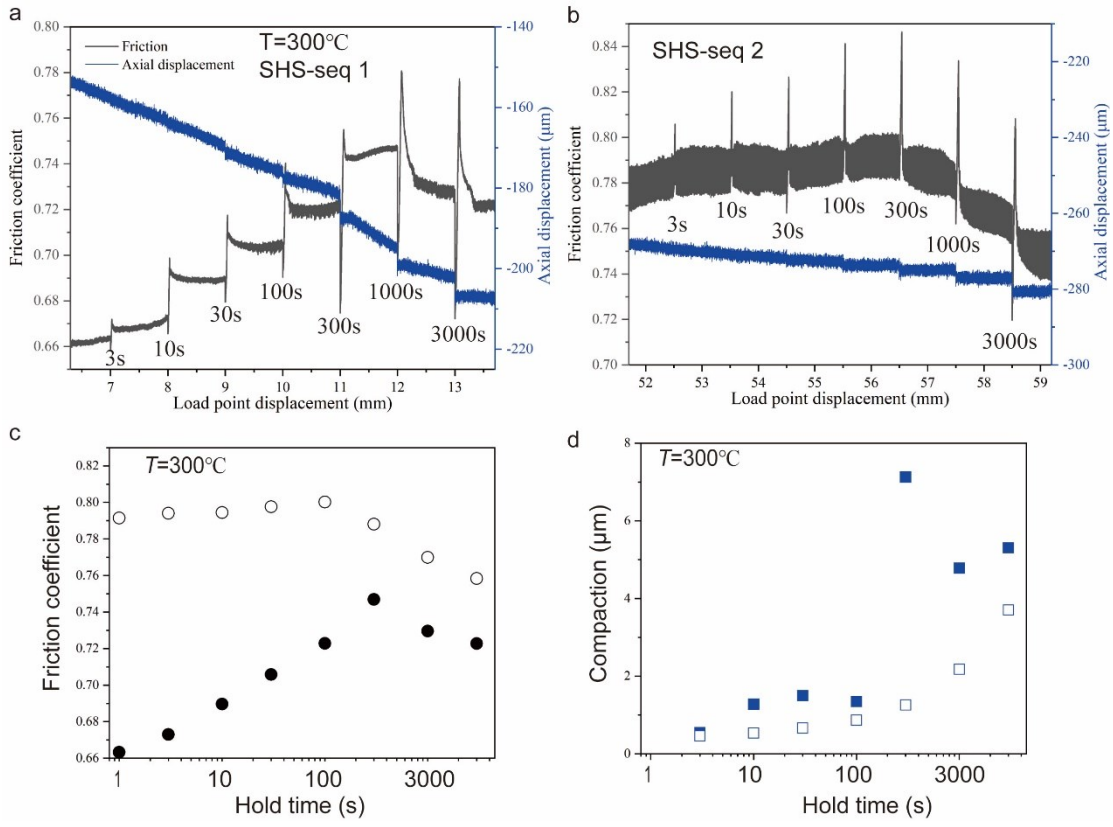

Figure 4.15: Results of the experiment LHV2755 performed at T = 300°C and P_p = 30 MPa**.** Friction coefficient μ and axial displacement versus slip displacement in SHS sequences (**a.** slip displacement from 7 to 13 mm; **b.** slip displacement from 52 to 59 mm). μ decreases (black in color line) and the gouge layer compacts (blue in color line) during holds. **c.** Steady state friction

coefficient after each hold. **d.** Gouge layer compaction during holds.

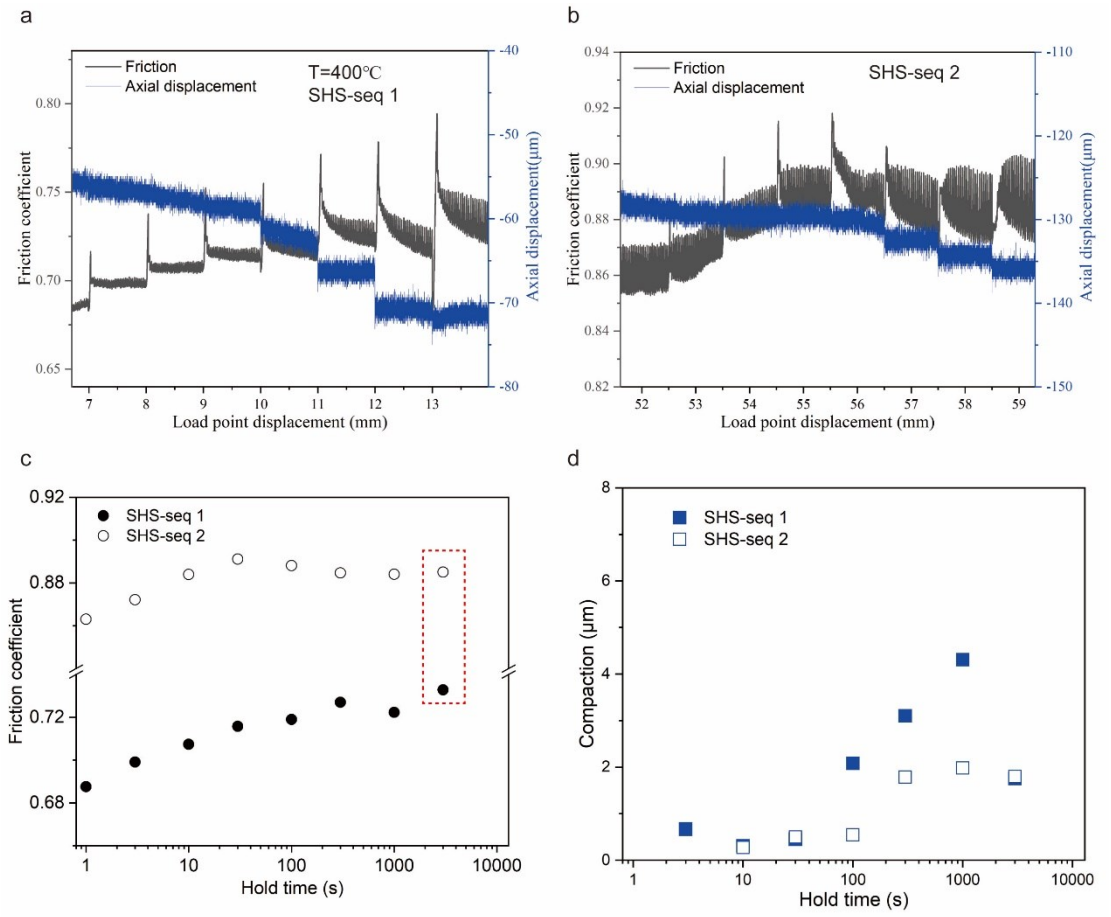

Figure 4.16: Mechanical data of the experiment (LHV2734) performed at $T = 400$°C. **a-b**. Evolution of friction coefficient and axial displacement with slip displacement for two SHS sequences. **c.** Post-hold frictional strength as a function of the hold time. Note that the friction coefficient determined after 3000 s holds is overestimated (marked by a square in red color) since the steady-state does not achieve within imposed slip displacement (1 mm). **d.** Gouge layer compaction during holds.

Chapter 5 Slip-dependence of frictional stability of simulated faults under hydrothermal conditions

Authors: Wei Feng[1,2], Lu Yao[2], Rodrigo Gomila[1], Shengli Ma[2] and Giulio Di Toro[1,3]

[1] Dipartimento di Geoscienze, Università degli Studi di Padova, Padua, Italy

[2]State Key Laboratory of Earthquake Dynamics, Institute of Geology, China Earthquake Administration, Beijing, China

[3]Sezione Roma 1, Istituto Nazionale di Geofisica e Vulcanologia, Rome, Italy

Status: to be submitted to *Geophysical research letters*

Contributions: W.F. and L.Y. conceived the study. W.F. and L.Y. performed the experiments. W.F. carried out the microstructural analysis with inputs from R.G. and G.D.T. W.F. wrote the first draft of the manuscript. All authors discussed and interpreted the results.

5.1 Abstract

The brittle to ductile transition (BDT) zone is thought to constrain the maximum depth for earthquake nucleation in the Earth's crust. The BDT broadly overlaps with the switch from upper crustal velocity weakening to lower crustal velocity strengthening behavior. In fact, velocity weakening is the necessary condition for earthquake nucleation. Here we report the frictional behavior of simulated faults made of basalt and gabbro gouges sheared at slip velocities ranging from 16 nm/s to 10 μm/s under ambient conditions close to BDT (50-100 MPa effective normal stress, 300-400°C temperature and 30 MPa pore fluid pressure). We observe cumulative slip (and duration of the experiment) facilitates the onset of the transition from velocity-weakening to velocity-strengthening behavior. In particular, with increasing slip displacement, frictional sliding and fluid-rock interaction result in the formation of smectite-type clays and in grain size reduction. These may contribute to lowering the required temperature and extending the slip velocity range for the occurrence of stability transition. Our results have important implications for understanding the seismogenic zone and may help explain the distribution of the aftershocks after large earthquakes.

5.2 Introduction

In the Earth's upper seismogenic crust, rocks generally deform in a "brittle" manner and the overall strength is dominated by pressure-sensitive fault friction (elastic-frictional regime *sensu* Sibson, 1977). Instead, in the lower, usually aseismic, crust, rocks deform in a "ductile" manner with increasing temperature and pressure, and the overall strength is constrained by temperature-sensitive creep and described by their appropriate flow laws (quasi plastic regime *sensu* Sibson, 1977; Evans and Kohlstedt, 1995). The transition between these regimes, also known as the brittle-ductile transition (BDT, Sibson, 1977; 1982), results in profound changes in rock rheological properties, occurring in a "semi-brittle" crustal domain where the deformation mechanisms

associated with the two regimes coexist (Meyer et al., 2019).

In the standard model of earthquake nucleation, the necessary condition is that the fault strength (or friction coefficient) decreases with increasing fault slip displacement *d* and slip velocity *V* (slip weakening and velocity weakening *V-W* behavior, Dietrich, 1978; Ruina, 1983; Ohnaka, 2013; Rice, 2006). The BDT, though does not correspond precisely to the transition from velocity weakening to velocity strengthening (*V-S*, friction coefficient increases with increasing *V*) frictional behaviors, is thought to constrain the lower limit of the seismogenic zone (Sibson, 1982; Scholz, 2019). Because of this, in the last fifty years, the BDT has been subject of intense geological, experimental and theoretical studies (Handy et al., 2007; Stipp et al., 2002; Asanuma et al., 2012; Tse and Rice, 1986; Shimamoto and Noda, 2014).

The dependence of fault friction with *V* is described by the empirically based rate and state friction (RSF) law (Dieterich, 1979; Ruina, 1983; Marone, 1998). Because earthquakes in the upper crust nucleate often in the presence of hot and pressurized fluids, a number of experimental studies have been conducted on crustal rocks (e.g., gabbro, granite, limestone, halite and quartz- or phyllosilicate-rich rocks) under "hydrothermal conditions" (Shimamoto, 1986; Blanpied et al., 1991; den Hartog et al., 2012; Okuda et al., 2023; He et al., 2007; Nakatani and Scholz, 2004). The velocity-stepping (*V*-stepping) experiments (i.e., the slip velocity is increased or decreased abruptly during sliding to measure the response of the dynamic friction coefficient) reveal the presence of three domains with increasing ambient temperature (hence, depth). They include a low temperature *V-S* domain, an intermediate temperature *V-W* domain and a high temperature *V-S* domain (Verberne et al., 2015; Chen et al., 2020; Blanpied et al., 1991; He et al., 2007; Zhang and He, 2016; Zhang et al., 2017; den Hartog et al., 2012; Okuda et al., 2023). In particular, the transition from intermediate temperature *V-W* to high temperature *V-S* domain corresponds roughly to the onset of BDT (Chen et al., 2020; Zhang and He, 2016). It has been shown that the BDT is dependent on temperature, pressure, presence of fluids, strain rate and lithology (Sibson,

1982, 1984; Scholz, 2019). However, because of technical limitations, the slip displacement was limited to few mm (e.g., Blanpied et al., 1991) or the role of fault slip displacement was not investigated for this transition, although its influence on frictional healing and fault stability has been recognized (Beeler et al., 1996; Richardson and Marone, 1999; Noel et al., 2023).

In this study, we perform rock friction experiments on simulated gabbro and basalt gouges. We impose *V*-steps at slip velocities ranging from 16 nm/s to 10 μm/s at temperatures *T* of 300 and 400°C, pore fluid pressure P_p of 30 MPa and effective normal stresses σ_{eff} of 50 and 100 MPa. The goal is to investigate whether the cumulative slip displacement affects the frictional stability transition and onset of BDT. Our mechanical data indicate that instability (*V*-*W*) transitions to stability (*V*-*S*) with increasing fault slip displacement. Microstructure observations suggest that this transition is associated with transition from localized deformation ("brittle") to bulk deformation ("ductile", Rutter, 1986). This result has important implications for understanding fault frictional stability and may link to the distribution of aftershocks following the mainshocks.

5.3 Methods

5.3.1 Starting materials

The rocks used in the experiments are the "Jinan dark green" gabbro (China) and the Etna volcano basalt (Italy, Giacomel et al., 2021). The intact rock bulks were crushed in a mill and sieved with a 180-mesh to obtain powders with grain size of less than 88 μm for the experiments. The basalt consisted of feldspar, augite, olivine, magnetite, and minor amounts of amorphous minerals (XRD analysis, see Giacomel et al., 2021), and the gabbro consisted of feldspar, pyroxene, olivine, and biotite. The mineral composition of the two rocks is reported in Tables 2.1 and 2.2 (Chapter 2).

5.3.2 Friction experiments

5.3.2.1 Apparatus

Friction experiments are performed with a Low to High-Velocity rotary shear apparatus (LHVR-Beijing) installed at the Institute of Geology, China Earthquake Administration in Beijing, China (Ma et al., 2014) (Figure 5.1). The key improvement of this apparatus is the installation of a newly-conceived hydrothermal pressure vessel capable of providing temperature (T) up to 500°C and pore pressure (P_p) up to 70 MPa. After obtaining vacuum in the vessel, pore fluid (distilled water) is injected into the vessel from the upper gland with a syringe pump. The fluid pressure is maintained constant (drained condition) and measured with a digital sensor. The sample and pore fluids are heated with an external furnace. The temperature inside the vessel is measured with a thermocouple located approximately 1 mm below the gouge layer. An updated air actuator is used to apply a normal load up to 60 KN (~250 MPa normal stress on the sample), measured with a 100 kN cell. To increase the quality of the mechanical data, the torque bar is installed just beneath the vessel and rigidly connected to the lower axial column (7 in Figure 5.1). The shear torque is measured with two high-resolution torque gauges. A pressure compensating device is installed in the lower loading part coupled to the axial column (8 in Figure 5.1) to reduce the influence of pore pressure variations on effective normal stress. Angular rotations are measured with an optical encoder (3 in Figure 5.1) installed next to the rotary column. Axial displacement (w) (dilatation or compaction of the gouge layer and machine) is measured with a linear voltage differential transducer (LVDT) (1 μm resolution and 10 mm stroke) placed on the bottom part of the machine (10 in Figure 5.1). To improve the stiffness of the machine, 22 mm in diameter pistons are used in these experiments. Data are acquired at a frequency of 50 Hz for all experiments.

The gouges are sandwiched between two ring-shaped and surface-grooved pistons (22/28 mm in inner/outer diameter) and confined laterally by inner and outer metal rings to avoid the gouge extrusion during compaction and shearing. The grooves are 0.25 mm in height, 0.5 mm in width, and spaced 1 mm a-part to ensure that shearing occurs within the gouge layer not at the gouge-metal holder boundary. To eliminate the

spurious torque of the vessel, confining rings and O-rings are lubricated with Molykote D-321R antifriction coating and with HT-resistant grease, respectively. The fault friction coefficients reported here are not corrected for the friction of the vessel.

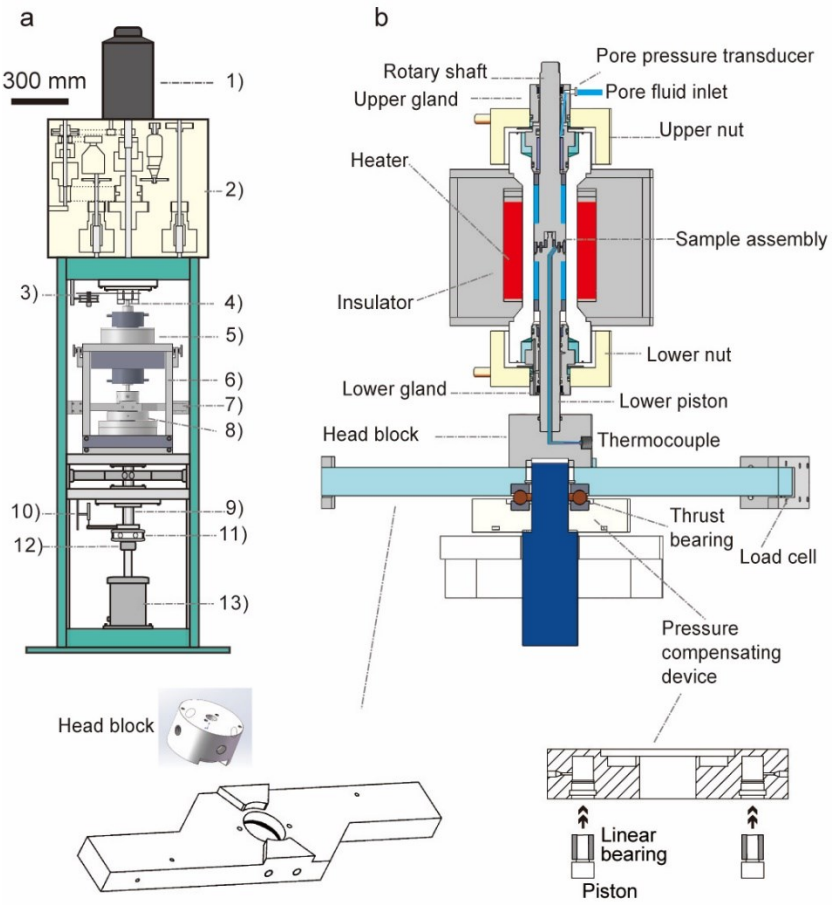

Figure 5.1: Experimental setup. a. The Low to High velocity rotary shear apparatus, equipped with a dedicated hydrothermal vessel (modified from Ma et al., 2014). 1) servomotor, 2) gear and belt system, 3) rotary encoder and potentiometer, 4) rotary column, 5) hydrothermal pressure vessel, 6) metal frame, 7) cantilever-type torque gauge, 8) pressure compensating device (designed by Lu Yao), 9) axial loading column, 10) liner voltage displacement transducer (LVDT), 11) thrust bearing, 12) compression cell, 13) air actuator. Note that when the new torque measurement unit 7) was used, the old one connected to the lower loading column (8) in Figure 2.1) did not support any shear torque. **b.** The sketch of the hydrothermal vessel with the main parts indicated in the diagram.

5.3.2.2 Experimental procedure

A total of 11 experiments are conducted at constant σ_{eff} of 50 MPa or 100 MPa, P_p of 30 MPa and T of 300°C or 400°C (Table 5.1 for full list). In setting up each experiment, about 0.8 g of gouge powder is distributed evenly into the sample holder, yielding an initial gouge thickness of 1.5 mm.

The gouge assembly is then mounted to the vessel. In each experiment, after achieving the desired and stable conditions (σ_{eff}, P_p and T), the initial "*run-in*" stage is imposed at a slip velocity of 10 μm/s for 7 mm of slip displacement (d). Once a stable friction coefficient ($\mu = \tau / \sigma_{eff}$) is achieved, a series of V-steps are applied by switching the load-point velocities over 5-folds in magnitude from 16 nm/s to 10 μm/s. The slip displacement between each V-step varies from 0.5 mm to 20 mm, depending on the slip displacement (D_c) required to reach a new steady state friction value. For the experiments on gabbro gouges, the temperature is set to T = 400°C and one experiment performed at σ_{eff} = 100 MPa (LHV2710), because preliminary experiments showed that the *V-S* behavior was not achieved at T = 300°C. To study the dependence of frictional stabilities with slip displacement, two cycles of V-stepping tests separated by a slip displacement of, for instance, 15 mm for LHV2710 and 40 mm for LHV2588. An additional experiment is performed on basalt gouges with σ_{eff} increased from 50 MPa to 100 MPa to investigate the pressure-dependence, if any, of μ in the *V-S* regime. The σ_{eff} steps are achieved by changing the normal load without stopping the drive motor during this process and thus without relaxing the imposed shear torque to the sample. Five experiments are performed at constant V= 0.4 μm/s (LHV2580) or with a limited number of V-steps (LHV2585, 2589 and 2727 for basalt gouges, and LHV2609 for gabbro gouges) for $7 < d < 12$ mm to investigate the microstructural evolution of the gouge layer with slip displacement and its relation to the measured V-dependence. In this study we focused on the V-dependence only qualitatively and, did not determine the RSF law parameter (a-b).

Table 5.1: List of experiments and experimental conditions

Exp.	Rock	P_p [MPa]	σ_{eff} [MPa]	T [°C]	V [μm/s]	d [mm]
2578	basalt	30	50	300	10-2-0.4-2-0.4-0.08-0.016-0.08-0.4-1-2-5-10	72
2580	basalt	30	50	300	0.4	29
2583	basalt	30	50	300	10-2-0.4-0.08-0.016-0.08-0.4-2-10	46
2585	basalt	30	50	400	10-2-0.4	12
2586	basalt	30	50	400	10-2-0.4-0.08-0.016-0.08-0.4-2-10-2-0.4	28
2589	basalt	30	50	300	10-2-0.4-2-0.4-2-0.4-2-10	7
2608	basalt	30	50-100	400	10-2-0.4	37
2727	basalt	30	50	400	10-2	7
2588	gabbro	30	50	400	10-2-0.4-0.08-0.016	12
					2-0.4-0.08-0.016-0.08-0.4-2-10-2-0.4	60-72
2609	gabbro	30	50	400	10-2-0.4	7
2710	gabbro	30	100	400	10-2-0.4-0.08-0.016	7
					2-0.4-0.08-0.016-0.08-0.4-2-10	22-32

P_p = pore fluid pressure, σ_{eff} = effective normal stress, T = temperature, V = slip velocity, d = slip displacement.

5.3.3 Microstructural analysis

At the end of the experiments, the vessel is cooled down maintaining the same pore pressure as in the experiments to avoid the vaporization of the pore water that would damage the microstructures. Unfortunately, the gouge layers from experiments (LHV2578 and 2586) are not successfully recovered. The recovered samples are impregnated with epoxy resin to obtain polished thin sections cut perpendicular to the

slip surface and parallel to the shear direction (i.e., tangential to the circumference of the sample) for Scanning Electron Microscope (SEM) investigations. Backscatter electron images (BSE) are acquired with a Tescan Solaris Field-Emission SEM operating at an accelerating voltage of 5 Kev and a current of 300 pA at a working distance of 3 or 4 mm. In addition, representative samples are analyzed with X-Ray diffraction (XRD) to determine the mineral compositions of the deformed samples.

5.4 Results

5.4.1 Mechanical Data

In both basalt and gabbro-built gouges, the friction coefficient and its velocity dependence evolve with slip displacement (Figure 5.2). The basalt-built gouges when sheared at 300°C and σ_{eff} = 50 MPa (LHV2578), during the *run in* stage at 10 μm/s and once the static friction coefficient (μ_s) of 0.67 is overcome, have stick-slip behavior (Figure 5.2a). *V*-steps (e.g., from 10 to 2 and to 0.4 μm/s) show that the gouge is velocity weakening. With increasing slip displacement, the magnitude of the friction drop during stick-slip events at 0.4 μm/s gradually reduces and after *d* ~20 mm the fault creeps (Inset I). At this stage and for the rest of the *V*-steps, the fault frictional behavior is velocity strengthening (see *V*-step from 0.4 to 2 μm/s at *d* ~25 mm) and μ can be as low as 0.5. Experiment (LHV2583) performed at identical deformation conditions produced similar results (See Appendices Figure 5.7). Instead, when sheared at *T* = 400°C and σ_{eff} = 50 MPa (LHV2586), once μ_s is overcome, the fault creeps at *V*=10 μm/s and a steady state friction μ_{ss} ~0.63 is achieved. When *V* is stepped to 2 μm/s, the fault stick slips and shows velocity weakening behavior. Similar to the experiment LHV2578 performed at *T* =300°C, the magnitude of the friction drop during stick-slip events gradually reduces and after *d* ~8.5 mm the fault creeps (Inset II). At this stage and for the rest of *V*-steps, the fault shows velocity strengthening behavior (see *V*-step from 2 to 0.4 μm/s at *d* ~9 mm) and μ can be as low as 0.4 (Figure 5.2b). The two experiments on basalt gouge show that under these hydrothermal conditions less displacement is

required to stabilize frictional sliding with increasing T.

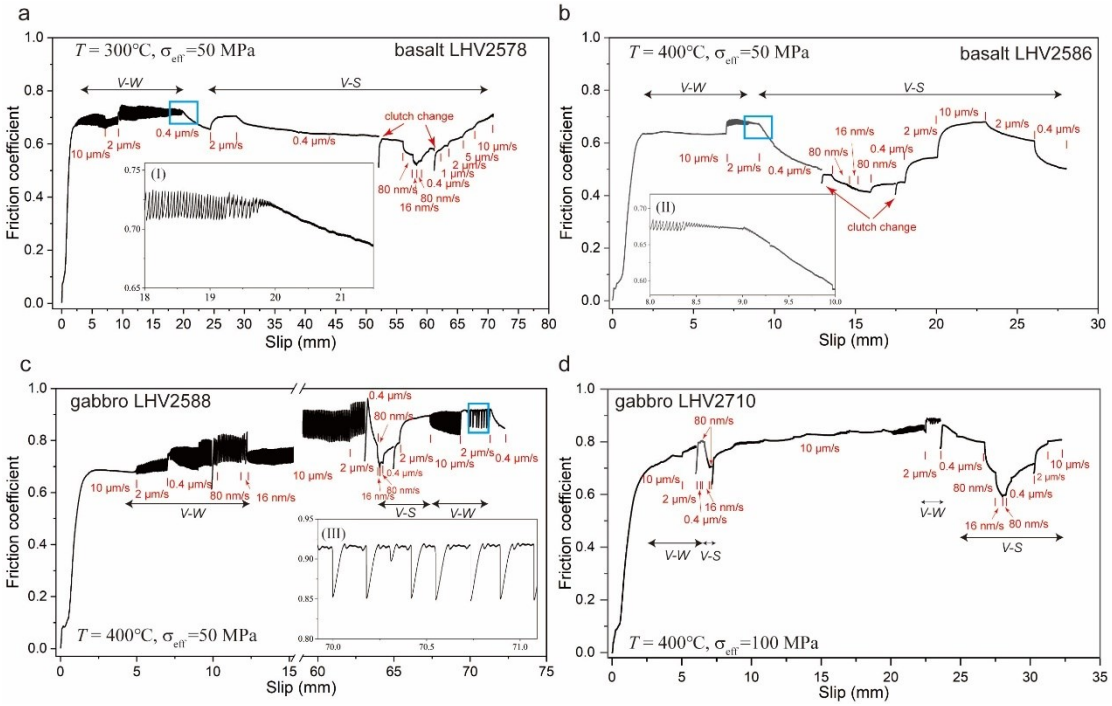

Figure 5.2: Evolution of the friction coefficient μ versus slip displacement (d) for experiments performed at P_p = 30 MPa under hydrothermal conditions. The experimental conditions (T, σ_{eff} and V-steps) are reported in each diagram. **a.** Experiment LHV2578 performed at T = 300°C and σ_{eff} = 50 MPa on basalt-built gouge. Inset I shows the progressive evolution with slip from unstable sliding to creep at V= 0.4 µm/s. **b.** Experiment LHV2586 performed at T = 400°C and σ_{eff} = 50 MPa on basalt-built gouge. Inset II shows a close-up of the V-stepping (2-0.4 µm/s), exhibiting V-S behavior. **c.** Experiment LHV2588 performed at T = 400°C and σ_{eff} = 50 MPa on gabbro-built gouge. Inset III shows the emergence of period-multiplying cycle behavior in the transitional regime. **d.** Experiment LHV2710 performed at T = 400°C and σ_{eff} = 100 MPa on gabbro-built gouge.

The frictional behavior of gabbro-built gouges is more complex and unstable than the one of basalt-built gouges at the same deformation conditions (Figures 5.2c-d). At T = 400°C and σ_{eff} = 50 MPa (experiment LHV2588), during the *run in* at V = 10 µm/s, the fault has μ_{ss} ~0.68. After 5 mm of slip when V is stepped to 2 µm/s, stick-slip and V-W behavior are observed (see V-steps in the first 15 mm of slip) with an exception of V-step to 16 nm/s (Figure 5.2c). After imposing 40 mm of slip displacement at V=10 µm/s

(time duration 4000 s), stick-slip and *V-W* behavior are still observed at 10 and 2 μm/s. However, frictional behavior becomes *V-S* when *V* is stepped in the range of 16 nm/s to 2 μm/s (μ decreases when *V* is decreased from 0.4 μm/s to 80 or 16 nm/s and then increases when *V* is increased from 16 nm/s to 2 μm/s). Period-multiplying cycle behavior (Mei et al., 2021) is observed at $V = 2$ μm/s in the transitional regime (Inset III). Instead, at $T = 400$°C and $\sigma_{eff} = 100$ MPa, after the *run in* stage, the fault shows *V-W* behavior for *V* range of 10 μm/s to 80 nm/s and *V-S* behavior for 80 nm/s to 16 nm/s (Figure 5.2d). Then, after 15 mm of slip at $V = 10$ μm/s, the gouge-built gouges exhibit stick-slip and *V-W* behavior at 2 μm/s (see $d \sim 23$ mm). *V-S* behavior is observed for larger slip displacement ($25 < d < 32$ mm) and lower *V*. Intriguingly, the *V* range for *V-S* behavior is extended to 10 μm/s at the end of the experiment (Figure 5.2d).

Summarizing, experimental faults made of basalt-built gouges, under the investigated hydrothermal conditions and with respect to those made of gabbro-built gouges, show (1) evident transitions from *V-W* to *V-S* frictional behavior with increasing slip displacement and, (2) ductile-like deformation process partially involved in the *V-S* regime. Point 1 is further attested by experiment LHV2580 performed with basalt-built gouges sheared at the same ambient conditions of the experiment LHV2578 ($T = 300$°C and $\sigma_{eff} = 50$ MPa) but at constant $V = 0.4$ μm/s. Stick-slip behavior gradually disappears with slip displacement (Figure 5.3a). Point 2, in particular the pressure-dependence of shear stress with normal stress, has been investigated in the experiment LHV2608 performed with a step σ_{eff} increase from 50 MPa to 100 MPa during the *V-S* regime at $V = 0.4$ μm/s. The doubling of the σ_{eff} results in an increase in shear stress from 38 to 64 MPa which corresponds to friction coefficients of 0.76 to 0.64 at the steady state (Figures 5.3b-c). This pressure-sensitive friction value suggests that the viscous-plastic deformation mechanism may partially take place in the *V-S* stage. The pressure dependence of μ is reversible where the friction coefficient increases back to 0.76 once the normal stress is reset to 50 MPa (Figure 5.3b).

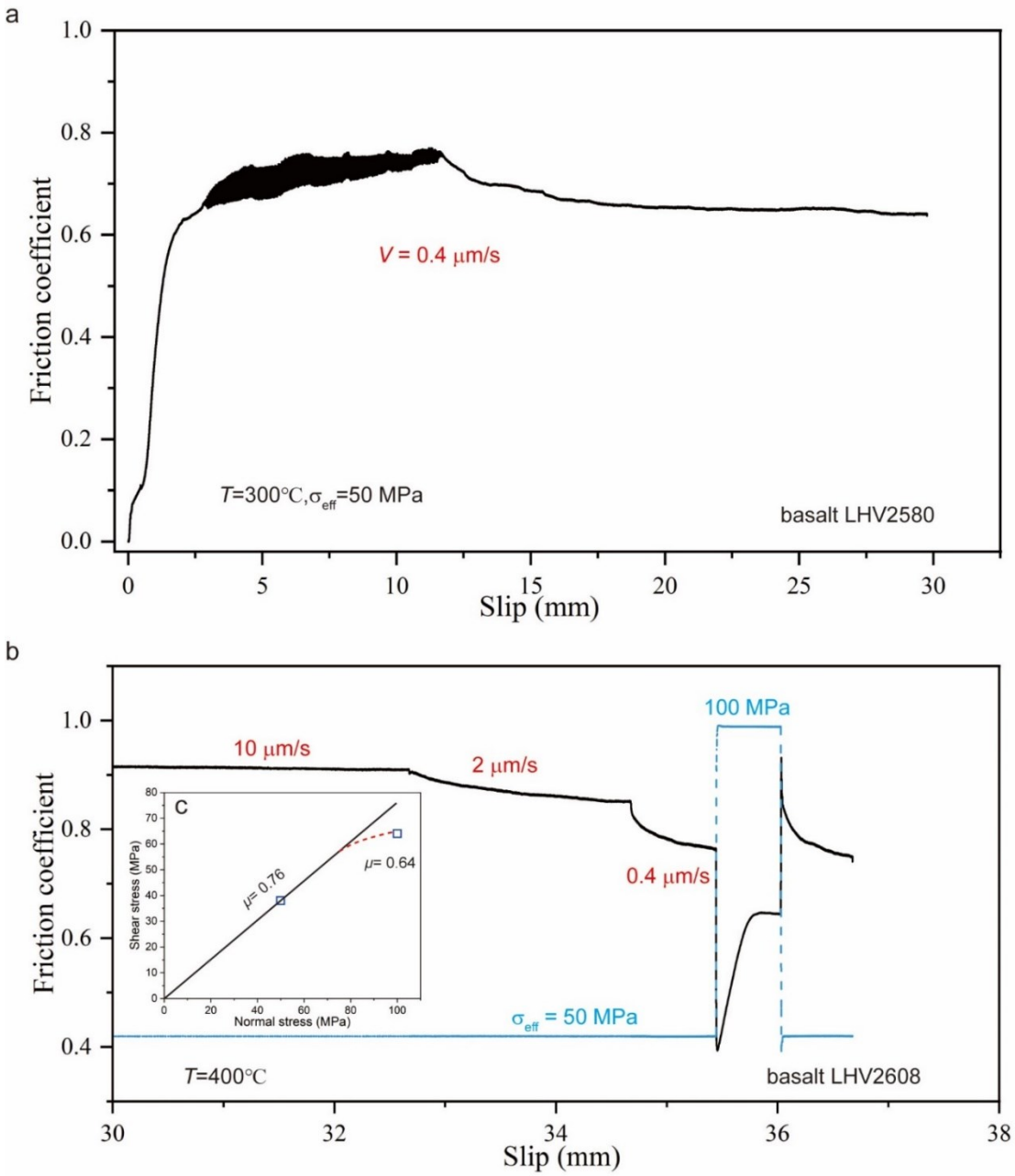

Figure 5.3: Results from experiments on basalt-built gouges (experimental conditions indicated in the diagram). **a.** Experiment LHV2580 performed at 300°C and σ_{eff} = 50 MPa at constant V of 0.4 μm/s. **b.** Experiment LHV2608 performed at 400°C including an increase of σ_{eff} from 50 MPa to 100 MPa. Blue in color curve = effective normal stress. **c.** Shear stress values collected at 50 MPa and 100 MPa normal stress in the Mohr space.

5.4.2 Microanalysis of deformed samples

5.4.2.1 Mineral assemblage

Both basalt-built and gabbro-built gouges which exhibit creep or *V-S* behavior (LHV2578, 2580 and 2588) show a broad peak at $2\theta \sim 8°$ in the XRD spectra, which is absent in the starting materials and the samples exhibiting stick-slip behavior (LHV2589) (Figure 5.4 and mechanical data see Appendices Figure 5.8). The intensity of the 8° peak increases with slip displacement (and thus the duration) of the experiment (LHV2580, d ~ 29 mm and LHV2578, d ~72 mm). After separation of the ultra-fine grains, orientation and glycol treatment, the newly formed mineral is identified as smectite (Brindley and Brown, 1980) (See Appendices Figure 5.9). In addition, a decrease in the intensity of the biotite peak $2\theta \sim 10°$ is measured in the sheared gabbro gouges (LHV2588) with respect to the starting materials. Frictional sliding under the investigated hydrothermal conditions results in the appearance of new water-bearing minerals (smectite).

5.4.2.2 Microstructures

The microstructures associated with velocity weakening and velocity strengthening behavior were investigated by arresting the experiments and recovering the sheared gouge layer at increasing displacement and in different regions.

In basalt-built gouges sheared for $d = 7$ mm at $T = 300$°C and $\sigma_{eff} = 50$ MPa (LHV2589), a principal shear band is hardly recognized. Possibly the slip zone was lost during the recovery of the gouge layer or thin section preparation (Figure 5.5a). With increasing slip displacement (LHV2583, $d = 46$ mm), when the experiment is arrested in the *V-S* regime, two slip zones about ~ 300 μm-thick are recognizable in the top and bottom part of the gouge layer (Figure 5.5b). The upper slip zone is made of ultra-fine grains (down to 200 nm in size, Figures 5.5c-d) resulting from fragmentation of the starting material. The pores between the grains are partially filled by < 100 nm long acicular grains possibly made of newly formed smectite (red arrows in Figure 5.5d). Riedel R1 shears depart from the slip zones and are oriented consistently with the dextral sense of shear (Figure 5.5b). Part of the grain boundary becomes blurred, suggesting a sintering

process or likely liquid-assisted processes (Figure 5.5d). In the sample LHV2580 sheared at a constant V of 0.4 μm/s for d = 29 mm, a ~80 μm-thick slip zone is developed in the upper part of the gouge layer (Figures 5.5e). The slip zone matrix is made by an aggregate of ultra-fine, often rounded grains immersed in a matrix which includes also < 100 nm long acicular grains possibly made of newly formed clays and an amorphous-like uniform dark grey in color matrix (inset in Figure 5.5f). Riedel R1 shears depart from the slip zone and are oriented consistently with the dextral sense of shear (Figures 5.5e-f).

In gabbro-built gouges sheared at T = 400°C and σ_{eff} = 50 MPa but stopped during stick-slip and *V-W* behavior in the initial stage of slip (d = 7 mm, LHV2609 see Appendices Figure 5.10). Strain deformation is localized into ~80 μm-thick slip zones (marked by dashed line in Figure 5.6a). The slip zone is made of ultra-comminuted grains of feldspar and clinopyroxene with sharp edges (Figure 5.6b). Riedel R1 shears depart from the slip zone and cut across the gouge layer, consistently with the sinistral sense of shear imposed on the sample (Figure 5.6a). With increasing slip displacement (d = 72 mm, LHV2588), once the gouge layer underwent several *V-W* and *V-S* transitions (Figure 5.2c), the gouge layer is intensely comminuted (Figures 5.6c-d). Grain size reduction is larger in the upper ~ 600 μm-thick and lower ~300 μm-thick gouge layers and interpreted as the main slip zones. Three domains are recognizable from the top to the central part. Domain 1 is characterized by intense fragmentation, with sub-angular to rounded grains of pyroxene (larger grains) and feldspar (small grains) and low porosity (Figure 5.6d). The matrix includes up to 1 μm long acicular in shape grains interpreted as newly-formed smectite (red arrows, inset in Figure 5.6d). Grain size increases toward the inner part of gouge layer (domains 2 and 3). The domain 2 is more porous than domain 1, and domain 3 is cut by Riedel R1 shears departing from domain 1 (Figure 5.6c). For gabbro-built gouges sheared at T = 400°C but higher σ_{eff} (100 MPa, LHV2710), after d = 32 mm, the gouge layer is intensely comminuted compared to the one at 50 MPa σ_{eff}. Deformation is distributed over the entire gouge layer thickness and

a sinistral S-C fabric, outlined by the spatial arrangement of pyroxene and feldspar grains, is well-developed (Figures 5.6e-f). Grains have sharp edges and angular shapes, indicative of cataclastic flow.

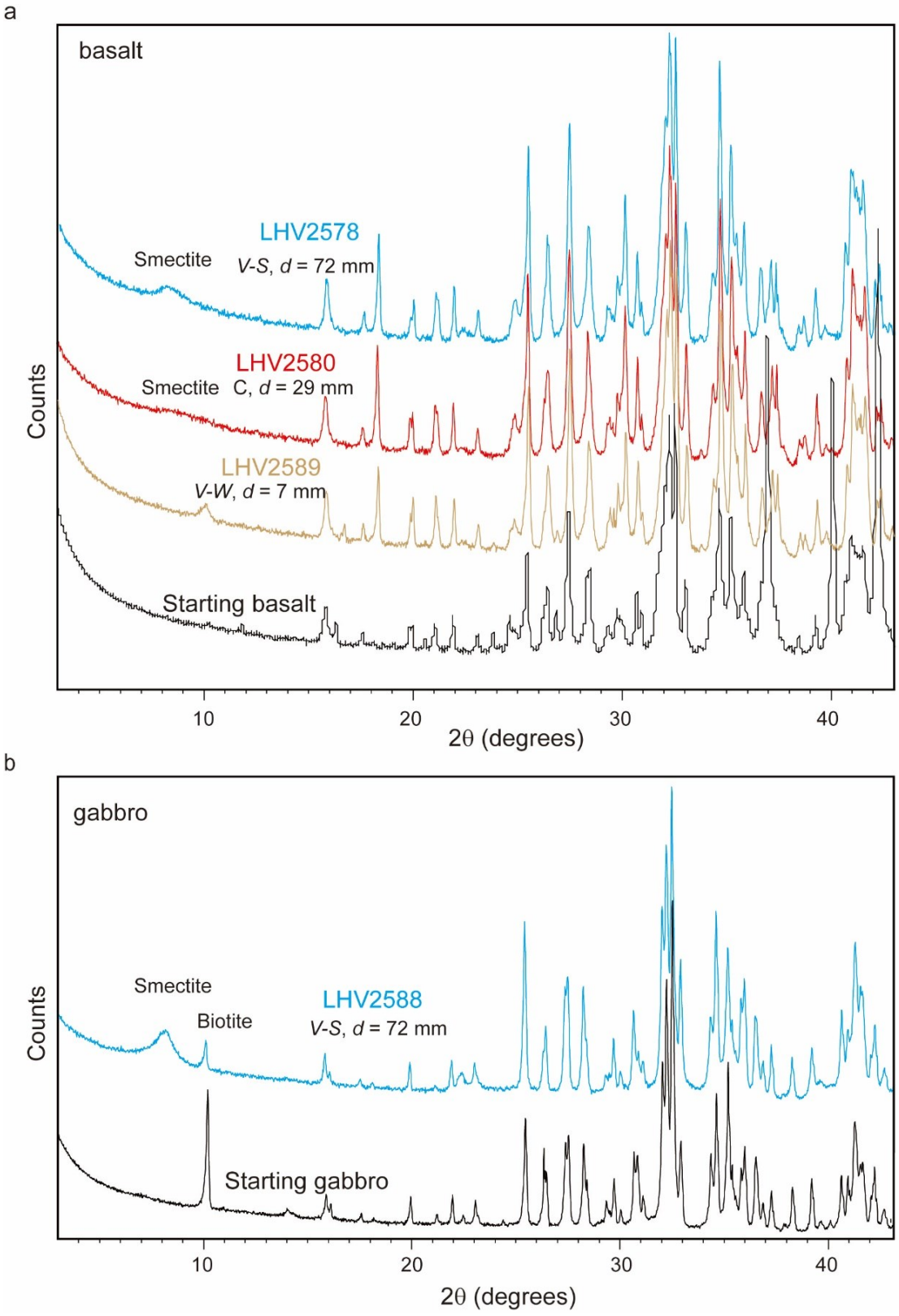

Figure 5.4: X-ray diffraction (XRD) spectra of representative samples recovered from friction experiments (the number of the experiments, slip displacement *d* and frictional behavior are reported in each diagram. *V-S* = velocity strengthening; *V-W* = velocity weakening; C = creep). The

appearance of the peak at 2θ~8° in the sheared gouges is indicative of the presence of newly-formed smectite-type clays **a.** XRD spectra from basalt-built gouge. **b.** XRD spectra from gabbro.

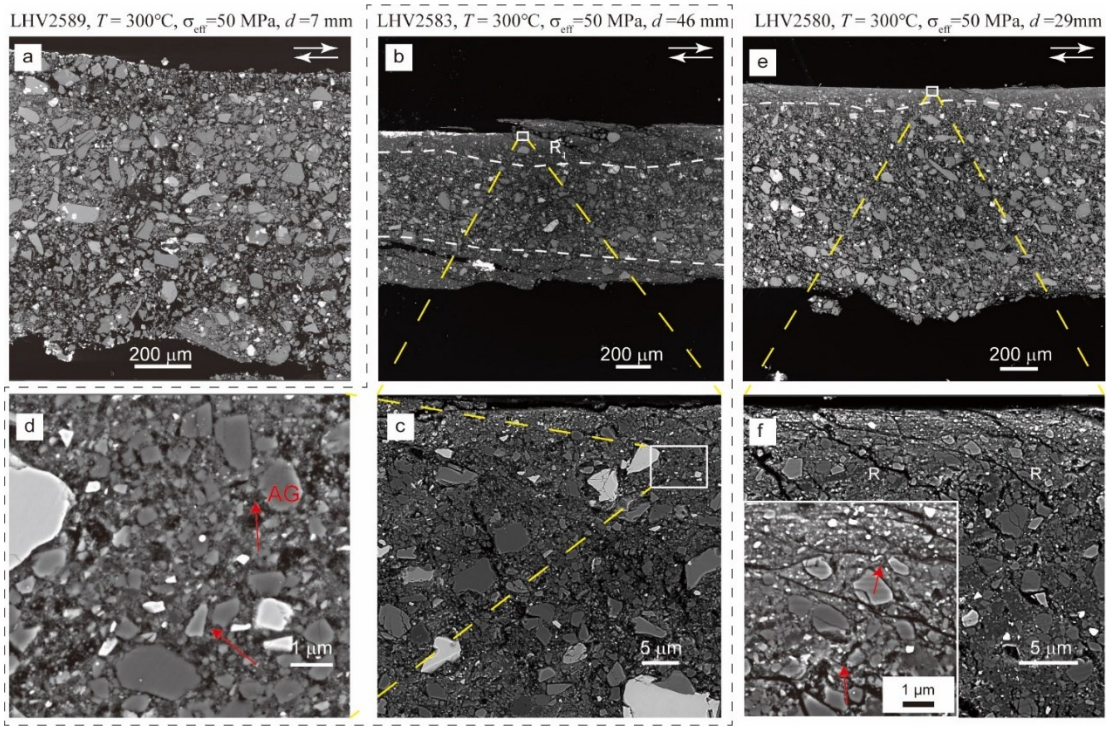

Figure 5.5: Microstructures of sheared basalt gouge layers from three experiments at T= 300°C and σ_{eff}= 50 MPa stopped at different displacements. Experimental conditions are reported in the top images. **a.** LHV2589: d = 7 mm. **b-c-d.** LHV2583: d = 46 mm. Red arrows in d indicate the acicular grains interpreted as newly-formed smectite. **e-f.** LHV2580: d = 29 mm. Red arrows in the inset of "f" indicate acicular grains and amorphous-like materials. See text for description. AG = acicular grains.

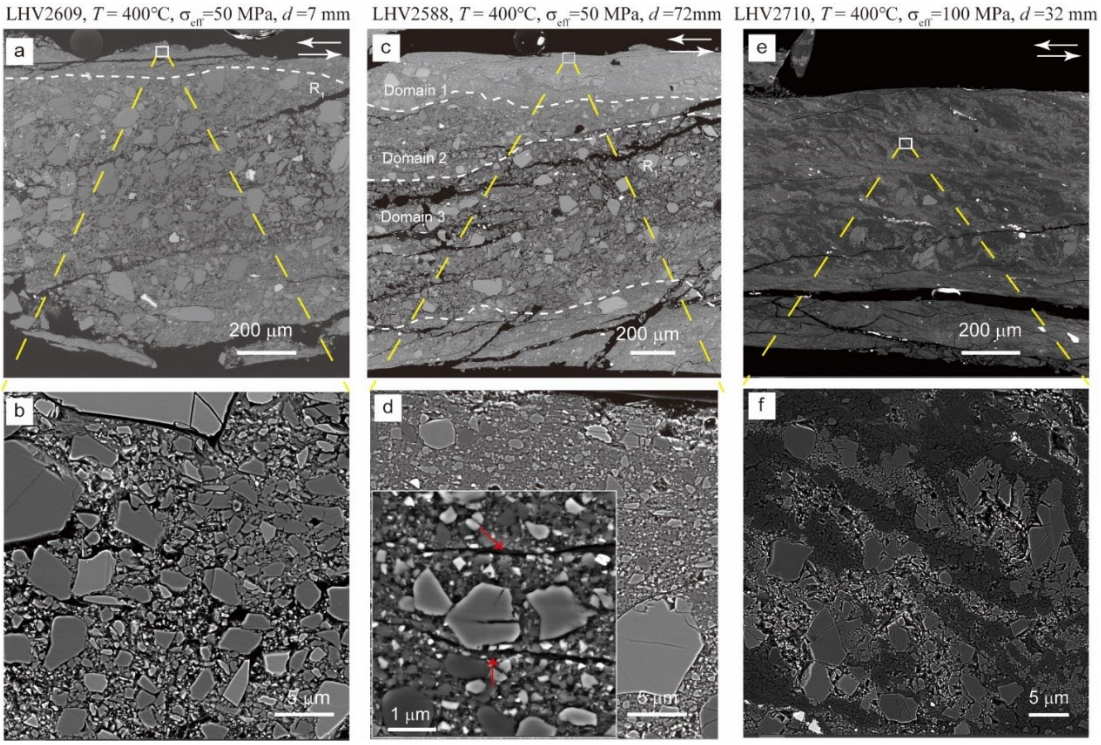

Figure 5.6: Microstructures of sheared gabbro from three experiments at T= 400°C stopped at different displacements. Experimental conditions are reported in the top images. **a-b.** LHV2609: σ_{eff}= 50 MPa, d = 7 mm. **c-d.** LHV2588: σ_{eff}= 50 MPa, d = 72 mm. Red arrows in the inset of "d" indicate the newly-formed clays. **e-f.** LHV2710: σ_{eff}= 100 MPa, d = 32 mm. See text for description.

5.5 Discussion

5.5.1 Slip-dependence of the frictional behavior

In this study, we reported the results of friction experiments conducted on simulated faults made of gabbro and basalt gouges sheared under hydrothermal conditions at T= 300-400°C, P_p=30 MPa and σ_{eff} = 50-100 MPa (Table 5.1). The goal is to investigate the frictional stability conditions of these faults made of common crustal rocks by stepping the imposed V from 16 nm/s to 10 µm/s for large displacement. The mechanical data shown in Figure 5.2 highlight that the transition from velocity weakening (possibly resulting in frictional instability) to velocity strengthening (frictional stability) regime is related to slip displacement and time duration of

experiments. The microstructural analysis of the deformed gabbro gouges recovered from the sample arrested during the *V-W* regime (LHV2609) shows the presence of localized shear zones (Figure 5.6a-b). Instead, deformation involves the entire gouge layer thickness and a S/C foliation develops during the *V-S* regime (LHV2710, Figure 5.6e-f). These microstructural characteristics are consistent with those associated with the brittle to ductile transition for phyllosilicate-rich and calcite-rich gouges sheared at higher temperatures (e.g., T = 600 and 550°C, Zhang and He, 2016; Chen et al., 2020). The microstructures of the sheared basalt recovered from the sample stopped during the *V-S* regime (LHV2583) exhibit the presence of a localized shear zone and unclear grain boundaries. These characteristics are similar to those associated with the *V-S* behavior for basalt sheared at 550°C (Okuda et al., 2023). The frictional response to *V*-steps in the *V-S* regime is gradual (e.g., Figure 5.2b) rather than sharp as usually observed in the RSF framework (Dieterich, 1979; Marone, 1998). However, the deformation mechanism is dominated by cataclasis. Because of this, the stability transition may not completely overlap with the BDT usually referred to by geologists.

In general, the transition of frictional stability from *V-W* to *V-S* observed in our experiments has widely been recognized in previous friction experiments performed on calcite, granite, basalt, gabbro, phyllosilicate-rich mylonite, illite-rich shale and halite-phyllosilicate mixtures under hydrothermal conditions (Verberne et al., 2015; Chen et al., 2020; Blanpied et al., 1991; He et al., 2007; Zhang and He, 2016; Zhang et al., 2017; den Hartog et al., 2012; Okuda et al., 2023). However, these transitions occur at higher temperatures and pressures. For instance, in the case of gabbro gouges sheared for 3 mm at P_p=30 MPa and σ_{eff} = 200 MPa (i.e., higher than in our experiments) the transition from *V-W* to *V-S* occurred at ~ 510°C (He et al., 2007). In the case of fresh basalt gouges from IODP Expedition 349 and sheared for 3 mm at P_p=100 MPa and σ_{eff}= 50 MPa, the frictional behavior remained *V-W* at temperatures up to 600°C (Zhang et al., 2017). Instead, altered basalts from the Mugi mélange sheared at P_p=100 MPa and σ_{eff} = 100 MPa the transition from *V-W* to *V-S* occurred at T ~ 450°C (Okuda et al.,

2023). These temperature values at which the stability transition was observed are systematically higher than the temperatures (i.e., T = 300 and 400°C) at which the transition occurs in our experiments.

The onset of transition into *V-S* behavior can also be promoted by decreases in slip velocity (Shimamoto, 1986; Okuda et al., 2023; Chen et al., 2020; Zhang and He, 2016). For instance, in the case of calcite gouge sheared at T = 550°C the transition from *V-W* to *V-S* is captured when V is decreased at a critical velocity (V_c), at which the velocity dependence changes, of 0.1 μm/s (Chen et al., 2020). In the case of basalt gouges, at T = 500-550°C V_c is 30-100 μm/s, whereas at T = 400-450°C V_c is decreased to 3-10 μm/s (Okuda et al., 2023). The higher temperature corresponds to a higher V_c. These results are consistent with our observations. In basalt gouges sheared at T = 400°C (LHV2586, Figure 5.2b) the *V-S* behavior is activated for V decreasing to 0.4 μm/s (i.e., V_c =0.4 μm/s). Intriguingly, after experiencing ~ 10 mm of slip the V_c for the occurrence of *V-S* is extended to 10 μm/s (Figure 5.2b). This suggests that the *V-S* behavior is facilitated by slip displacement. Although a slip dependence of frictional properties, e.g., frictional healing and sliding behavior, has been previously observed in experiments (Beeler et al., 1996; Richardson and Marone, 1999; Zhang et al., 2017), less attention has been paid to its possible effects on frictional stability transition (Noel et al., 2023).

How slip displacement and fluid-rock interaction contribute to the onset of the transition from *V-W* to *V-S* behavior can be due to the formation of smectites and to grain size reduction. Newly-formed smectites are present in the deformed samples that underwent sufficient long displacement and exhibit frictional creep or *V-S* behavior at the end of the experiments (Figure 5.4). Previous experiments indicated that smectite or smectite-rich gouges are characterized in water-saturated conditions by a low frictional strength (μ ~0.1-0.3) and *V-S* behavior (Moore and Lockner, 2007; Tesei et al, 2015; Saffer and Marone, 2003). Therefore, in our experiments the formation of smectite-like mineral in the gouge may lower the frictional strength and “stabilize” the experimental fault. This would be consistent with previous experimental evidence.

Experiments on talc-quartz and chlorite-epidote mixtures showed that the friction coefficient decreases and the frictional behavior evolves from *V-W* or *V*-neutral into *V-S* when the abundance of these "weak" minerals increases (Niemeijer et al., 2010; An et al., 2021). In fact, the smectite to illite transformation occurs at ~ 150°C lower than the temperatures applied in our experiment. This suggests it would be other clay-like minerals during the deformation.

Also, grain size reduction could play a significant role in contributing to the frictional stability transition. Grain size reduces with increasing slip displacement (Figures 5.5 and 5.6). We suggest that grain size reduction, in the presence of hot and pressurized water, promotes the activation of grain size-sensitive processes. This is because the progressive reduction in grain size will increase the surface area and thus enhance fluid-aided processes such as solution transfer (Durney, 1972) and hydrothermal alternation (Callahan et al., 2019. In fact, the effect of grain size on the transition from *V-W* to *V-S* has been captured by a microphysical model, which shows that decreasing the grain size results in a higher critical velocity (V_c) (Chen et al., 2020). This is consistent with the increased value of V_c with slip displacement (Figure 5.2). In addition, grain size reduction due to comminution will be boosted at higher σ_{eff} and the transition from *V-W* to *V-S* will be promoted correspondingly. This hypothesis is supported, in the case of gabbro-built gouges, that the slip displacement required for the transition occurring is 63 mm and 23 mm for σ_{eff} of 50 (Figure 5.2c) and 100 MPa (Figure 5.2d), respectively. Therefore, we propose that the newly-formed clay minerals and grain size reduction contribute to the transition toward frictional stability.

5.5.2 Geological implications

To sum up, the transition from *V-W* to *V-S* behavior (roughly brittle to ductile) can be facilitated by cumulative slip displacement, in addition to the widely recognized higher *T*, higher σ_{eff} and lower strain rate (Noel et al., 2021; Violay et al., 2015; Shimamoto, 1986; Tullis and Yund, 1980; Chen et al., 2020; Paterson and Weaver, 1970). However,

in the experiments presented here, the microstructural evidence suggest that frictional behavior transition is due to cataclastic-related deformation mechanisms, neo-formation of smectite-like clays and, possibly, grain size-dependent processes (Figs. 5.5-5.6). There is no evidence of crystal-plastic deformation mechanisms. Our results show that this transitional regime is accompanied by the occurrence of complex slip behaviors, e.g., period-multiplying cycle (Figure 5.2c, inset III). Similar behavior has been observed in experiments near the transition from stick-slip to creep (Mei et al., 2021; Bedford et al., 2021). This complex type of frictional sliding may be related to normal stress and fault heterogeneity (Mei et al., 2021). Our findings experimentally provide evidence that slow slip events (SSEs) may occur in the vicinity of the BDT zone (Goswami and Barbot, 2018; Lavier et al., 2021).

Our results also have significant implications for the distribution of seismicity on natural faults in the oceanic crust, as the transition from *V-W* to *V-S* behavior constrains the maximum depth at which earthquakes can nucleate. If the other fault loading conditions remain constant, we hypothesize that the transition promoted by slip displacement may migrate the base of the seismogenic zone to shallower depths with fault maturity or afterslip. Moreover, the *V-W* behavior can be resumed once the slip velocity is raised exceeding the V_c, as observed in the case of gabbro-built gouges stick-slip events occur when V is stepped upwards to 10 μm/s (Figure 5.2c). We extrapolate that the faults in the region beneath the regular seismogenic zone (*V-S* regime) may show frictional instability due to the elevated strain rates caused by the mainshock, contributing to the nucleation of aftershocks. This could explain the observed transient deepening of aftershocks following the mainshocks (Schaff et al., 2002; Rolandone et al., 2004; Cheng and Ben-Zion, 2019). Meanwhile, the distribution of aftershocks after instantaneous deepening has been recorded to move towards shallow depths over time (Cheng and Ben-Zion, 2019). This gradual shallowing of aftershocks is comparable with post-seismic relaxation as usually recognized (Nishimura and Thatcher, 2003), our work suggests that the post-seismic slip can also facilitate the (shear-induced) transition

from instability to stability along the faults.

5.6 Conclusions

We performed a series of velocity-stepping tests on simulated gabbro- and basalt-built gouges under 50 MPa effective normal stress, at 300 and 400°C and 50 MPa pore pressure, covering 5 orders of magnitude in velocity (16 nm/s to 10 μm/s) to investigate the effect of slip displacement on frictional stability. Our results demonstrate that the transition from frictional instability to stability depends not only on temperature, normal stress and loading velocity but also on fault slip history that affects grain size, mineral composition and the simulated fault zone structure. These findings have important implications for the fault slip behavior in the vicinity of the BDT zone and provide a new perspective on the understanding of the distribution of seismicity, particularly aftershocks.

5.7 Appendices

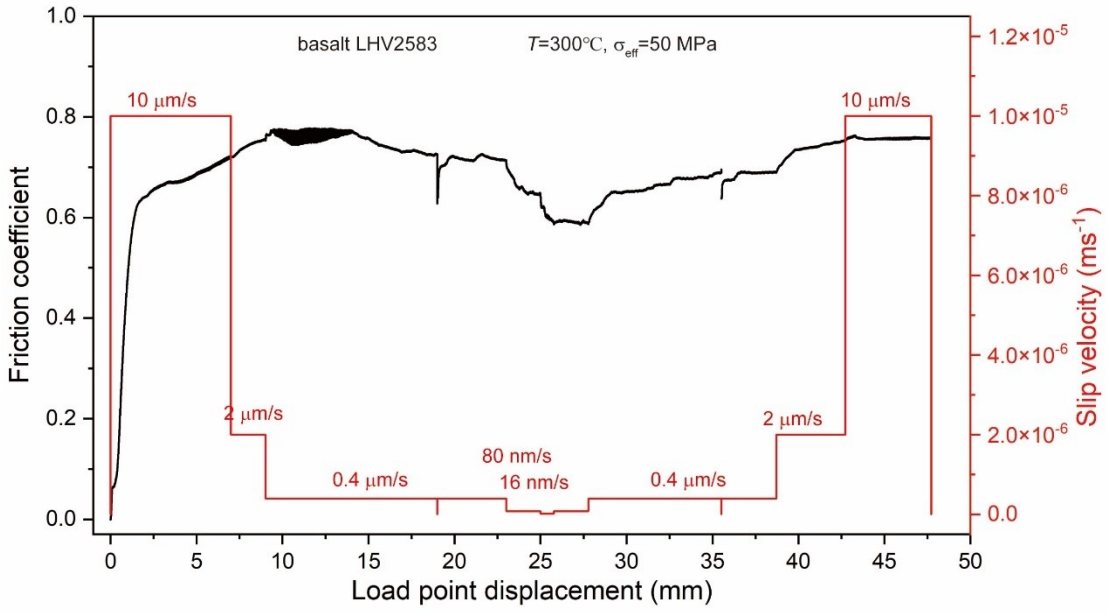

Figure 5.7: Results from a repeated experiment on basalt (LHV2583) performed at T = 300°C, σ_{eff} = 50 MPa and P_p = 30 MPa showing well-reproducible data with experiment (LHV2578). Velocities are reported in the diagram. A transition of velocity dependence from *V-W* to *V-S* is observed at *V*=

0.4 μm/s after ~ 12 mm of slip displacement.

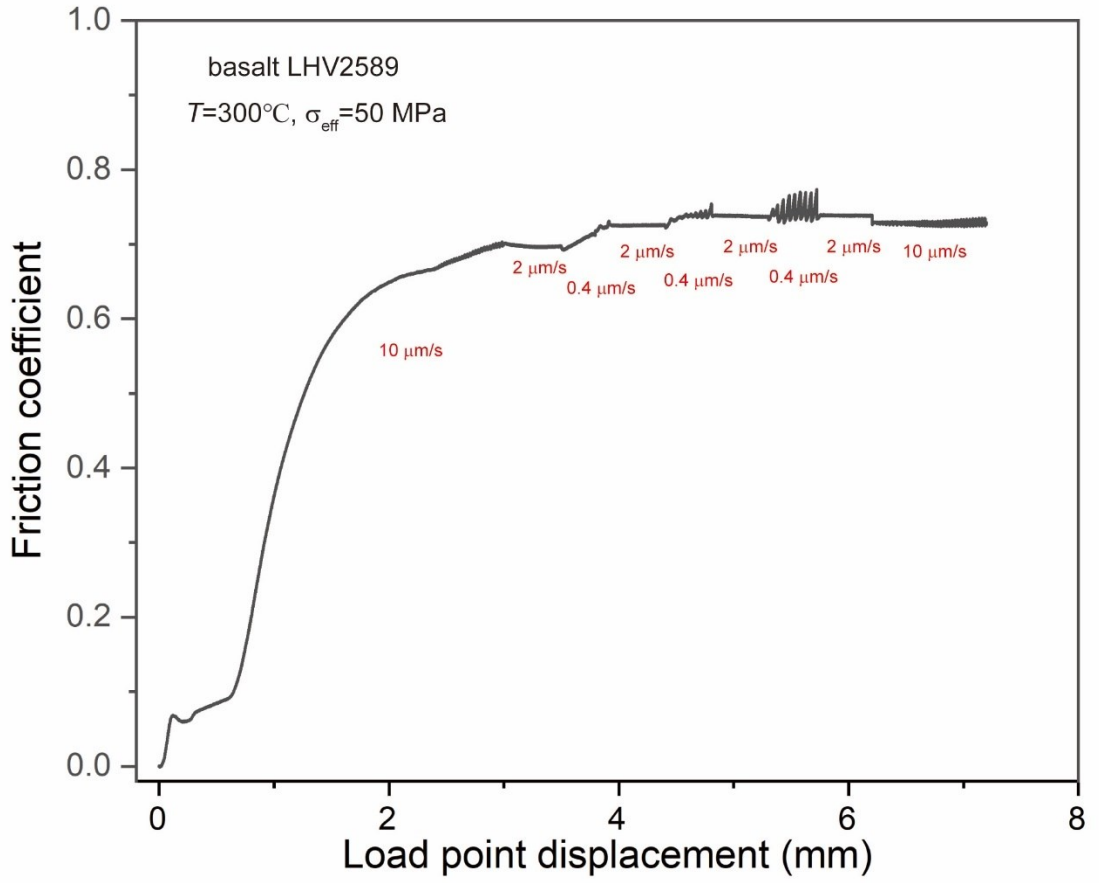

Figure 5.8: Friction coefficient versus slip displacement in the experiment (LHV2589) on basalt gouges performed at 300℃ and σ_{eff} = 50 MPa. Experiment is arrested during the *V-W* regime, *d* = 7 mm.

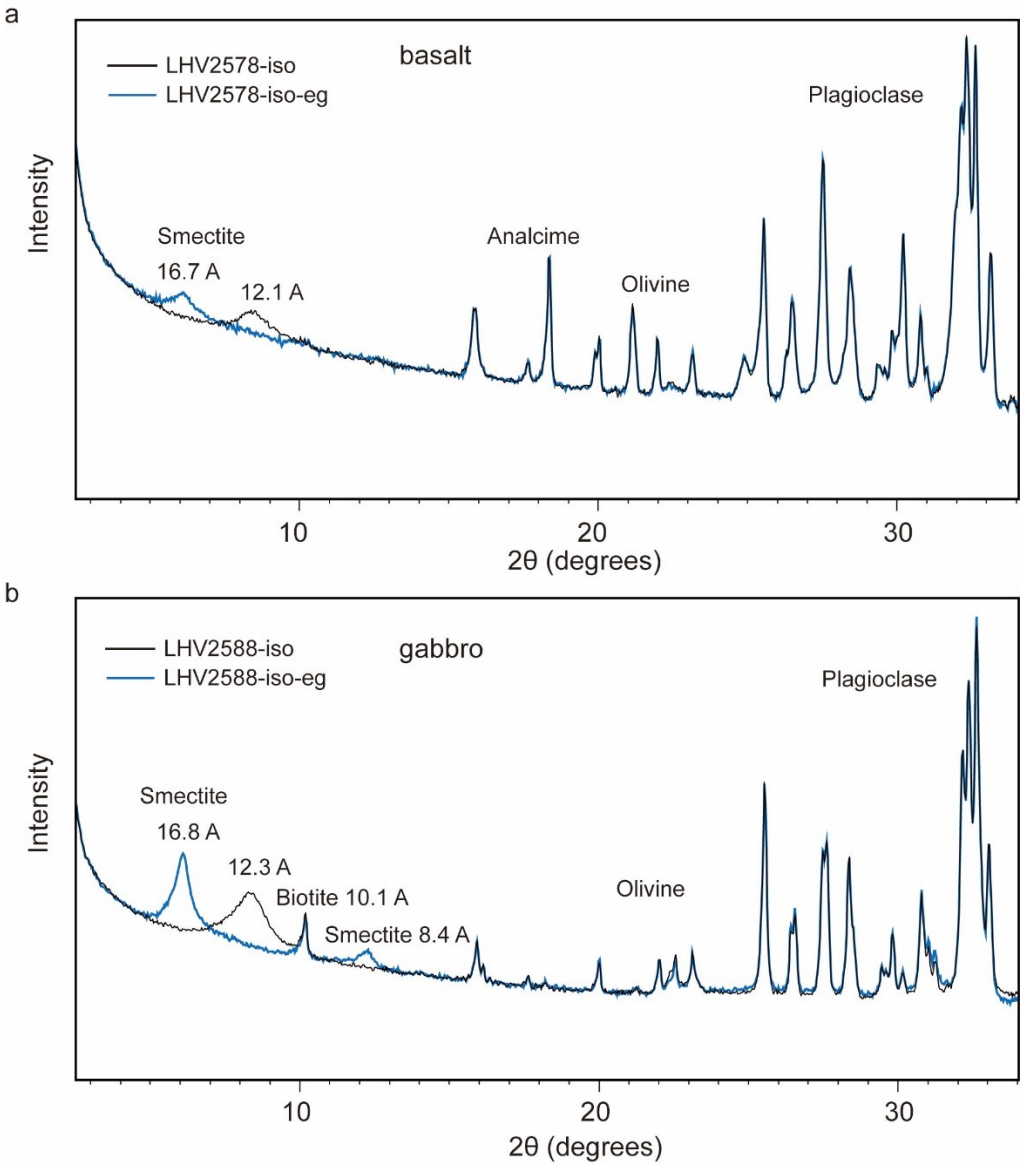

Figure 5.9: XRD spectra after iso-oriented and ethylene glycol treatment of powders recovered from the experiments LHV2578 (basalt) and LHV2588 (gabbro) exhibiting *V-S* behavior. The spectra show that smectite-like mineral is present. **a.** Experiment LHV257. **b.** Experiment LHV2588.

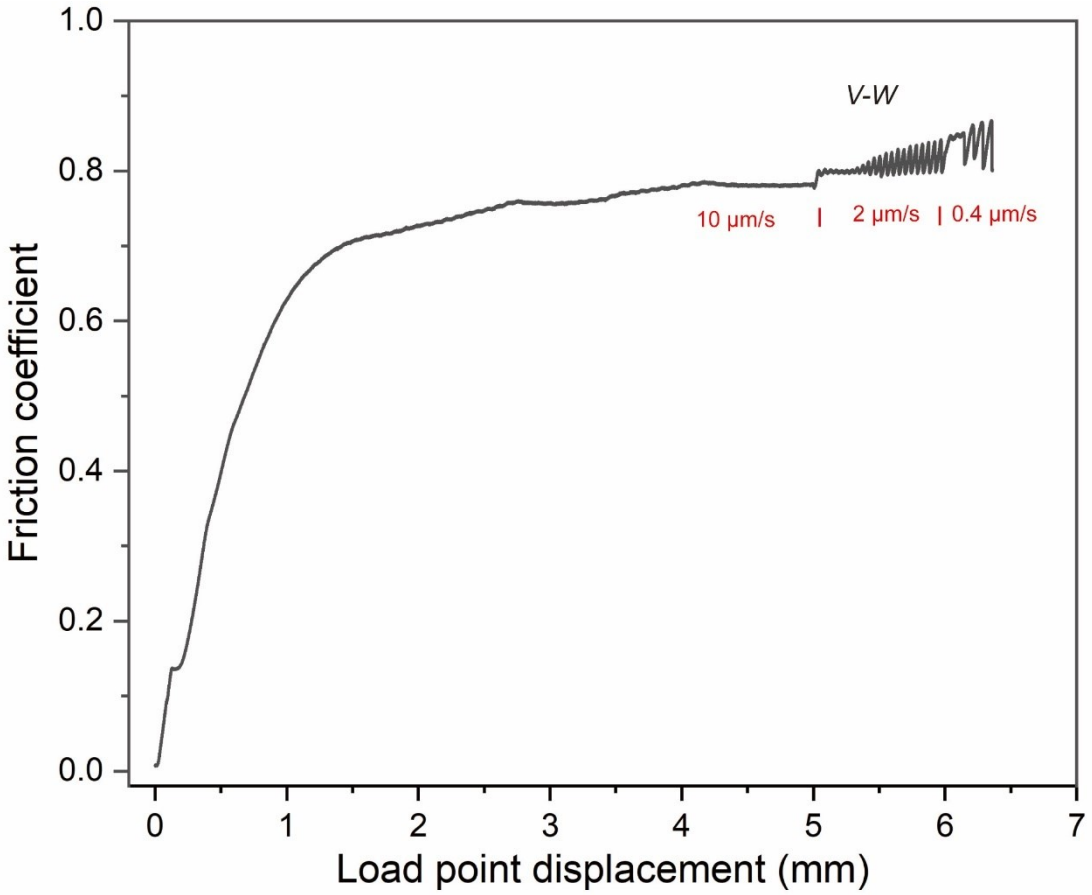

Figure 5.10: Friction coefficient versus slip displacement in the experiment (LHV2609) on gabbro gouges performed at 400°C, 50 MPa σ_{eff} and 30 MPa P_p. Experiment is stopped after d ~ 7 mm during the *V-W* regime.

6 Conclusions and Perspectives

6.1 Main results of the thesis

Earthquakes often originate and propagate in the presence of hydrothermal fluids. Previous studies have suggested fluids govern earthquake nucleation and fault strength (Blanpied et al., 1992; Wibberley et al., 2005). In this thesis, I report the results of frictional behavior of experimental faults made of gabbro and basalt sheared at hydrothermal conditions. These experimental data were obtained thanks to the installation of a new dedicated hydrothermal pressure vessel, which took about ten years to be developed by Prof. Shimamoto to overcome a series of technical challenges, on a rotary shear machine. These experiments were mainly performed at the IGCEA in Beijing because of the impact of COVID-19 which delayed of 18 months the installation of an identical hydrothermal vessel in the Rock Deformation Laboratory in Padua University. Specifically, experimental work focused on three main questions related to the seismic cycle under hydrothermal conditions:

(1) how does the presence of hot and pressurized fluids affect the **frictional strength** during sub- to co-seismic slip?

(2) how do the experimental faults recover their strength (**frictional healing**) in the presence of hydrothermal fluids during the quasi-stationary (or inter-seismic) phase?

(3) How does fault **frictional stability** evolve in large displacement experiments (> few cm) under hydrothermal conditions? Does cumulative slip affect the velocity dependence of the friction coefficient?

The major findings addressing these questions are as follows:

6.1.1 Frictional strength

25 constant slip velocity experiments were performed with a rotary shear machine

(LHVR-Beijing) on solid gabbro (28 mm in diameter) to investigate the frictional strength in the presence of water under liquid, vapor and supercritical state (Chapter 3). Gabbro cylinders were sheared at 10 MPa effective normal stress, slip velocities from 1 μm/s to 100 mm/s and slip displacement up to 3 m.

Our mechanical data show that friction coefficient of gabbro can be as low as 0.3 regardless of imposed slip velocity when pressurized water is in liquid and supercritical state (i.e., T=300°C & P_p=10 MPa and T=400°C & P_p=30 MPa, respectively), while friction coefficient decreases with increasing slip velocity when pressurized water is in vapor state (i.e., T=400°C & P_p=10 MPa), similarly as in room humidity experiments (Di Toro et al., 2021) (Figure 3.4). XRD analyses on the slip zones sheared with liquid and supercritical water reveal the presence of a mixture of chlorite and smectite, absent in the starting materials. The presence of clay-like newly-formed minerals was confirmed by high-resolution FESEM investigations. Similarly, the H-O-H bending vibrational mode of H_2O is detected in the micro-Raman spectra of the slip surfaces recovered from the liquid and supercritical water experiments, but not from the vapor water experiments (Figure 3.8). In addition, elastohydrodynamic (EHD) lubrication was evaluated as a possible weakening mechanism responsible for low friction at low velocity (e.g., 10 μm/s). Our results show that the EHD lubrication can be activated once the required viscosity is attained by a mixture of rock powders with liquid and supercritical water. We conclude that fault weakening at low velocities (sub-seismic) in the presence of liquid and supercritical water is related to the physical (EHD lubrication) and chemical (H-O-H bending) role of water together with the formation of newly-formed minerals.

6.1.2 Frictional healing

A series of slide-hold-slide (SHS) experiments were performed on experimental faults made of gabbro gouges to investigate the fault strength recovery (i.e., frictional healing) under dry and hydrothermal conditions (Chapter 4). Experiments were conducted at σ_{eff}

of 50 MPa, T ranging from 25 to 400°C and P_p of 0 or 30 MPa. In the SHS sequence, the imposed slip velocity was V=10 μm/s, and hold time t_h varied from 3 to 10000 s. For each experiment, two SHS sequences separated by a slip displacement interval of 40 mm were conducted (Figure 4.3).

Our results show that under dry conditions at $T \leq$200°C and under hydrothermal conditions but at $T \leq$100°C, frictional healing $\Delta\mu$ increases with t_h, consistent with previous experiments (Marone, 1998; Chen et al., 2015; Hunfeld et al., 2020; Carpenter et al., 2016) (Figures 4.5 and 4.6). Moreover, the $\Delta\mu$ and healing rate β values in the 2nd SHS sequence are slightly higher than those in the 1st sequence, possibly due to the smaller grain size at the larger displacement that promotes fault healing. By contrast, in the experiments performed under dry conditions at $T \geq$ 300°C with large slip displacement or under hydrothermal conditions at $T \geq$ 200s, $\Delta\mu$ decreases and β switches to negative values (<0) when the hold is longer than a threshold time (Figure 4.6). We conclude that the decrease in $\Delta\mu$ and the transition of β from positive to negative cannot be solely explained by the change in the real area of contact. As temperature increases and in the presence of fluids, the breaking of chemical bonds at the contact interface becomes active, resulting in a decrease in bond strength. Our results suggest that the increase of the contact area ("quantity") and the decrease of the contact strength ("quality") operate together, contributing to frictional healing.

6.1.3 Frictional stability

Velocity-stepping experiments were performed on basalt-built and gabbro-built gouges under ambient conditions up to 400°C and 100 MPa normal stress, approaching in some cases the so called "brittle-ductile" transition and at slip velocities ranging from 16 nm/s to 10 μm/s (Chapter 5). The slip displacement was imposed up to ~80 mm to investigate the slip-dependence of frictional stability.

Our results reveal that, in both basalt- and gabbro-built gouges, cumulative slip and duration of the experiment facilitate the onset of the transition from velocity weakening

(frictional instability) to velocity strengthening (frictional stability) behavior (Figure 5.2). Moreover, the constant velocity experiment performed on basalt gouges at T = 300°C and V=0.4 μm/s shows that stick-slip behavior gradually evolves to creep with slip displacement (Figure 5.3). XRD analysis on deformed both samples which exhibit velocity strengthening behavior consistently shows the presence of newly-formed smectite. The microstructural analysis (SEM) of the deformed gabbro gouges recovered from the sample arrested during the velocity weakening regime shows the presence of localized shear zones, while, when arrested during the velocity strengthening regime, deformation involves the entire gouge layer thickness and a S/C foliation develops. We interpret that with increasing slip displacement, frictional sliding and fluid-rock interaction result in the formation of smectite-type clays and in grain size reduction. These may contribute to the initiation of the transition from frictional instability to stability.

6.2 Implications for the seismic cycle

The main results discussed in this thesis have significant implications for each stage of the seismic cycle in natural and human-induced earthquakes, particularly in high enthalpy geothermal reservoirs. For instance, in the rupture nucleation stages, slip zone dilatancy may cause a dramatic drop in pore fluid pressure, resulting in a phase change of pore fluid from liquid or supercritical state to vapor. According to our results (Figure 3.4, Chapter 3), this phase transition of pore fluid at nucleation velocity can increase friction strength, which may delay or stop the nucleation stage. Moreover, velocity-stepping experiments performed under ambient conditions close to the lower boundary of the seismogenic zone reveal that the transition from velocity weakening to velocity strengthening occurs with cumulative slip displacement. This implies that, under specific ambient conditions, fault maturity or afterslip can promote the transition from frictional instability to stability, inhibiting earthquake nucleation (Figure 5.2, Chapter 5).

In the rupture propagation stage, when slip velocity ≥ 10 mm/s, the experimental faults show a drastic decrease in friction coefficient from 0.7 to 0.2-0.3, independent of the physical state of pressurized water (Figure 3.4, Chapter 3). These results are consistent with the experiments performed at room humidity or in the presence of liquid water at ambient temperature (e.g., Niemeijer et al., 2011; Violay et al., 2014; 2015).

During the inter-seismic period, faults need to recover their strength for earthquakes to repeatedly occur. This process of increase in static friction over time is known as frictional healing. Our slide-hold-slide experiments show that the well-known log-linear relation between frictional healing and hold time is relaxed at temperature > 200°C, especially in the presence of pressurized water (Figure 4.6, Chapter 4). The healing rate switches from positive to negative for hold durations longer than a threshold time (Figure 4.6f, Chapter 4). In the case of natural faults, if the fault tectonic loading remains the same and if frictional healing decrease with the hold period, we would expect the number of earthquakes per unit of time to increase.

6.3 Future work

This work has provided a new dataset on the frictional properties of experimental faults (gabbro and basalt) under hydrothermal conditions, challenging in some cases the results attained from small-displacement experiments. Our results also invoke several new questions that need to be investigated in future studies.

6.3.1 High velocity (V ≥ 1 m/s) experiments

As described in Chapter 3, constant velocity experiments on cylinder rocks have been performed at slip velocities from 10 μm/s to 0.1 m/s. It has been shown that the ambient conditions (e.g., the physical state of pore water) strongly affect the fault strength and frictional behavior. However, the velocity imposed in the experiments in this study did not reach 1 m/s, a slip velocity considered typical of coseismic slip in natural faults and imposed in hundreds to thousands of high velocity experiments performed at room

humidity conditions so far. High-resolution FESEM analysis of the deformed samples recovered from the experiment performed at 0.1 m/s in the presence of supercritical water indicate the presence of three microstructural domains in the slip zone and the presence of injection veins in the wall rocks (see Figure 3.15b, Chapter 3). The microstructure of one of these domains is fully crystalline and made of micrograins of pyroxene and albite. Similar microstructures have not been described in the slip zones of experiments preformed on gabbro sheared at similar slip velocities and in the presence of water but at room temperature conditions. In the latter case, the slip zone is made of clasts suspended in a glassy-like matrix (experimental pseudotachylyte). Instead, this fully crystalline slip zone resembles mineralizations found in some natural faults, rather than the product of solidification of a friction melt. This finding requires further studies.

Moreover, though EHD lubrication seems a reasonable weakening mechanism in the presence of liquid and supercritical water as discussed in Chapter 3, further studies are required to understand better the role of the "chemistry" in these experiments. This would also require the sampling of the fluids, the chemical analysis of both the fluids and the solids (Ion chromatography, ICP-MS and ICP-OES techniques, XRF, etc.) and chemical modeling with dedicated software (e.g., TOUGHREACT V4). These analysis and models would allow to identify the type and extent of fluid-rock interaction occurring under the explored laboratory hydrothermal conditions and how these are related to the mechanisms that lead to friction evolution (or fault healing, see next section) under sub-critical to supercritical water conditions.

New high velocity experiments should be performed in the future, with the aim to investigate whether other dynamic weakening mechanisms are activated under these conditions, establish the fundamental link between mechanical data and microstructures and, lastly, compare the experimental with the natural fault produces. In fact, without this comparison, the extrapolation of our mechanical data to natural conditions should be performed with extreme caution.

6.3.2 Mechanisms responsible for decreased frictional healing

The slide-hold-slide experiments presented in Chapter 4 reveal the log-linear relation between frictional healing and the hold time, usually recognized in room condition experiments, does not hold at high temperatures (T >200°C), especially in the presence of pressurized fluids. The frictional healing rate (i.e., the slope of $d(\Delta\mu)/d\ [log_{10}t_h]$) decreases with increasing hold time (Figure 4.6). We interpret that this is a result of the decreased contact strength, counteracting the increased contact area. However, this is only supported by theoretical concepts and modeling simulations (Li et al., 2018; Ouyang et al., 2022), while direct experimental evidence is not available. In addition, the frictional interface typically includes different minerals and types of contact bonds, which add further complexity to the evolution of the chemical bonds and fault strength with time. Therefore, it is suggested to perform similar SHS experiments on samples containing a single mineral (i.e., quartz: SiO_2) in future studies. In fact, if negative healing is also observed here, although still challenging, its modeling would be easier to deal with. Indeed, the solubility of SiO_2 in water is well known, hydrolytic weakening, sub-critical growth and stress corrosion for SiO_2 have been studies extensively (Tullis and Yund, 1980; Michalske and Freiman, 1982; Zhu et al., 2005; Atkinson, 1982), and chemical aging models are based on asperity contacts made of SiO_2 (Li et al., 2018).

Bibliography

Acosta, M., Passelegue, F. X., Schubnel, A. & Violay, M., 2018, Dynamic weakening during earthquakes controlled by fluid thermodynamics: Nature Communications, v. 9, 3074, https://doi.org/10.1038/s41467-018-05603-9.

An, M. et al., 2020, Frictional stability of metamorphic epidote in granitoid faults under hydrothermal conditions and implications for injection-induced seismicity: Journal of Geophysical Research: Solid Earth, v. 127, e2021JB023136, https://doi.org/10.1029/2021JB023136.

An, M., Zhang, F., Min, K. B., Elsworth, D., Marone, C., and He, C., 2021, The Potential for low-grade metamorphism to facilitate fault instability in a geothermal reservoir: Geophysical Research Letters, v. 48, https://doi.org/10.1029/2021GL093552.

Aretusini, S., Meneghini, F., Spagnuolo, E., Harbord, C. W., and Di Toro, G., 2021, Fluid pressurisation and earthquake propagation in the Hikurangi subduction zone: Nature Communications, v. 12, p. 2481, https://doi.org/10.1038/s41467-021-22805-w.

Asanuma, H., Muraoka, H., Tsuchiya, N., and Ito, H., 2012, The concept of the Japan Beyond-Brittle Project (JBBP) to develop EGS reservoirs in ductile zones: Transaction-Geothermal Resources Council, v. 36, p. 359-364.

Asanuma, H., Nozaki, H., Niitsuma, H., and Wyborn, D., 2005, Interpretation of microseismic events with larger magnitude collected at Cooper Basin, Australia: Geothermal Resources Council Transactions, v. 29, p. 87-92.

Atkinson, B. K., 1982, Subcritical crack propagation in rocks: theory, experimental results and applications: Journal of Structural Geology, v. 4, p. 41-56, https://doi.org/10.1016/0191-8141(82)90005-0.

Atkinson, B. K., 1984, Subcritical crack growth in geological materials: Journal of Geophysical Research: Solid Earth, v. 89, p. 4077-4114,

https://doi.org/10.1029/JB089iB06p04077.

Audet, P., Bostock, M. G., Christensen, N. I., and Peacock, S. M., 2009, Seismic evidence for overpressured subducted oceanic crust and megathrust fault sealing: Nature, v. 457, p. 76-78, https://doi.org/10.1038/nature07650.

Baisch, S., Weidler, R., Vörös, R., Wyborn, D., and de Graaf, L., 2006, Induced seismicity during the stimulation of a geothermal hfr reservoir in the Cooper Basin, Australia: Bulletin of the Seismological Society of America, v. 96, p. 2242-2256, https://doi.org/10.1785/0120050255.

Barbier, E., 2002, Geothermal energy technology and current status: an overview: Renewable and Sustainable Energy Reviews, v. 6, p. 3-65, https://doi.org/10.1016/S1364-0321(02)00002-3.

Barbot, S., 2019, Slow-slip, slow earthquakes, period-two cycles, full and partial ruptures, and deterministic chaos in a single asperity fault: Tectonophysics, v. 768, 228171, https://doi.org/10.1016/j.tecto.2019.228171.

Barbot, S., 2022, A rate-, state-, and temperature-dependent friction law with competing healing mechanisms: Journal of Geophysical Research: Solid Earth, v. 127, p. e2022JB025106, https://doi.org/10.1029/2022JB025106.

Bedford, J. D., and Faulkner, D. R., 2021, The role of grain size and effective normal stress on localization and the frictional stability of simulated quartz gouge: Geophysical Research Letters, v. 48, https://doi.org/10.1029/2020GL092023.

Beeler, N. M., Tullis, T. E., Blanpied, M. L., and Weeks, J. D., 1996, Frictional behavior of large displacement experimental faults: Journal of Geophysical Research: Solid Earth, v. 101, p. 8697-8715, https://doi.org/10.1029/96JB00411.

Ben-Zion, Y., and Sammis, C. G., 2003, Characterization of fault zones: pure and applied geophysics, v. 160, p. 677-715, https://doi.org/10.1007/PL00012554.

Bistacchi, A., Massironi, M., and Menegon, L., 2010, Three-dimensional characterization of a crustal-scale fault zone: The Pusteria and Sprechenstein fault system (Eastern Alps): Journal of Structural Geology, v. 32, p. 2022-2041,

https://doi.org/10.1016/j.jsg.2010.06.003.

Bizzarri, A., and Cocco, M., 2006, A thermal pressurization model for the spontaneous dynamic rupture propagation on a three-dimensional fault: 2. Traction evolution and dynamic parameters: Journal of Geophysical Research: Solid Earth, v. 111, B05304, https://doi.org/10.1029/2005JB003864.

Blanpied, M. L., Lockner, D. A. & Byerlee, J. D., 1995, Frictional slip of granite at hydrothermal conditions: Journal of Geophysical Research: Solid Earth, v. 100, p. 13045-13064, https://doi.org/10.1029/95JB0086.

Blanpied, M. L., Lockner, D. A., and Byerlee, J. D., 1991, Fault stability inferred from granite sliding experiments at hydrothermal conditions: Geophysical Research Letters, v. 18, p. 609-612, https://doi.org/10.1029/91GL00469.

Blanpied, M. L., Lockner, D. A., and Byerlee, J. D., 1992, An earthquake mechanism based on rapid sealing of faults: Nature, v. 358, p. 574-576, https://doi.org/10.1038/358574a0.

Bowden, F. P., and Tabor, D., 1950, The Friction and Lubrication of Solids: Part 1. Oxford: Clarendon Press.

Brace, W. F., and Byerlee, J. D., 1966, Stick-slip as a mechanism for earthquakes: Science, v. 153, p. 990-992, https://doi.org/10.1126/science.153.3739.990.

Brandt, L. & Coletti, F., 2022, Particle-laden turbulence: progress and perspectives: Annual Review of Fluid Mechanics, v. 54, p. 159-189, https://doi.org/10.1146/annurev-fluid-030121-021103.

Brantut, N., 2020, Dilatancy-induced fluid pressure drop during dynamic rupture: Direct experimental evidence and consequences for earthquake dynamics: Earth and Planetary Science Letters, v. 538, 116179, https://doi.org/10.1016/j.epsl.2020.116179.

Brantut, N., Heap, M. J., Meredith, P. G., and Baud, P., 2013, Time-dependent cracking and brittle creep in crustal rocks: A review: Journal of Structural Geology, v. 52, p. 17-43, https://doi.org/10.1016/j.jsg.2013.03.007.

Brindley, G. and Brown, G., 1980, Crystal Structures of Clay Minerals and their X-Ray Identification: Mineralogical Society of Great Britain and Ireland.

Brodsky, E. E. & Kanamori, H., 2001, Elastohydrodynamic lubrication of faults: Journal of Geophysical Research: Solid Earth, v. 106, p. 16357-16374, https://doi.org/10.1029/2001jb000430.

Brown, K. M., and Fialko, Y., 2012, 'Melt welt' mechanism of extreme weakening of gabbro at seismic slip rates: Nature, v. 488, no. 7413, p. 638-641, https://doi.org/10.1038/nature11370.

Burridge, R., and Knopoff, L., 1967, Model and theoretical seismicity: Bulletin of the Seismological Society of America, v. 57, p. 341-371, https://doi.org/10.1785/BSSA0570030341.

Burridge, R., and Knopoff, L., 1967, Model and theoretical seismicity: Bulletin of the Seismological Society of America, v. 57, p. 341-371, https://doi.org/10.1785/BSSA0570030341.

Byerlee, J., 1978, Friction of rocks: Pure and Applied Geophysics, v. 116, p. 615-626, https://doi.org/10.1007/BF00876528.

Caine, J. S., Evans, J. P., and Forster, C. B., 1996, Fault zone architecture and permeability structure: Geology, v. 24, p. 1025-1028, https://doi.org/10.1130/0091-7613(1996)024<1025:FZAAPS>2.3.CO;2.

Callahan, O. A., Eichhubl, P., Olson, J. E., and Davatzes, N. C., 2019, Fracture mechanical properties of damaged and hydrothermally altered rocks, Dixie valley-Stillwater fault zone, Nevada, USA: Journal of Geophysical Research: Solid Earth, v. 124, p. 4069-4090, https://doi.org/10.1029/2018JB016708.

Caristan, Y., 1982, The transition from high temperature creep to fracture in Maryland diabase: Journal of Geophysical Research: Solid Earth, v. 87, p. 6781-6790, https://doi.org/10.1029/JB087iB08p06781.

Carpenter, B. M., Ikari, M. J., and Marone, C., 2016, Laboratory observations of time-dependent frictional strengthening and stress relaxation in natural and synthetic

fault gouges: Journal of Geophysical Research: Solid Earth, v. 121, p. 1183-1201, https://doi.org/10.1002/2015JB012136.

Chen, J., Verberne, B. A., and Niemeijer, A. R., 2020, Flow-to-friction transition in simulated calcite gouge: experiments and microphysical modeling: Journal of Geophysical Research: Solid Earth, v. 12, p. e2020JB019970, https://doi.org/10.1029/2020JB019970.

Chen, J., Verberne, B. A., and Spiers, C. J., 2015, Interseismic re-strengthening and stabilization of carbonate faults by "non-Dieterich" healing under hydrothermal conditions: Earth and Planetary Science Letters, v. 423, p. 1-12, https://doi.org/10.1016/j.epsl.2015.03.044.

Chester, F. M., 1994, Effects of temperature on friction: Constitutive equations and experiments with quartz gouge: Journal of Geophysical Research: Solid Earth, v. 99, p. 7247-7261, https://doi.org/10.1029/93JB03110.

Chester, F. M., and Logan, J. M., 1986, Implications for mechanical properties of brittle faults from observations of the Punchbowl fault zone, California: pure and applied geophysics, v. 124, p. 79-106, https://doi.org/10.1007/BF00875720.

Collettini, C., Niemeijer, A., Viti, C. & Marone, C., 2009, Fault zone fabric and fault weakness: Nature, v. 462, p. 907-910, https://doi.org/10.1038/nature08585.

Collettini, C., Tesei, T., Scuderi, M. M., Carpenter, B. M., and Viti, C., 2019, Beyond Byerlee friction, weak faults and implications for slip behavior: Earth and Planetary Science Letters, v. 519, p. 245-263, https://doi.org/10.1016/j.epsl.2019.05.011.

Cornelio, C. & Violay, M., 2020, Parametric analysis of the elastohydrodynamic lubrication efficiency on induced seismicity: Geophysical Journal International, v. 222, p. 517-525, https://doi.org/10.1093/gji/ggaa180.

Cornelio, C., Spagnuolo, E., Di Toro, G., Nielsen, S. & Violay, M., 2019, Mechanical behaviour of fluid-lubricated faults: Nature Communications, v. 10, 1274, https://doi.org/10.1038/s41467-019-09293-9.

Cornet, F. H., Bérard, T., and Bourouis, S., 2007, How close to failure is a granite rock mass at a 5km depth?: International Journal of Rock Mechanics and Mining Sciences, v. 44, p. 47-66, https://doi.org/10.1016/j.ijrmms.2006.04.008.

Davis, E. E., and Villinger, H. W., 2006, Transient formation fluid pressures and temperatures in the Costa Rica forearc prism and subducting oceanic basement: CORK monitoring at ODP Sites 1253 and 1255: Earth and Planetary Science Letters, v. 245, p. 232-244, https://doi.org/10.1016/j.epsl.2006.02.042.

De Paola, N., Hirose, T., Mitchell, T., Di Toro, G., Viti, C., and Shimamoto, T., 2011, Fault lubrication and earthquake propagation in thermally unstable rocks: Geology, v. 39, p. 35-38, https://doi.org/10.1130/G31398.1.

De Paola, N., Holdsworth, R. E., Viti, C., Collettini, C., and Bullock, R., 2015, Can grain size sensitive flow lubricate faults during the initial stages of earthquake propagation?: Earth and Planetary Science Letters, v. 431, p. 48-58, https://doi.org/10.1016/j.epsl.2015.09.002.

Deichmann, N., and Giardini, D., 2009, Earthquakes induced by the stimulation of an enhanced geothermal system below Basel (Switzerland): Seismological Research Letters, v. 80, p. 784-798, https://doi.org/10.1785/gssrl.80.5.784.

den Hartog, S. A. M., Niemeijer, A. R. & Spiers, C. J., 2012, New constraints on megathrust slip stability under subduction zone P–T conditions: Earth and Planetary Science Letters, v. 353-354, p. 240-252, https://doi.org/10.1016/j.epsl.2012.08.022.

Di Toro, G. et al., 2011, Fault lubrication during earthquakes: Nature, v. 471, p. 494-498, https://doi.org/10.1038/nature09838.

Di Toro, G., Aretusini, S., Cornelio, C., Nielsen, S., Spagnuolo, E., Núñez-Cascajero, A., Tapetado, A., and Vázquez, C., 2021, Friction during earthquakes: 25 years of experimental studies: IOP Conference Series: Earth and Environmental Science, v. 861, p. 052032, https://doi.org/10.1088/1755-1315/861/5/052032.

Di Toro, G., Han, R., Hirose, T., De Paola, N., Nielsen, S., Mizoguchi, K., Ferri, F.,

Cocco, M., and Shimamoto, T., 2011, Fault lubrication during earthquakes: Nature, v. 471, p. 494-498, https://doi.org/10.1038/nature09838.

Di Toro, G., Hirose, T., Nielsen, S., and Shimamoto, T., 2006, Relating high-velocity rock-friction experiments to coseismic slip in the presence of melts, Earthquakes: Radiated Energy and the Physics of Faulting, p. 121-134, https://doi.org/10.1029/170GM13.

Di Toro, G., Hirose, T., Nielsen, S., Pennacchioni, G., and Shimamoto, T., 2006, Natural and experimental evidence of melt lubrication of faults during earthquakes: Science, v. 311, p. 647-649, https://doi.org/10.1126/science.1121012.

Di Toro, G., Nielsen, S., and Pennacchioni, G., 2005, Earthquake rupture dynamics frozen in exhumed ancient faults: Nature, v. 436, p. 1009-1012, https://doi.org/10.1038/nature03910.

Dieterich, J. H., 1972, Time-dependent friction in rocks: Journal of Geophysical Research, v. 77, p. 3690-3697, https://doi.org/10.1029/JB077i020p03690.

Dieterich, J. H., 1979, Modeling of rock friction: 1. Experimental results and constitutive equations: Journal of Geophysical Research: Solid Earth, v. 84, p. 2161-2168, https://doi.org/10.1029/JB084iB05p02161.

Dieterich, J. H., and Kilgore, B. D., 1994, Direct observation of frictional contacts: New insights for state-dependent properties: pure and applied geophysics, v. 143, p. 283-302, https://doi.org/10.1007/BF00874332.

Dunkel, K. G., Austrheim, H., Renard, F., Cordonnier, B., and Jamtveit, B., 2017, Localized slip controlled by dehydration embrittlement of partly serpentinized dunites, Leka Ophiolite Complex, Norway: Earth and Planetary Science Letters, v. 463, p. 277-285, https://doi.org/10.1016/j.epsl.2017.01.047.

Durney, D. W., 1972, Solution-transfer, an important geological deformation mechanism: Nature, v. 235, p. 315-317, https://doi.org/10.1038/235315a0.

Ellsworth, W. L., and Bulut, F., 2018, Nucleation of the 1999 Izmit earthquake by a triggered cascade of foreshocks: Nature Geoscience, v. 11, p. 531-535,

https://doi.org/10.1038/s41561-018-0145-1.

Evans, B., and Kohlstedt, D. L., 1995, Rheology of Rocks, Rock Physics and Phase Relations, p. 148-165, https://doi.org/10.1029/RF003p0148.

Faulkner, D. R., Jackson, C. A. L., Lunn, R. J., Schlische, R. W., Shipton, Z. K., Wibberley, C. A. J., and Withjack, M. O., 2010, A review of recent developments concerning the structure, mechanics and fluid flow properties of fault zones: Journal of Structural Geology, v. 32, p. 1557-1575, https://doi.org/10.1016/j.jsg.2010.06.009.

Faulkner, D. R., Lewis, A. C., and Rutter, E. H., 2003, On the internal structure and mechanics of large strike-slip fault zones: field observations of the Carboneras fault in southeastern Spain: Tectonophysics, v. 367, p. 235-251, https://doi.org/10.1016/S0040-1951(03)00134-3.

Faulkner, D. R., Mitchell, T. M., Rutter, E. H., and Cembrano, J., 2008, On the structure and mechanical properties of large strike-slip faults: Geological Society, London, Special Publications, v. 299, p. 139-150, https://doi.org/10.1144/SP299.9.

Fredrich, J. T., Evans, B., and Wong, T.-F., 1989, Micromechanics of the brittle to plastic transition in Carrara marble: Journal of Geophysical Research: Solid Earth, v. 94, p. 4129-4145, https://doi.org/10.1029/JB094iB04p04129.

Frye, K. M., and Marone, C., 2002, Effect of humidity on granular friction at room temperature, v. 107, p. ETG 11-1-ETG 11-13, https://doi.org/10.1029/2001JB000654.

Fukushima, Y., Toda, S., Miura, S., Ishimura, D., Fukuda, J. i., Demachi, T., and Tachibana, K., 2018, Extremely early recurrence of intraplate fault rupture following the Tohoku-Oki earthquake: Nature Geoscience, v. 11, p. 777-781, https://doi.org/10.1038/s41561-018-0201-x.

Giacomel, P., Ruggieri, R., Scuderi, M. M., Spagnuolo, E., Di Toro, G., and Collettini, C., 2021, Frictional properties of basalt experimental faults and implications for volcano-tectonic settings and geo-energy sites: Tectonophysics, v. 811,

https://doi.org/10.1016/j.tecto.2021.228883.

Gilbert, G. K., 1909, Earthquake forecasts introduction: Science, v. 29, p.121–138, https://doi.org/10.1126/science.29.734.1.

Goldsby, D. L., and Tullis, T. E., 2002, Low frictional strength of quartz rocks at subseismic slip rates: Geophysical Research Letters, v. 29, p. 25-21-25-24, https://doi.org/10.1029/2002GL015240.

Goldsby, D. L., and Tullis, T. E., 2011, Flash heating leads to low frictional strength of crustal rocks at earthquake slip rates: Science, v. 334, p. 216-218, https://doi.org/10.1126/science.1207902.

Gomila, R., Fondriest, M., Jensen, E., Spagnuolo, E., Masoch, S., Mitchell, T. M., Magnarini, G., Bistacchi, A., Mittempergher, S., Faulkner, D., Cembrano, J., and Di Toro, G., 2021, Frictional melting in hydrothermal fluid-rich faults: Field and experimental evidence from the Bolfín Fault Zone (Chile): Geochemistry, Geophysics, Geosystems, v. 22, https://doi.org/10.1029/2021GC009743.

Goswami, A., and Barbot, S., 2018, Slow-slip events in semi-brittle serpentinite fault zones: Scientific Reports, v. 8, https://doi.org/10.1038/s41598-018-24637-z.

Griggs, D., 1967, Hydrolytic weakening of quartz and other silicates: Geophysical Journal International, v. 14, p. 19-31, https://doi.org/10.1111/j.1365-246X.1967.tb06218.x.

Han, R., Hirose, T., and Shimamoto, T., 2010, Strong velocity weakening and powder lubrication of simulated carbonate faults at seismic slip rates: Journal of Geophysical Research: Solid Earth, v. 115, B03412, https://doi.org/10.1029/2008JB006136.

Han, R., Shimamoto, T., Hirose, T., Ree, J.-H., and Ando, J.-i., 2007, Ultralow friction of carbonate faults caused by thermal decomposition, v. 316, p. 878-881, https://doi.org/10.1126/science.1139763.

Handy, M., Hirth, G., and Hovius, N., 2007, Tectonic faults: MIT Press.

Harbord, C., Brantut, N., David, E. C., and Mitchell, T. M., 2022, A high pressure, high

temperature gas medium apparatus to measure acoustic velocities during deformation of rock: Review of Scientific Instruments, v. 93, p. 053908, https://doi.org/10.1063/5.0084477.

He, C., Luo, L., Hao, Q.-M., and Zhou, Y., 2013, Velocity-weakening behavior of plagioclase and pyroxene gouges and stabilizing effect of small amounts of quartz under hydrothermal conditions: Journal of Geophysical Research: Solid Earth, v. 118, p. 3408-3430, https://doi.org/10.1002/jgrb.50280.

He, C., Wang, Z. & Yao, W., 2007, Frictional sliding of gabbro gouge under hydrothermal conditions: Tectonophysics, v. 445, p. 353-362, https://doi.org/10.1016/j.tecto.2007.09.008.

He, C., Yao, W., Wang, Z., and Zhou, Y., 2006, Strength and stability of frictional sliding of gabbro gouge at elevated temperatures: Tectonophysics, v. 427, p. 217-229, https://doi.org/10.1016/j.tecto.2006.05.023.

Heaton, T. H., 1990, Evidence for and implications of self-healing pulses of slip in earthquake rupture: Physical of the Earth and Planetary Interiors. v. 64, p. 1-20, https://doi.org/10.1016/0031-9201(90)90002-F.

Heimpel, M., 1997, Critical behaviour and the evolution of fault strength during earthquake cycles: Nature, v. 388, p. 865-868, https://doi.org/10.1038/42232.

Heise, W., Caldwell, T. G., Bertrand, E. A., Hill, G. J., Bennie, S. L., and Ogawa, Y., 2013, Changes in electrical resistivity track changes in tectonic plate coupling: Geophysical Research Letters, v. 40, p. 5029-5033, https://doi.org/10.1002/grl.50959.

Hirose, T., and Shimamoto, T., 2005, Growth of molten zone as a mechanism of slip weakening of simulated faults in gabbro during frictional melting: Journal of Geophysical Research: Solid Earth, v. 110, B05202, https://doi.org/10.1029/2004JB003207.

Hunfeld, L. B., Chen, J., Hol, S., Niemeijer, A. R., and Spiers, C. J., 2020, Healing Behavior of Simulated Fault Gouges From the Groningen Gas Field and

Implications for Induced Fault Reactivation: Journal of Geophysical Research: Solid Earth, v. 125, p. e2019JB018790, https://doi.org/10.1029/2019JB018790.

Ikari, M. J., Marone, C., and Saffer, D. M., 2011, On the relation between fault strength and frictional stability: Geology, v. 39, p. 83-86, https://doi.org/10.1130/G31416.1.

Im, K., Elsworth, D., and Fang, Y., 2018, The influence of preslip sealing on the permeability evolution of fractures and faults: Geophysical Research Letters, v. 45, p. 166-175, https://doi.org/10.1002/2017GL076216.

Im, K., Elsworth, D., and Wang, C., 2019, Cyclic permeability evolution during repose then reactivation of fractures and faults: Journal of Geophysical Research: Solid Earth, v. 124, p. 4492-4506, https://doi.org/10.1029/2019JB017309.

Islam, M. T., Nabi, M. N., Arefin, M. A., Mostakim, K., Rashid, F., Hassan, N. M. S., Rahman, S. M. A., McIntosh, S., Mullins, B. J., and Muyeen, S. M., 2022, Trends and prospects of geothermal energy as an alternative source of power: A comprehensive review: Heliyon, v. 8, p. e11836, https://doi.org/10.1016/j.heliyon.2022.e11836.

Ito, Y., and Obara, K., 2006, Dynamic deformation of the accretionary prism excites very low frequency earthquakes: Geophysical Research Letters, v. 33, L02311, https://doi.org/10.1029/2005GL025270.

Kanakiya, S., Adam, L., Esteban, L., Rowe, M. C., and Shane, P., 2017, Dissolution and secondary mineral precipitation in basalts due to reactions with carbonic acid: Journal of Geophysical Research: Solid Earth, v. 122, p. 4312-4327, https://doi.org/10.1002/2017JB014019.

Karner, S. L., and Marone, C., 1998, The effect of shear load on frictional healing in simulated fault gouge, v. 25, p. 4561-4564, https://doi.org/10.1029/1998GL900182.

Kato, A., Iidaka, T., Ikuta, R., Yoshida, Y., Katsumata, K., Iwasaki, T., Sakai, S. i., Thurber, C., Tsumura, N., Yamaoka, K., Watanabe, T., Kunitomo, T., Yamazaki, F., Okubo, M., Suzuki, S., and Hirata, N., 2010, Variations of fluid pressure within

the subducting oceanic crust and slow earthquakes: Geophysical Research Letters, v. 37, L14310, https://doi.org/10.1029/2010GL043723.

King, D. S. H., and Marone, C., 2012, Frictional properties of olivine at high temperature with applications to the strength and dynamics of the oceanic lithosphere: Journal of Geophysical Research: Solid Earth, v. 117, https://doi.org/10.1029/2012JB009511.

Lapusta, N., and Rice, J. R., 2003, Nucleation and early seismic propagation of small and large events in a crustal earthquake model: Journal of Geophysical Research: Solid Earth, v. 108, B42005, https://doi.org/10.1029/2001JB000793.

Lavier, L. L., Tong, X., and Biemiller, J., 2021, The mechanics of creep, slow slip events, and earthquakes in mixed brittle-ductile fault zones: Journal of Geophysical Research: Solid Earth, v. 126, p. e2020JB020325, https://doi.org/10.1029/2020JB020325.

Leeman, J. R., Saffer, D. M., Scuderi, M. M., and Marone, C., 2016, Laboratory observations of slow earthquakes and the spectrum of tectonic fault slip modes: Nature Communications, v. 7, p. 11104, https://doi.org/10.1038/ncomms11104.

Li, Q., Tullis, T. E., Goldsby, D., and Carpick, R. W., 2011, Frictional ageing from interfacial bonding and the origins of rate and state friction: Nature, v. 480, p. 233-236, https://doi.org/10.1038/nature10589.

Li, Z., and Szlufarska, I., 2018, Multiphysics model of chemical aging in frictional contacts: Physical Review Materials, v. 2, https://doi.org/10.1103/PhysRevMaterials.2.063602.

Lisabeth, H. P., and Zhu, W., 2015, Effect of temperature and pore fluid on the strength of porous limestone: Journal of Geophysical Research: Solid Earth, v. 120, p. 6191-6208, https://doi.org/10.1002/2015JB012152.

Liu, Y., and Szlufarska, I., 2012, Chemical origins of frictional aging: Physical Review Letters, v. 109, p. 186102, https://doi.org/10.1103/PhysRevLett.109.186102.

Lockner, D. A., Byerlee, J. D., Kuksenko, V., Ponomarev, A., and Sidorin, A., 1991,

Quasi-static fault growth and shear fracture energy in granite: Nature, v. 350, p. 39-42, https://doi.org/10.1038/350039a0.

Lockner, D. A., Morrow, C., Moore, D. & Hickman, S., 2011, Low strength of deep San Andreas fault gouge from SAFOD core: Nature, v. 472, p. 82-85, https://doi.org/10.1038/nature09927.

Ma, S., Shimamoto, T., Yao, L., Togo, T. & Kitajima, H., 2014, A rotary-shear low to high-velocity friction apparatus in Beijing to study rock friction at plate to seismic slip rates: Earthquake Sciences, v. 27, p. 469-497, https://doi.org/10.1007/s11589-014-0097-5.

Marone, C., 1998, Laboratory-derived friction laws and their application to seismic faulting: Annual Review of Earth and Planetary Science, v. 26, p. 643-696, https://doi.org/10.1146/annurev.earth.26.1.643.

Marone, C., 1998, The effect of loading rate on static friction and the rate of fault healing during the earthquake cycle: Nature, v. 391, p. 69-72, https://doi.org/10.1038/34157.

Marone, C., and Saffer, D. M., 2007, 12. Fault friction and the upper transition from seismic to aseismic faulting, Columbia University Press, p. 346-369.

Marone, C., Vidale, J. E., and Ellsworth, W. L., 1995, Fault healing inferred from time dependent variations in source properties of repeating earthquakes: Geophysical Research Letters, v. 22, p. 3095-3098, https://doi.org/10.1029/95GL03076.

Masoch, S., Fondriest, M., Preto, N., Secco, M., and Di Toro, G., 2019, Seismic cycle recorded in cockade-bearing faults (Col de Teghime, Alpine Corsica): Journal of Structural Geology, v. 129, p. 103889, https://doi.org/10.1016/j.jsg.2019.103889.

Masoch, S., Gomila, R., Fondriest, M., Jensen, E., Mitchell, T., Pennacchioni, G., Cembrano, J., and Di Toro, G., 2021, Structural evolution of a crustal-scale seismogenic fault in a magmatic arc: The Bolfin Fault Zone (Atacama Fault System): Tectonics, v. 40, p. e2021TC006818, https://doi.org/10.1029/2021TC006818.

Mei, C., Barbot, S., and Wu, W., 2021, Period-multiplying cycles at the transition between stick-slip and stable sliding and implications for the Parkfield period-doubling tremors: Geophysical Research Letters, v. 48, p. e2020GL091807, https://doi.org/10.1029/2020GL091807.

Meyer, G. G., Brantut, N., Mitchell, T. M., and Meredith, P. G., 2019, Fault reactivation and strain partitioning across the brittle-ductile transition: Geology, v. 47, p. 1127-1130, https://doi.org/10.1130/G46516.1.

Michalske, T. A., and Freiman, S. W., 1982, A molecular interpretation of stress corrosion in silica: Nature, v. 295, p. 511-512, https://doi.org/10.1038/295511a0.

Mitchell, E. K., Fialko, Y. & Brown, K. M., 2015, Frictional properties of gabbro at conditions corresponding to slow slip events in subduction zones: Geochemistry, Geophysics, Geosystems, v. 16, p. 4006-4020, https://doi.org/10.1002/2015gc006093.

Mitchell, E. K., Fialko, Y., and Brown, K. M., 2013, Temperature dependence of frictional healing of Westerly granite: Experimental observations and numerical simulations: Geochemistry, Geophysics, Geosystems, v. 14, p. 567-582, https://doi.org/10.1029/2012GC004241.

Mitchell, T. M., and Faulkner, D. R., 2009, The nature and origin of off-fault damage surrounding strike-slip fault zones with a wide range of displacements: A field study from the Atacama fault system, northern Chile: Journal of Structural Geology, v. 31, p. 802-816, https://doi.org/10.1016/j.jsg.2009.05.002.

Mitchell, T. M., and Faulkner, D. R., 2012, Towards quantifying the matrix permeability of fault damage zones in low porosity rocks: Earth and Planetary Science Letters, v. 339-340, p. 24-31, https://doi.org/10.1016/j.epsl.2012.05.014.

Mizoguchi, K., Takahashi, M., Masuda, K. & Fukuyama, E., 2007, Fault strength drop due to phase transitions in the pore fluid: Geophysical Research Letters, v. 34, L09313, https://doi.org/10.1029/2007GL029345.

Moore, D. E. & Lockner, D. A., 2013, Chemical controls on fault behavior: Weakening

of serpentinite sheared against quartz-bearing rocks and its significance for fault creep in the San Andreas system: Journal of Geophysical Research: Solid Earth, v. 118, p. 2558-2570, https://doi.org/10.1002/jgrb.50140.

Moore, D. E. & Rymer, M. J., 2007, Talc-bearing serpentinite and the creeping section of the San Andreas fault: Nature, v. 448, p. 795-797, https://doi.org/10.1038/nature06064.

Moore, D. E., and Lockner, D. A., 2007, Friction of the smectite clay montmorillonite: A review and interpretation of data: Columbia University Press, p. 317-345, https://doi.org/10.7312/dixo13866-011.

Moore, D. E., and Lockner, D. A., 2008, Talc friction in the temperature range 25°–400 °C: Relevance for Fault-Zone Weakening: Tectonophysics, v. 449, p. 120-132, https://doi.org/10.1016/j.tecto.2007.11.039.

Moore, D. E., and Lockner, D. A., 2013, Chemical controls on fault behavior: Weakening of serpentinite sheared against quartz-bearing rocks and its significance for fault creep in the San Andreas system: Journal of Geophysical Research: Solid Earth, v. 118, p. 2558-2570, https://doi.org/10.1002/jgrb.50140.

Moore, D. E., and Lockner, D. A., 2021, Weakening of peridotite sheared at hydrothermal conditions: Geochemistry, Geophysics, Geosystems, v. 22, p. e2021GC010005, https://doi.org/10.1029/2021GC010005.

Moore, D. E., Lockner, D. A., Summers, R., Shengli, M., and Byerlee, J. D., 1996, Strength of chrysotile-serpentinite gouge under hydrothermal conditions: Can it explain a weak San Andreas fault?: Geology, v. 24, p. 1041-1044, https://doi.org/10.1130/0091-7613(1996)024<1041:SOCSGU>2.3.CO;2.

Moore, J. C., and Saffer, D., 2001, Updip limit of the seismogenic zone beneath the accretionary prism of southwest Japan: An effect of diagenetic to low-grade metamorphic processes and increasing effective stress: Geology, v. 29, p. 183-186, https://doi.org/10.1130/0091-7613(2001)029<0183:ULOTSZ>2.0.CO;2.

Morey, G.W., 1957, The solubility of solids in gases: Economic Geology, v. 52, p. 225-

251, https://doi.org/10.2113/gsecongeo.52.3.225.

Morrow, C. A., Moore, D. E., and Lockner, D. A., 2000, The effect of mineral bond strength and adsorbed water on fault gouge frictional strength: Geophysical Research Letters, v. 27, p. 815-818, https://doi.org/10.1029/1999GL008401.

Morrow, C. A., Moore, D. E., and Lockner, D. A., 2017, Frictional strength of wet and dry montmorillonite: Journal of Geophysical Research: Solid Earth, v. 122, p. 3392-3409, https://doi.org/10.1002/2016JB013658.

Muhuri, S. K., Dewers, T. A., Scott, T. E., Jr., and Reches, Z. e., 2003, Interseismic fault strengthening and earthquake-slip instability: Friction or cohesion?: Geology, v. 31, p. 881-884, https://doi.org/10.1130/G19601.1.

Mukuhira, Y., Asanuma, H., Niitsuma, H., Häring, M., and Deichmann, N., 2010, Estimation of source parameter of microseismic events with large magnitude collected at basel, switzerland in 2006: Geothermal Resources Council Transactions, v. 34, p. 375–380.

Nakatani, M., and Scholz, C. H., 2004, Frictional healing of quartz gouge under hydrothermal conditions: 1. Experimental evidence for solution transfer healing mechanism: Journal of Geophysical Research: Solid Earth, v. 109, B07201, https://doi.org/10.1029/2001JB001522.

Nielsen, S., Di Toro, G., Hirose, T., and Shimamoto, T., 2008, Frictional melt and seismic slip, v. 113, B01308, https://doi.org/10.1029/2007JB005122.

Nielsen, S., Spagnuolo, E., Violay, M. & Di Toro, G., 2021, Thermal weakening friction during seismic slip: Experiments and models with heat sources and sinks: Journal of Geophysical Research: Solid Earth, v. 126, e2020JB020652, https://doi.org/10.1029/2020jb020652.

Niemeijer, A. R., Boulton, C., Toy, V. G., Townend, J., and Sutherland, R., 2016, Large-displacement, hydrothermal frictional properties of DFDP-1 fault rocks, Alpine Fault, New Zealand: Implications for deep rupture propagation: Journal of Geophysical Research: Solid Earth, v. 121, p. 624-647,

https://doi.org/10.1002/2015JB012593.

Niemeijer, A. R., Di Toro, G., Griffith, W. A., Bistacchi, A., Smith, S. A. F., and Nielsen, S., 2012, Inferring earthquake physics and chemistry using an integrated field and laboratory approach: Journal of Structural Geology, v. 39, p. 2-36, https://doi.org/10.1016/j.jsg.2012.02.018.

Niemeijer, A. R., Di Toro, G., Nielsen, S., and Di Felice, F., 2011, Frictional melting of gabbro under extreme experimental conditions of normal stress, acceleration, and sliding velocity: Journal of Geophysical Research, v. 116, B07404, https://doi.org/10.1029/2010JB008181.

Niemeijer, A. R., Marone, C. & Elsworth, D., 2008, Healing of simulated fault gouges aided by pressure solution: Results from rock analogue experiments: Journal of Geophysical Research: Solid Earth, v. 113, B04204, https://doi.org/10.1029/2007JB005376.

Niemeijer, A. R., Marone, C., and Elsworth, D., 2010, Fabric induced weakness of tectonic faults: Geophysical Research Letters, v. 37, L03304, https://doi.org/10.1029/2009GL041689.

Niemeijer, A. R., Spiers, C. J., and Peach, C. J., 2008, Frictional behaviour of simulated quartz fault gouges under hydrothermal conditions: Results from ultra-high strain rotary shear experiments: Tectonophysics, v. 460, p. 288-303, https://doi.org/10.1016/j.tecto.2008.09.003.

Nishimura, T., and Thatcher, W., 2003, Rheology of the lithosphere inferred from postseismic uplift following the 1959 Hebgen Lake earthquake: Journal of Geophysical Research: Solid Earth, v. 108, https://doi.org/10.1029/2002JB002191.

Noda, H., and Lapusta, N., 2013, Stable creeping fault segments can become destructive as a result of dynamic weakening: Nature, v. 493, p. 518-521, https://doi.org/10.1038/nature11703.

Noda, H., and Shimamoto, T., 2005, Thermal pressurization and slip-weakening distance of a fault: An example of the hanaore fault, southwest Japan: Bulletin of

the Seismological Society of America, v. 95, p. 1224-1233, https://doi.org/10.1785/0120040089.

Noël, C., Passelègue, F. X., and Violay, M., 2021, Brittle faulting of ductile rock induced by pore fluid pressure build-up: Journal of Geophysical Research: Solid Earth, v. 126, p. e2020JB021331, https://doi.org/10.1029/2020JB021331.

Noël, C., Giorgetti, C., Scuderi, M. M., Collettini, C., and Marone, C., 2023, The Effect of Shear Displacement and Wear on Fault Stability: Laboratory Constraints: Journal of Geophysical Research: Solid Earth, v. 128, https://doi.org/10.1029/2022JB026191.

Ohnaka, M., 2013, The physics of rock failure and earthquakes: Cambridge University Press, https://doi.org/10.1017/CBO9781139342865.

Okamoto, A. S., Niemeijer, A. R., Takeshita, T., Verberne, B. A. & Spiers, C. J., 2020, Frictional properties of actinolite-chlorite gouge at hydrothermal conditions: Tectonophysics, v. 779, 228377, https://doi.org/10.1016/j.tecto.2020.228377.

Okamoto, A. S., Verberne, B. A., Niemeijer, A. R., Takahashi, M., Shimizu, I., Ueda, T., and Spiers, C. J., 2019, Frictional properties of simulated chlorite gouge at hydrothermal conditions: Implications for subduction megathrusts: Journal of Geophysical Research: Solid Earth, v. 124, p. 4545-4565, https://doi.org/10.1029/2018JB017205.

Okuda, H., Niemeijer, A. R., Takahashi, M., Yamaguchi, A. & Spiers, C. J., 2023, Hydrothermal friction experiments on simulated basaltic fault gouge and implications for megathrust earthquakes: Journal of Geophysical Research: Solid Earth, v. 128, e2022JB025072, https://doi.org/10.1029/2022JB025072.

Orowan, E., 1944, The fatigue of glass under stress: Nature, v. 154, p. 341-343, https://doi.org/10.1038/154341a0.

Ouyang, W., and Urbakh, M., 2022, Microscopic mechanisms of frictional aging: Journal of the Mechanics and Physics of Solids, v. 166, https://doi.org/10.1016/j.jmps.2022.104944.

Park, J.-O., Fujie, G., Wijerathne, L., Hori, T., Kodaira, S., Fukao, Y., Moore, G. F., Bangs, N. L., Kuramoto, S. i., and Taira, A., 2010, A low-velocity zone with weak reflectivity along the Nankai subduction zone: Geology, v. 38, p. 283-286, https://doi.org/10.1130/G30205.1.

Paterson, M. S., 1958, Experimental deformation and faulting in Wombeyan marble: GSA Bulletin, v. 69, p. 465-476, https://doi.org/10.1130/0016-7606(1958)69[465:EDAFIW]2.0.CO;2.

Paterson, M. S., and Weaver, C. W., 1970, Deformation of polycrystalline MgO under pressure: Journal of the American Ceramic Society, v. 53, no. 8, p. 463-471, https://doi.org/10.1111/j.1151-2916.1970.tb12678.x.

Peacock, S. M., Christensen, N. I., Bostock, M. G., and Audet, P., 2011, High pore pressures and porosity at 35 km depth in the Cascadia subduction zone: Geology, v. 39, p. 471-474, https://doi.org/10.1130/G31649.1.

Perrin, G., Rice, J. R., and Zheng, G., 1995, Self-healing slip pulse on a frictional surface: Journal of the Mechanics and Physics of Solids, v. 43, p. 1461-1495, https://doi.org/10.1016/0022-5096(95)00036-I.

Phillips, N. J., Belzer, B., French, M. E., Rowe, C. D., and Ujiie, K., 2020, Frictional strengths of subduction thrust rocks in the region of shallow slow earthquakes: Journal of Geophysical Research: Solid Earth, v. 125, p. e2019JB018888, https://doi.org/10.1029/2019JB018888.

Piana Agostinetti, N. et al., 2017, Discovering geothermal supercritical fluids: a new frontier for seismic exploration: Scientific Reports, v. 7, p. 14592, https://doi.org/10.1038/s41598-017-15118-w.

Pollitz, F. F., 2015, Postearthquake relaxation evidence for laterally variable viscoelastic structure and water content in the Southern California mantle: Journal of Geophysical Research: Solid Earth, v. 120, p. 2672-2696, https://doi.org/10.1002/2014JB011603.

Pozzi, G., De Paola, N., Nielsen, S. B., Holdsworth, R. E., Tesei, T., Thieme, M., and

Demouchy, S., 2021, Coseismic fault lubrication by viscous deformation: Nature Geoscience, v. 14, https://doi.org/10.1038/s41561-021-00747-8.

Raleigh, C. B., Healy, J. H., and Bredehoeft, J. D., 1972, Faulting and crustal stress at Rangely, Colorado, p. 275-284, https://doi.org/10.1029/GM016p0275.

Raleigh, C. B., Healy, J. H., and Bredehoeft, J. D., 1976, An experiment in earthquake control at Rangely, Colorado: Science, v. 191, p. 1230-1237, https://doi.org/10.1126/science.191.4233.1230.

Reches, Z., and Lockner, D. A., 2010, Fault weakening and earthquake instability by powder lubrication: Nature, v. 467, p. 452-455, https://doi.org/10.1038/nature09348.

Rempe, M., Di Toro, G., Mitchell, T. M., Smith, S. A. F., Hirose, T., and Renner, J., 2020, Influence of effective stress and pore fluid pressure on fault strength and slip localization in carbonate slip zones: Journal of Geophysical Research: Solid Earth, v. 125, p. e2020JB019805, https://doi.org/10.1029/2020JB019805.

Rice, J. R., 1993, Spatio-temporal complexity of slip on a fault: Journal of Geophysical Research: Solid Earth, v. 98, p. 9885-9907, https://doi.org/10.1029/93JB00191.

Rice, J. R., 2006, Heating and weakening of faults during earthquake slip: Journal of Geophysical Research: Solid Earth, v. 111, B05311, https://doi.org/10.1029/2005JB004006.

Rice, J. R., 2006, Heating and weakening of faults during earthquake slip: Journal of Geophysical Research: Solid Earth, v. 111, https://doi.org/10.1029/2005JB004006.

Richardson, E., and Marone, C., 1999, Effects of normal stress vibrations on frictional healing: Journal of Geophysical Research: Solid Earth, v. 104, p. 28859-28878, https://doi.org/10.1029/1999JB900320.

Roeloffs, E. A., 2006, Evidence for aseismic deformation rate changes prior to earthquakes: Annual Review of Earth and Planetary Sciences, v. 34, p. 591-627, https://doi.org/10.1146/annurev.earth.34.031405.124947.

Rolandone, F., Bürgmann, R., and Nadeau, R. M., 2004, The evolution of the seismic-

aseismic transition during the earthquake cycle: Constraints from the time-dependent depth distribution of aftershocks: Geophysical Research Letters, v. 31, L23610, https://doi.org/10.1029/2004GL021379.

Ross, Z. E., Cochran, E. S., Trugman, D. T. & Smith, J. D., 2020, 3D fault architecture controls the dynamism of earthquake swarms: Science, v. 368, p. 1357-1361, https://doi.org/10.1126/science.abb0779.

Ruina, A., 1983, Slip instability and state variable friction laws: Journal of Geophysical Research: Solid Earth, v. 88, p. 10359-10370, https://doi.org/10.1029/JB088iB12p10359.

Rutter, E. H., 1972, The influence of interstitial water on the rheological behaviour of calcite rocks: Tectonophysics, v. 14, p. 13-33, https://doi.org/10.1016/0040-1951(72)90003-0.

Rutter, E. H., 1986, On the nomenclature of mode of failure transitions in rocks: Tectonophysics, v. 122, p. 381-387, https://doi.org/10.1016/0040-1951(86)90153-8.

Saffer, D. M., and Marone, C., 2003, Comparison of smectite- and illite-rich gouge frictional properties: application to the updip limit of the seismogenic zone along subduction megathrusts: Earth and Planetary Science Letters, v. 215, p. 219-235, https://doi.org/10.1016/S0012-821X(03)00424-2.

Savage, H. M., and Brodsky, E. E., 2011, Collateral damage: Evolution with displacement of fracture distribution and secondary fault strands in fault damage zones: Journal of Geophysical Research: Solid Earth, v. 116, B03405, https://doi.org/10.1029/2010JB007665.

Schaff, D. P., Bokelmann, G. H. R., Beroza, G. C., Waldhauser, F., and Ellsworth, W. L., 2002, High-resolution image of Calaveras Fault seismicity: Journal of Geophysical Research: Solid Earth, v. 107, no. B9, p. ESE 5-1-ESE 5-16, https://doi.org/10.1029/2001JB000633.

Scholz, C. H., 1998, Earthquakes and friction laws: Nature, v. 391, p. 37-42,

https://doi.org/10.1038/34097.

Scholz, C. H., 2019, The Mechanics of Earthquakes and Faulting: Cambridge University Press.

Schott, J., Pokrovsky, O. S., and Oelkers, E. H., 2009, The link between mineral dissolution/precipitation kinetics and solution chemistry: Reviews in Mineralogy and Geochemistry, v. 70, p. 207-258, https://doi.org/10.2138/rmg.2009.70.6.

Seki, T. et al., 2020, The bending mode of water: A powerful probe for hydrogen bond structure of aqueous systems: The Journal of Physical Chemistry Letters, v. 11, p. 8459-8469, https://doi.org/10.1021/acs.jpclett.0c01259.

Shelly, D. R., and Hardebeck, J. L., 2010, Precise tremor source locations and amplitude variations along the lower-crustal central San Andreas Fault: Geophysical Research Letters, v. 37, https://doi.org/10.1029/2010GL043672.

Shelly, D. R., Beroza, G. C., Ide, S., and Nakamula, S., 2006, Low-frequency earthquakes in Shikoku, Japan, and their relationship to episodic tremor and slip: Nature, v. 442, p. 188-191, https://doi.org/10.1038/nature04931.

Shimamoto, T., 1986, Transition between frictional slip and ductile flow for halite shear zones at room temperature: Science, v. 23, p. 711-714, https://doi.org/10.1126/science.231.4739.711.

Shimamoto, T., 2022, Hydrothermal experimental system for UNIPD friction apparatus [TS Hydrothermal PV-2020] background, description & specifications, and scope.

Shimamoto, T., and Noda, H., 2014, A friction to flow constitutive law and its application to a 2-D modeling of earthquakes: Journal of Geophysical Research: Solid Earth, v. 119, p. 8089-8106, https://doi.org/10.1002/2014JB011170.

Shipton, Z. K., and Cowie, P. A., 2001, Damage zone and slip-surface evolution over μm to km scales in high-porosity Navajo sandstone, Utah: Journal of Structural Geology, v. 23, p. 1825-1844, https://doi.org/10.1016/S0191-8141(01)00035-9.

Sibson, R. H., 1973, Interactions between temperature and pore-fluid pressure during earthquake faulting and a mechanism for partial or total stress relief: Nature

Physical Science, v. 243, p. 66-68, https://doi.org/10.1038/physci243066a0.

Sibson, R. H., 1977, Fault rocks and fault mechanisms: Journal of the Geological Society, v. 133, p. 191-213, https://doi.org/10.1144/gsjgs.133.3.0191.

Sibson, R. H., 1982, Fault zone models, heat flow, and the depth distribution of earthquakes in the continental crust of the United States: Bulletin of the Seismological Society of America, v. 72, p. 151-163, https://doi.org/10.1785/BSSA0720010151.

Sibson, R. H., 1984, Roughness at the base of the seismogenic zone: Contributing factors: Journal of Geophysical Research: Solid Earth, v. 8, p. 5791-5799, https://doi.org/10.1029/JB089iB07p05791.

Sibson, R. H., 2020, Preparation zones for large crustal earthquakes consequent on fault-valve action: Earth, Planets and Space, v. 72, p. 31, https://doi.org/10.1186/s40623-020-01153-x.

Sibson, R. H., and Rowland, J. V., 2003, Stress, fluid pressure and structural permeability in seismogenic crust, North Island, New Zealand: Geophysical Journal International, v. 154, p. 584-594, https://doi.org/10.1046/j.1365-246X.2003.01965.x.

Sone, H., Shimamoto, T. & Moore, D. E., 2012, Frictional properties of saponite-rich gouge from a serpentinite-bearing fault zone along the Gokasho-Arashima Tectonic Line, central Japan: Journal of Structure Geology, v. 38, p. 172-182, https://doi.org/10.1016/j.jsg.2011.09.007.

Spagnuolo, E., Nielsen, S., Violay, M., and Di Toro, G., 2016, An empirically based steady state friction law and implications for fault stability: Geophysical Research Letters, v. 43, p. 3263-3271, https://doi.org/10.1002/2016GL067881.

Stesky, R. M., 1978, Mechanisms of high temperature frictional sliding in Westerly granite: Canadian Journal of Earth Sciences, v. 15, p. 361-375, https://doi.org/10.1139/e78-04.

Stesky, R. M., Brace, W. F., Riley, D. K. & Robin, P. Y. F.,1974, Friction in faulted rock

at high temperature and pressure: Tectonophysics, v. 23, p. 177-203, https://doi.org/10.1016/0040-1951(74)90119-X.

Stipp, M., Stünitz, H., Heilbronner, R., and Schmid, S. M., 2002, The eastern Tonale fault zone: a 'natural laboratory' for crystal plastic deformation of quartz over a temperature range from 250 to 700°C: Journal of Structural Geology, v. 24, p. 1861-1884, https://doi.org/10.1016/S0191-8141(02)00035-4.

Tape, C., Holtkamp, S., Silwal, V., Hawthorne, J., Kaneko, Y., Ampuero, J. P., Ji, C., Ruppert, N., Smith, K., and West, M. E., 2018, Earthquake nucleation and fault slip complexity in the lower crust of central Alaska: Nature Geoscience, v. 11, p. 536-541, https://doi.org/10.1038/s41561-018-0144-2.

Tesei, T., Collettini, C., Carpenter, B. M., Viti, C., and Marone, C., 2012, Frictional strength and healing behavior of phyllosilicate-rich faults: Journal of Geophysical Research: Solid Earth, v. 117, https://doi.org/10.1029/2012JB009204.

Tesei, T., Lacroix, B., and Collettini, C., 2015, Fault strength in thin-skinned tectonic wedges across the smectite-illite transition: Constraints from friction experiments and critical tapers: Geology, v. 43, p. 923-926, https://doi.org/10.1130/G36978.1.

Tobin, H. J., and Saffer, D. M., 2009, Elevated fluid pressure and extreme mechanical weakness of a plate boundary thrust, Nankai Trough subduction zone: Geology, v. 37, p. 679-682, https://doi.org/10.1038/s41561-018-0144-2.

Togo, T. et al., 2015, Stick–slip behavior of Indian gabbro as studied using a NIED large-scale biaxial friction apparatus: Earthquake Science, v. 28, p. 97-118, https://doi.org/10.1007/s11589-015-0113-4.

Tse, S. T., and Rice, J. R., 1986, Crustal earthquake instability in relation to the depth variation of frictional slip properties: Journal of Geophysical Research: Solid Earth, v. 91, p. 9452-9472, https://doi.org/10.1029/JB091iB09p09452.

Tsutsumi, A. & Shimamoto, T., 1997, High-velocity frictional properties of gabbro: Geophysical Research Letters, v. 24, p. 699-702, https://doi.org/10.1029/97gl00503.

Tsutsumi, A., and Mizoguchi, K., 2007, Effect of melt squeezing rate on shear stress along a simulated fault in gabbro during frictional melting: Geophysical Research Letters, v. 34, https://doi.org/10.1029/2007GL031565.

Tullis, J., and Yund, R. A., 1980, Hydrolytic weakening of experimentally deformed Westerly granite and Hale albite rock: Journal of Structural Geology, v. 2, p. 439-451, https://doi.org/10.1016/0191-8141(80)90005-X.

Tullis, T. E., 2015, Mechanisms for friction of rock at earthquake slip rates: Treatise on Geophysics, v. 4, p. 139-159, https://doi.org/10.1016/B978-0-444-53802-4.00073-7.

Tullis, T. E., 2015, Mechanisms for friction of rock at earthquake slip rates, Treatise on Geophysics, p. 139-159, https://doi.org/10.1016/B978-0-444-53802-4.00073-7.

Verberne, B. A., Niemeijer, A. R., De Bresser, J. H. P., and Spiers, C. J., 2015, Mechanical behavior and microstructure of simulated calcite fault gouge sheared at 20–600°C: Implications for natural faults in limestones: Journal of Geophysical Research: Solid Earth, v. 120, p. 8169-8196, https://doi.org/10.1002/2015JB012292.

Verberne, B. A., Niemeijer, A. R., De Bresser, J. H. P., and Spiers, C. J., 2015, Mechanical behavior and microstructure of simulated calcite fault gouge sheared at 20–600°C: Implications for natural faults in limestones: Journal of Geophysical Research: Solid Earth, v. 120, p. 8169-8196, https://doi.org/10.1002/2015JB012292.

Verberne, B. A., Plumper, O., de Winter, D. A., and Spiers, C. J., 2014, Rock mechanics. Superplastic nanofibrous slip zones control seismogenic fault friction: Science, v. 346, p. 1342-1344, https://doi.org/10.1126/science.1259003.

Violay, M. et al., 2014, Effect of water on the frictional behavior of cohesive rocks during earthquakes: Geology, v. 42, p. 27-30, https://doi.org/10.1130/g34916.1.

Violay, M., Gibert, B., Mainprice, D., and Burg, J.-P., 2015, Brittle versus ductile deformation as the main control of the deep fluid circulation in oceanic crust:

Geophysical Research Letters, v. 42, p. 2767-2773, https://doi.org/10.1002/2015GL063437.

Violay, M., Giorgetti, C., Cornelio, C., Aeschiman, F., Di Stefano, G., Gastaldo, L., and Wiemer, S., 2021, HighSTEPS: A high strain temperature pressure and speed apparatus to study earthquake mechanics: Rock Mechanics and Rock Engineering, v. 54, p. 2039-2052, https://doi.org/10.1007/s00603-021-02362-w.

Violay, M., Nielsen, S., Gibert, B., Spagnuolo, E., Cavallo, A., Azais, P., Vinciguerra, S., and Di Toro, G., 2013, Effect of water on the frictional behavior of cohesive rocks during earthquakes: Geology, v. 42, p. 27-30, https://doi.org/10.1130/G34916.1.

Weatherley, D. K. & Henley, R. W., 2013, Flash vaporization during earthquakes evidenced by gold deposits: Nature Geoscience, v. 6, p. 294-298, https://doi.org/10.1038/ngeo1759.

Wibberley, C. A. & Shimamoto, T., 2005, Earthquake slip weakening and asperities explained by thermal pressurization: Nature, v. 436, p. 689-692, https://doi.org/10.1038/nature03901.

Wimpenny, S., Forrest, N., and Copley, A., 2022, Time-dependent decrease in fault strength in the 2011–2016 Ibaraki–Fukushima earthquake sequence: Geophysical Journal International, v. 232, p. 788-809, https://doi.org/10.1093/gji/ggac368.

Wintsch, R. P., Christoffersen, R., and Kronenberg, A. K., 1995, Fluid-rock reaction weakening of fault zones: Journal of Geophysical Research: Solid Earth, v. 100, p. 13021-13032, https://doi.org/10.1029/94JB02622.

Yao, L., Ma, S., Platt, J. D., Niemeijer, A. R., and Shimamoto, T., 2016, The crucial role of temperature in high-velocity weakening of faults: Experiments on gouge using host blocks with different thermal conductivities: Geology, v. 44, p. 63-66, https://doi.org/10.1130/G37310.1.

Yasuhara, H., Marone, C., and Elsworth, D., 2005, Fault zone restrengthening and frictional healing: The role of pressure solution: Journal of Geophysical Research:

Solid Earth, v. 110, https://doi.org/10.1029/2004JB003327.

Yu, C.-C. et al., 2020, Vibrational couplings and energy transfer pathways of water's bending mode: Nature Communications, v. 11, 5977, https://doi.org/10.1038/s41467-020-19759-w.

Yukutake, Y., Ito, H., Honda, R., Harada, M., Tanada, T., and Yoshida, A., 2011, Fluid-induced swarm earthquake sequence revealed by precisely determined hypocenters and focal mechanisms in the 2009 activity at Hakone volcano, Japan: Journal of Geophysical Research: Solid Earth, v. 116, https://doi.org/10.1029/2010JB008036.

Zhang, L., and He, C., 2016, Frictional properties of phyllosilicate-rich mylonite and conditions for the brittle-ductile transition: Journal of Geophysical Research: Solid Earth, v. 121, p. 3017-3047, https://doi.org/10.1002/2015JB012489.

Zhang, L., He, C., Liu, Y., and Lin, J., 2017, Frictional properties of the South China Sea oceanic basalt and implications for strength of the Manila subduction seismogenic zone: Marine Geology, v. 394, p. 16-29, https://doi.org/10.1016/j.margeo.2017.05.006.

Zhang, X., and Spiers, C. J., 2005, Compaction of granular calcite by pressure solution at room temperature and effects of pore fluid chemistry: International Journal of Rock Mechanics and Mining Sciences, v. 42, p. 950-960, https://doi.org/10.1016/j.ijrmms.2005.05.017.

Zhu, T., Li, J., Lin, X., and Yip, S., 2005, Stress-dependent molecular pathways of silica–water reaction: Journal of the Mechanics and Physics of Solids, v. 53, p. 1597-1623, https://doi.org/10.1016/j.jmps.2005.02.002.

Appendices

Appendix A Preliminary data on frictional healing in basalt-built gouges

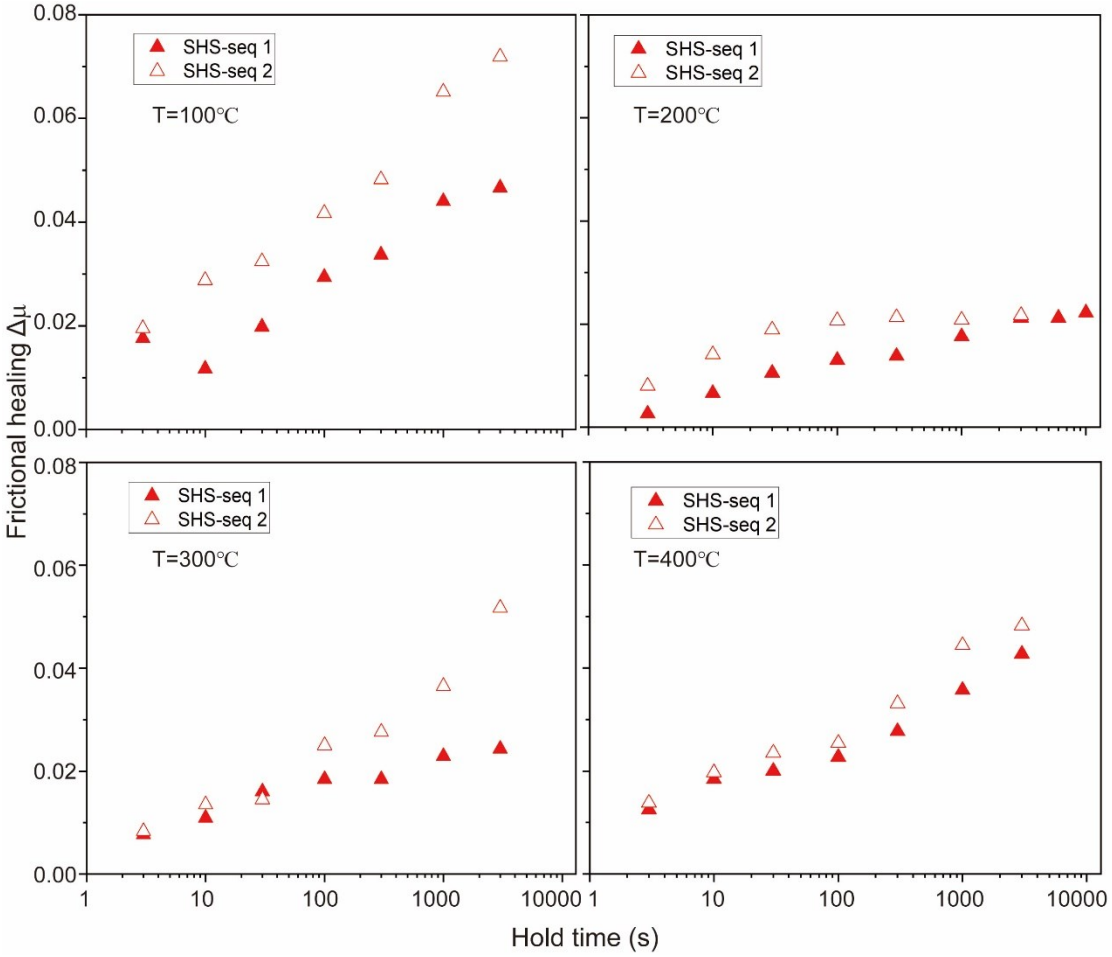

Figure A.1: Dry conditions experiments: frictional healing data ($\Delta\mu$) of basalt at temperatures from 100°C to 400°C. $\Delta\mu$ increases linearly with the logarithm of hold time in both sequences except for the 2nd sequence at T=200°C.

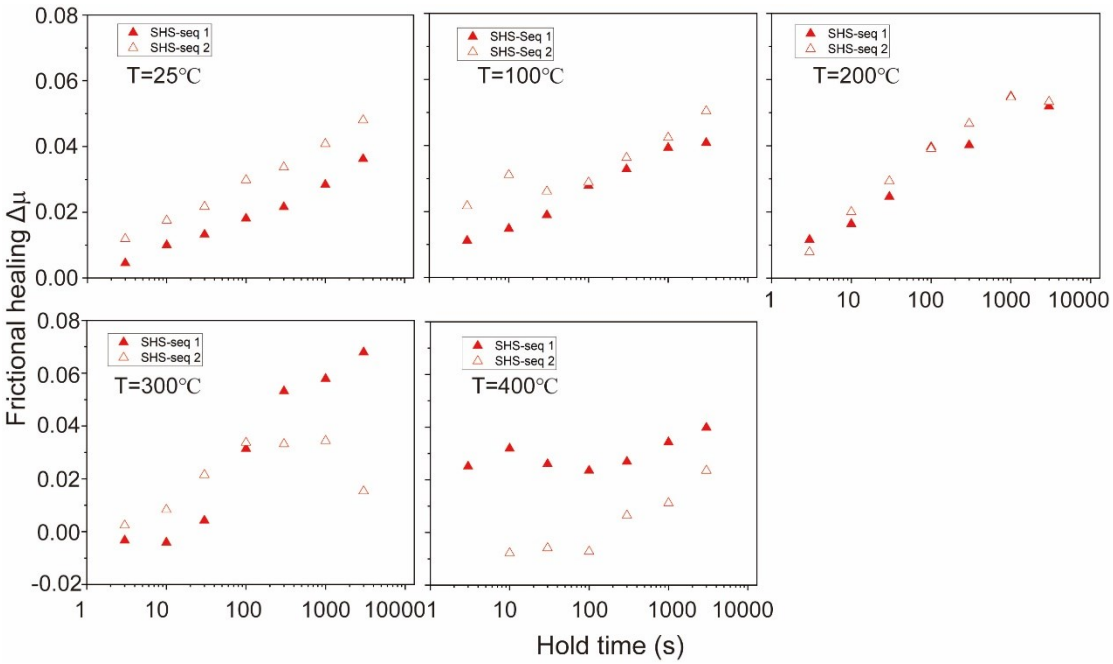

Figure A.2: Pressurized water experiments: frictional healing data ($\Delta\mu$) of basalt at P_p=30 MPa and temperatures from 25℃ to 400℃. At $T \leq 200$℃, frictional healing increases linearly with the logarithm of hold time (t_h). At $T \geq 300$℃, the linear relation between $\Delta\mu$ and log t_h does not hold. This observation is similar to that of gabbro.

Appendix B High-velocity frictional properties of gabbro- and marble-built faults under hydrothermal conditions

Lu Yao[1*], **Wei Feng**[2], Shengli Ma[1], Toshihiko Shimamoto[1], Giulio Di Toro[2]

[1]*State Key Laboratory of Earthquake Dynamics, Institute of Geology, China Earthquake Administration, Beijing 100029, China*

[2]*Dipartimento di Geoscienze, University of Padua, Padua, Italy*

B.1 Methods

The low- to high-velocity rotary shear apparatus we use (Ma et al., 2014) has a newly-equipped externally-heated pressure vessel capable of fulfilling hydrothermal conditions with temperatures up to 500 °C and pore fluid pressure up to 70 MPa. The basic design of the vessel is introduced in Chapter 2 (originally designed by Shimamoto Earth & Environment Laboratory Ltd., manufactured by TOYO KOATSU Co. Ltd).

The tested rock samples include Carrara marble and gabbro collected from Jinan, east China (Jinan gabbro). For sample preparation, after machining a perfect rock cylinder, we make a ring-shaped slip surface (16/28 mm internal/external diameter) by lathing a 2-mm-deep hollow in the center of one end surface (Figure B.1). Two parallel surfaces on the periphery of the other side of the cylinder are machined for the purpose of torque transmission. To prevent the tensile failure of rocks in experiments, Nickel rings are made to tightly fit around the rock specimens near the slip surfaces.

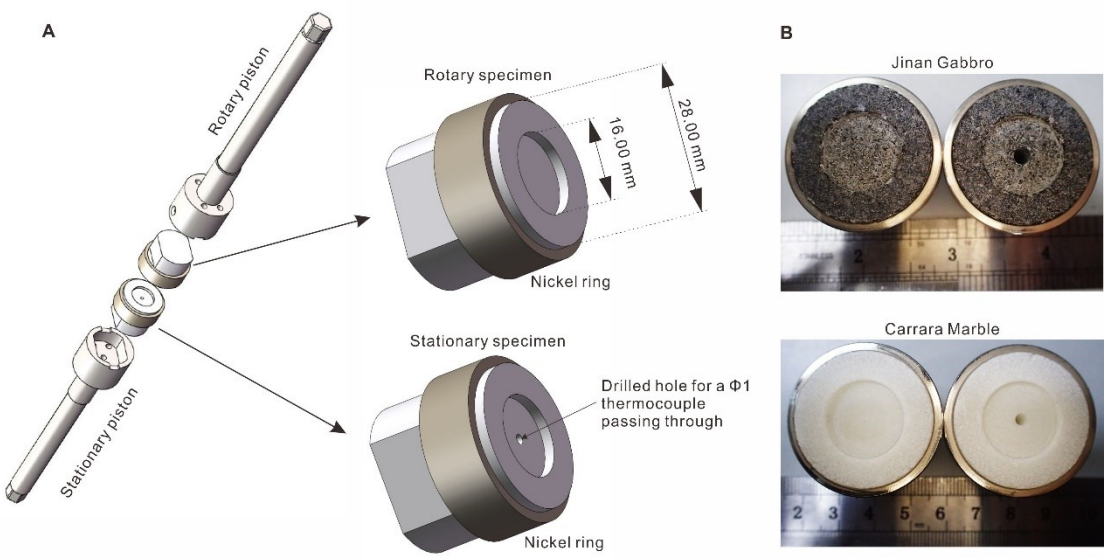

Figure B.1: Sample assembly in friction experiments. **A.** Schematic diagram of the sample assembly. **B.** Photos of the gabbro and marble samples

The friction experiments were conducted at effective normal stress (σ_{eff}) of 10 MPa and equivalent slip velocity (V_{eq}) of 1.5 m/s. The imposed temperature (T) ranged from 40 to 400 °C, and the pore pressure (P_p) was mostly 30 MPa, with 5 or 50 MPa in a few experiments.

B.2 Results

Mechanical Data

Eleven experiments were performed under the same σ_{eff} (10 MPa) and initial P_p (30 MPa) but various initial ambient T of 40–400 °C. The pressure vessel was isolated from the syringe pump before the initiation of sliding in all the experiments except for one run at T = 400 °C (marked with NI—no isolation—in Figure B.2).

Figures B.2A–D show the evolution of friction coefficient (μ) and axial displacement with slip displacement (d) from these experiments. Peak friction coefficients (μ_p) range from 0.404 to 0.491 for Jinan gabbro, and from 0.371 to 0.449 for Carrara marble respectively, almost independent of ambient T. The dynamic weakening processes and the steady-state friction coefficients (μ_{ss}) are conspicuously affected by ambient T

(Figures B.2A-B). For both gabbro and marble, higher ambient T yields smaller μ_{ss}. However, ambient T seems to play distinct roles in the weakening during the first 0.6 m of slip, i.e., promoting the initial weakening for gabbro versus delaying the weakening for marble. Differences also exist between the two rocks in the strength recovery during the deceleration phase. More recovery of friction can be observed for marble. The recovery of friction dwindles with increasing temperature for gabbro and even becomes negligible at T = 300 and 400 °C (cp. Figures B.2A-B). Moreover, whether isolating the pump and the vessel only brings a negligible effect on gabbro weakening (cp. red and cyan lines in Figures B.2A). In addition, for gabbro, the axial shortening reduces from ~1 mm at T = 40 °C to < 0.25 mm at $T \geq$ 200 °C, in contrast to almost no shortening at various T for marble (cp. Figures B.2C-D).

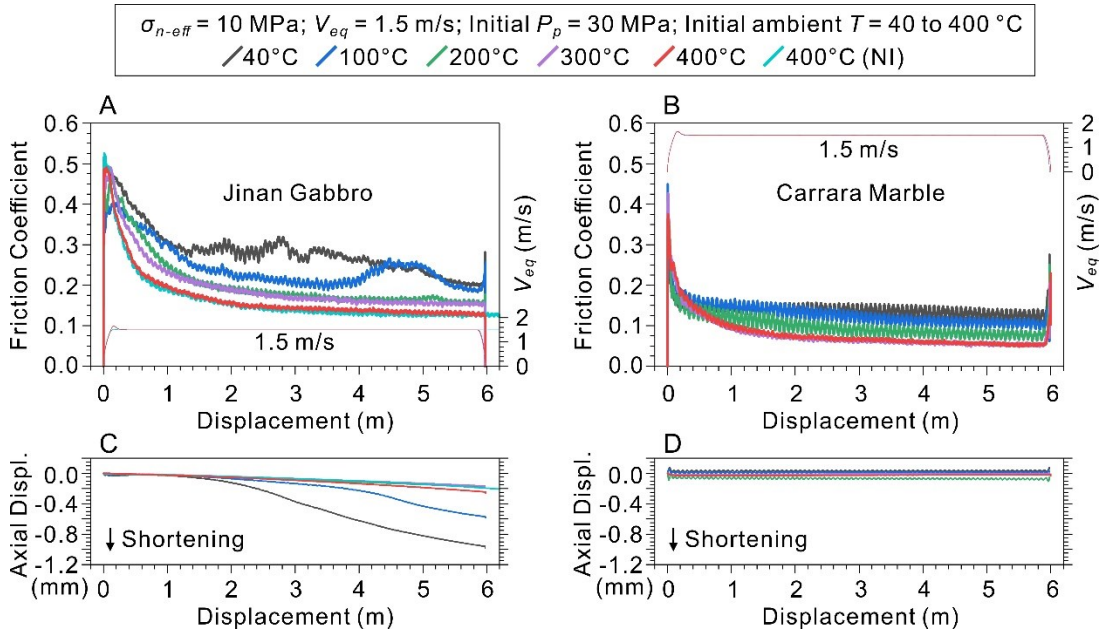

Figure B.2: Mechanical data obtained in high-velocity experiments performed on gabbro and marble at σ_{eff} of 10 MPa under hydrothermal conditions. **A-B**. Friction coefficient versus slip displacement. **C-D**. Axial displacement versus slip displacement. See text for description.

We fit the post-peak frictional data to the equation proposed by Mizoguchi et al. (2007) to get quantitative evaluations of μ_{ss}, D_c (slip weakening distance) and E_G (fracture energy). We also use an additional parameter D_{c0}, which is defined as the post-peak

displacement δ where $(\mu(\delta) - \mu_{ss}) = 1/e^*(\mu_p - \mu_{ss})$, to better depict the rapid weakening in the inception of slip. The D_c determined with Mizoguchi's equation and the D_{c0} thus represent the characteristic distance at which 95% and ~63% of the total weakening occurs, respectively. With T increasing from 40 to 400 °C, μ_{ss} decreases from 0.250 to 0.139, and from 0.133 to 0.063, for gabbro and marble, respectively (Figure B.3A). Regarding the changes of D_c and D_{c0} with T, gabbro differs from marble, i.e., an overall decreasing trend for gabbro versus an increasing trend for marble (Fig. Figure B.3B). Moreover, at any given temperature, D_c (1.347–2.387 m) and D_{c0} (0.398–0.884 m) of gabbro are evidently larger than those of marble (D_c of 0.124–0.851 m and D_{c0} of 0.038–0.244 m). In respect of E_G, the relation between E_G and T is indiscernible for gabbro, while marble shows a slight increase in E_G with T (Figure B.3C). As for the recovery of friction ($\Delta\mu_{recovery}$) defined as the peak friction coefficient during the deceleration minus μ_{ss}, gabbro has much lower $\Delta\mu_{recovery}$ than marble in general, and the $\Delta\mu_{recovery}$ of gabbro dwindles toward zero at $T \geq 200$ °C (Figure B.3D).

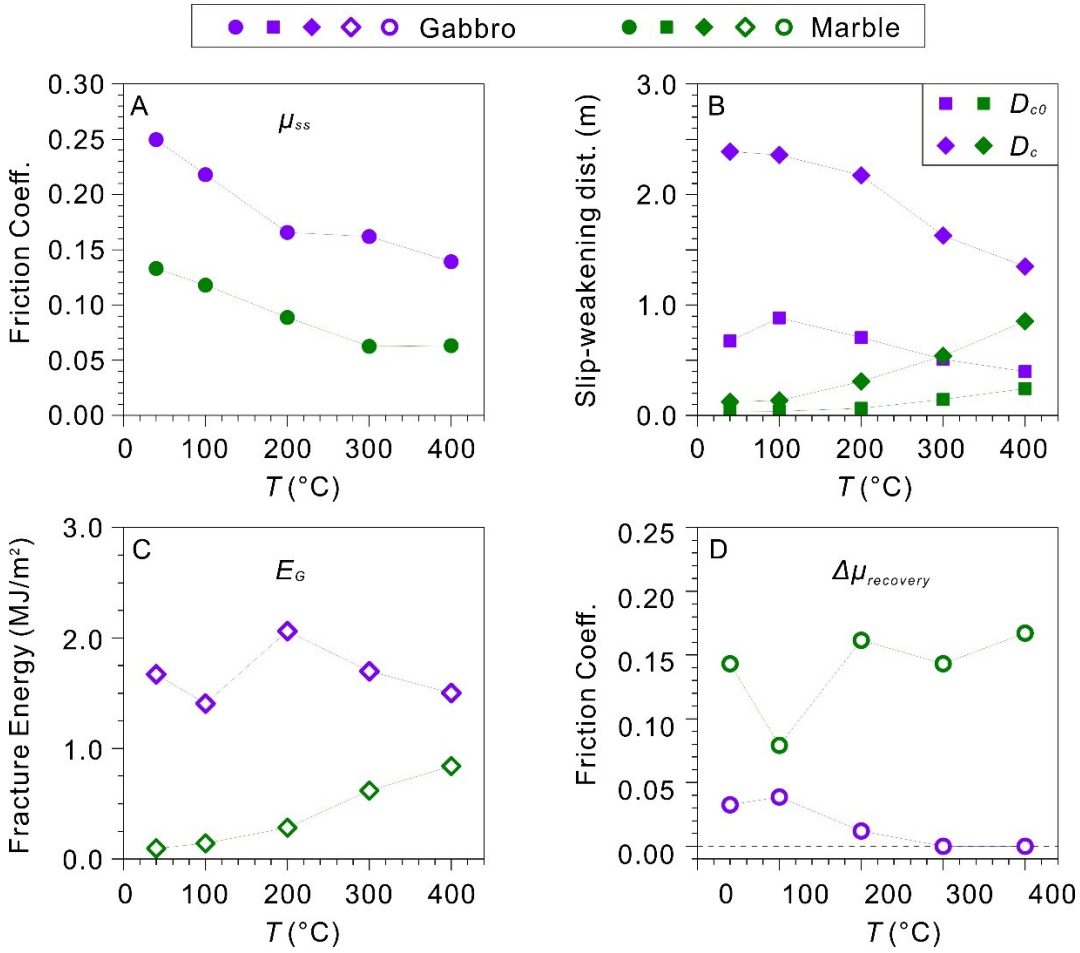

Figure B.3: Frictional parameters (**A.** μ_{ss}: steady state friction, **B.** D_c and D_{c0}: characteristic slip weakening distance, **C.** E_G: fracture energy, **D.** $\Delta\mu_{recovery}$: friction value recovered in deceleration stage) obtained in the experiments for gabbro and marble. See text for description.

Microstructures

We compare the deformation textures of the rock samples retrieved from the experiments performed under P_p = 30 MPa and two end-member ambient T of 40 and 400 °C, respectively. For gabbro, melts can be observed on the slip surfaces in both cases (Figures B.4A and C), though the sample halves were not welded after the experiments. The wide-distributed stripe-like melts and the vesicular textures on the slip surface (Figures B.4C and E) suggest more severe frictional melting in the test performed under T = 400 °C. Moreover, in some of the hollows of the slip surfaces, we

observe nanoflakes in the case of T = 40 °C (Figure B.4B), and rod- and flake-like structures on the micron scale in the case of T = 400 °C (Figure B.4D).

For marble deformed under T = 40 °C, some area of the slip surface is scattered with submicron individual grains, while some regions are featured by sintering of fine grains (Figures B.4F and G). In the case of T = 400 °C, recrystallization and grain growth (Figures B.4H and I) can be observed on the entire slip surface.

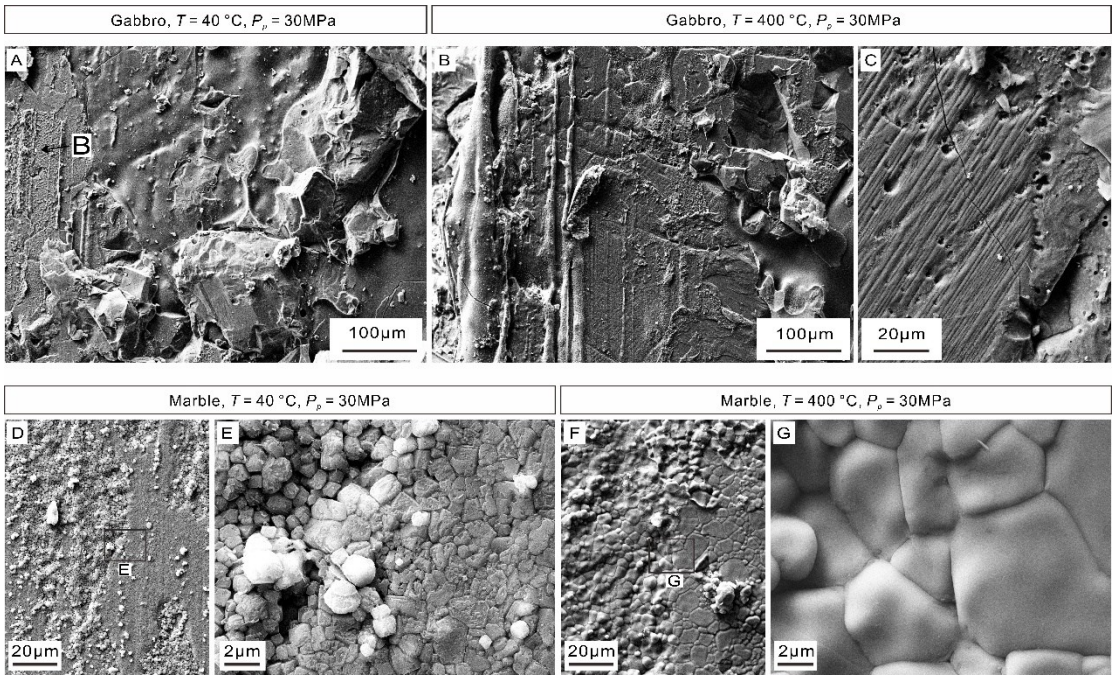

Figure B.4: Microstructures of the sheared gabbro (**A-C**) and marble (**D-G**) under at P_p =30 MPa, and T = 25℃ or 400℃. **A.** Experiment LHV2753, gabbro, T = 25℃. **B-C.** Experiment LHV2764, gabbro, T = 400℃. **D-E.** Experiment LHV2776, marble, T = 25℃. **F-G.** Experiment LHV2774, gabbro, T = 400℃. Experiments are performed at σ_{eff} of 10 MPa

Acknowledgements

I would like to give my special thanks to my supervisor, Giulio Di Toro, and co-supervisor, Lu Yao. Giulio, it has been a great honor for me to be one of your students. Thank you for your invaluable guidance, countless encouragement and continued support over the last 3.5 years. Your motivation, knowledge and enthusiasm have not only inspired me, but also helped shape me to become a better researcher. I will never forget this incredible experience. Lu has also been a brilliant supervisor and is always supportive in many ways. Your constant passion for laboratory work motivates me a lot. It has been an absolute pleasure to work with you. I hope this thesis is just the beginning of a fruitful collaboration between us.

I am very happy to be a part of the research group at Padua University. I wish to express my gratitude to all the group members with whom I have worked: Rodrigo, Giorgio, Telemaco, Simone, Luca, Francesco, Michele, Miriana and Wei-hsin. My grateful thanks will be extended to group members from INGV: Elena, Stefano and Chiara. Thank you for the constructive discussions and for contributing to the completion of my thesis.

I would like to thank all the fantastic colleagues and friends I met during my stay at the IGCEA. Especially, I wish to acknowledge Prof. Shengli Ma, Prof. Yongsheng Zhou, Jianye Chen and, of course, Lu Yao. Thanks for hosting me. The experience we have (group meetings and playing basketball weekly) is unforgettable.

I would like to thank my friends I met in Padova who enriched my life: Jeff, Chaoqun, Yu, Yikai, XiaoQin, Jiayi, Dalu, Shaomin, Rui, Lun, Wenqiang, Jun, Qiangwang, Yuting, Meng, Huan, Xiangli, Liying, Xiaoqin, Heng, etc... We shared our cook skills and specialty (hometown) dishes, which satisfied my Chinese stomach. I also thank Bowen, Qingyu, XiaoCui, Xiaoyang, Huiqi, Hong, Yu, Men, Dabao, Kaka, Huabiao, Yingshang, Jiankai, Yimo, Zhanjing, Zhiwei, Dong, Hang, Lufeng, Song, Yang, Minghui, etc…感

谢所有一直以来支持我的朋友们.

I am sincerely grateful to the reviewers of my thesis, Marie Violay (EPFL) and André Niemeijer (UU) for their constructive comments and invaluable feedback. Their contributions have significantly enhanced the quality of my thesis.

I acknowledge the China Scholarship Council for offering me a scholarship to pursue my Ph.D. in Italy. This research was also funded by the European Research Council and the National Natural Science Foundation of China. I am grateful for the grants that supported my conference attendance (EGU, GRC, SGI).

Finally, I would like to give my biggest appreciation to my parents and family for their unconditional love and support on my journey of growth. 感谢父母和家人在我成长道路上无条件的爱与支持.

Padova, 25/03/2023

Wei